Electrochemical Study of New Generation Photoactive Materials

A Thesis Submitted

To

Sikkim University

In Partial Fulfilment of the Requirement for the Award of Degree
of
MASTER OF PHILOSOPHY

Submitted by

Deshaj Bhujel

Roll No. 19MPCH01

Reg No: 19SU344637

Department of Chemistry, School of Physical Sciences

Sikkim University

6th Mile, Tadong, Gangtok, Sikkim-737102

April, 2021

Electrochemical Study of New Generation Photoactive Materials

A Thesis Submitted

To

Sikkim University

In Partial Fulfilment of the Requirements for the Award of Degree

of

MASTER OF PHILOSOPHY

Submitted by
Deshaj Bhujel
Roll No. 19MPCH01
Reg No: 19SU344637

Department of Chemistry, School of Physical Sciences
Sikkim University
6th Mile, Tadong, Gangtok, Sikkim-737102

Under the Supervision of
Dr. Anand Pariyar,
Department of Chemistry, School of Physical Sciences
Sikkim University
6th Mile, Tadong, Gangtok, Sikkim-737102
&
Co-Supervision of
Dr. SudarsanTamang,
Department of Chemistry, School of Physical Sciences
Sikkim University
6th Mile, Tadong, Gangtok, Sikkim-737102
April, 2021

Dated: 5th April 2021

DECLARATION

It is hereby declared that the thesis entitled **"Electrochemical Study of New Generation Photoactive Materials"** prepared solely by me for examination for the award of **Master of Philosophy (M.Phil.)** degree of Sikkim University is my own work. The work described in this thesis is based on experiments performed by myself under the supervision of **Dr. Anand Pariyar** (supervisor) and **Dr. Sudarsan Tamang** (co-supervisor), Assistant Professor, Dept. of Chemistry, Sikkim University. Any or no part of this thesis has not been submitted previously for any other degree, diploma, associateship, and fellowship.

Deshaj Bhujel

Roll No: 19MPCH01
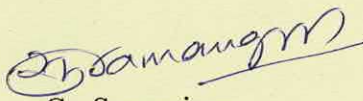
Reg No: 19SU344637

Department of Chemistry

School of Physical Science

Sikkim University

We recommend that this thesis be placed before the examiners for evaluation.

Supervisor

(Dr. Anand Pariyar)

(Seal)
Dr. ANAND PARIYAR
Assistant Professor
Department of Chemistry
Sikkim University Tadong-737102
Gangtok, East Sikkim

Co-Supervisor

(Dr. Sudarsan Tamang)

(Seal) Sudarsan Tamang
Assistant Professor
Department of Chemistry
SIKKIM UNIVERSITY
6 Mile Samdur PO Tadong
Ph 0359- 23206
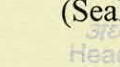
Head of the Department

(Prof. Sanjay Dahal)

(Seal)
अध्यक्ष/प्रभारी
Head/In-charge
रसायन विज्ञान
Department of Chemistry
सिक्किम विश्वविद्यालय
Sikkim University

Dated: 5th April 2021

CERTIFICATE

This is to certify that the thesis entitled **"Electrochemical Study of New Generation Photoactive Materials"** submitted to Sikkim University in partial fulfilment of the requirement for the degree of **Master of Philosophy in Chemistry** is a result of bonafied research work carried out by **Mr. Deshaj Bhujel** under my supervision in the **Dept. of Chemistry, Sikkim University**. Any or no part of this thesis has not been submitted previously for any other degree, diploma, associateship, and fellowship.

All the assistance and help received during the course of the investigation have been dully acknowledged by him.

Dr. Anand Pariyar (Supervisor)

Assistant Professor

Department of Chemistry

School of Physical Science

New Science Block

Sikkim University

Tadong, Gangtok

Sikkim, India – 737102

Dr. Sudarsan Tamang (Co-Supervisor)

Assistant Professor

Department of Chemistry

School of Physical Science

New Science Block

Sikkim University

Tadong, Gangtok

Sikkim, India – 737102

6 माइल, सामदुर, तादोंग – 737102
गंगटोक, सिक्किम, भारत
फोन–03592-251212, 251415, 251656
टेलीफैक्स - 251067
वेबसाइट - www.cus.ac.in

6th Mile, Samdur, Tadong-737102
Gangtok, Sikkim, India
Ph. 03592-251212, 251415, 251656
Telefax : 251067
Website : www.cus.ac.in

सिक्किम विश्वविद्यालय
SIKKIM UNIVERSITY

(भारत के संसद के अधिनियम द्वारा वर्ष 2007 में स्थापित और नैक (एनएएसी) द्वारा वर्ष 2015 में प्रत्यायित केंद्रीय विश्वविद्यालय)
(A central university established by an Act of Parliament of India in 2007 and accredited by NAAC in 2015)

Dated: 5th April 2021

PLAGIARISM CHECK CERTIFICATE

This is to certify that plagiarism check has been carried out successfully for the following **M.Phil.** thesis using **URKUND** Software and the results are within the permissible limit of the University.

Electrochemical Study of New Generation Photoactive Materials

Submitted by **Mr. Deshaj Bhujel** under the supervision of **Dr. Anand Pariyar** (Supervisor) and **Dr. Sudarsan Tamang** (Co-Supervisor) Assistant Professor, Dept. of Chemistry, School of Physical Sciences, Sikkim University.

Deshaj Bhujel
Signature of the Candidate

Supervisor
Dr. ANAND PARIYAR
Assistant Professor
Department of Chemistry
Sikkim University Tadong-737102
Gangtok, East Sikkim

Head of Department

अध्यक्ष/प्रभारी
Head/In-charge
रसायन विज्ञान विभाग
Department of Chemistry
सिक्किम विश्वविद्यालय
Sikkim University

Librarian

ACKNOWLEDGEMENT

Deshaj Bhujel
Roll No-19MPCH01
Reg No: 19SU344637

Research Scholar
Department. of Chemistry
School of Physical Sciences
Sikkim University
Tadong, Gangtok
Sikkim, India-737102

Table of Contents

Contents

List of Tables

i

List of Figures

List of Abbreviations/Symbols

CB	Conduction Band
CBM	Conduction Band Minimum
CV	Cyclic Voltammetry
CAE	Constant Analyser Energy
CdS	Cadmium Sulfide
CdSe	Cadmium Selenide
CdTe	Cadmium Telluride
DSSCs	Dye Sensitized Solar Cells
DMF	Dimethyl Formamide
DMSO	Dimethyl Sulfoxide
DAm	Dodecylamine
DCM	Dichloromethane
DHP	Dihydropyridine
DCE	Dichloroethane
DFT	Density Functional Theory
DEC	Diethyl Carbonate
EA	Electron Affinity
EDX	Energy Dispersive X-ray
FWHM	Full Width Half Maximum
FTO	Fluorine Doped Tin Oxide
FT-IR	Fourier Transform Infrared Spectroscopy
GO	Graphene Oxide
HOMO	Highest Occupied Molecular Orbital
HI	Hot Injection
HDA	Hexadecylamine
HFE	Hydrofluoroethers
HRTEM	High Resolution Transmission Electron Microscopy
HAT	Hydrogen Atom Transfer
IP	Ionisation Potential
ITO	Indium Tin Oxide
LUMO	Lowest Unoccupied Molecular orbital

LARP	Ligand Assisted Reprecipitation Method
LHPs	Lead Halide Perovskites
LED	Light emitting Diodes
LiTFSL	Trifluoromethane Sulfonomide Lithium
MA	Methylammonium
MA	Myristic Acid
NREL	National Renewable Energy Laboratory
NHE	Normal Hydrogen Electrode
NMR	Nuclear Magnetic Resonance Spectroscopy
NCs	Nanocrystals
OAm	Oleylamine
OA	Oleic acid
PCE	Power Conversion Efficiency
PESA	Photoemission Spectroscopy in Air
PXRD	Powder X-ray Diffractometer
PL	Photoluminescence
PCBE	[6,6]-Phenyl C61-Butyric Acid 3-Ethylthiophene
Py	Pyridine
QDs	Quantum Dots
rpm	Rotation Per Minute
rt	Room Temperature
SEPM	Semi-Empirical Pseudo-Potential Method
SEM	Scanning Electron Microscope
SA	Stearic Acid
SAm	Stearylamine
TOP	Trioctylphosphine
TOPO	Trioctylphosphine Oxide
TBAP	Tetrabutyl Ammonium Perchlorate
THAP	Tetrahexyl Ammonium Perchlorate
TBAHFP	Tetrabutyl Ammonium Hexafluoro Phosphate
TLC	Thin Layer Chromatography
THF	Tetrahydrofuran
TGA	Thermogravimetric Analysis
UV	Ultra Violet

UPS	Ultraviolet Photoelectron Spectroscopy
VBM	Valence Band Maximum
VB	Valence Band
XPS	X-ray Photoelectron Spectroscopy
E_g	Band Gap
°C	Degree Celsius
h	Planck's Constant
q	Charge of an Electron
ε	Permittivity of The Dielectric Constant of Semiconductor
μ	Reduced Mass
K_{sv}	Stern-Volmer Quenching Constant
MHz	Megahertz
eV	Electron Volt
V	Volt
mV	Millivolt
h	Hour
S	Second
λ	Wavelength
nm	Nanometre
mL	Millilitre

CHAPTER-I

INTRODUCTION AND LITERATURE SURVEY

<div align="center">

CHAPTER-I

INTRODUCTION AND LITERATURE SURVEY

</div>

1.1. Introduction

The escalating consumption of non-renewable energy resources *viz.* fossil fuels, coal, and natural gas has led to the gradual depletion of such resources and is on the verge of exhaustion. At the same time, these hydrocarbon-based energy resources contribute a major role in environmental pollution and defy the principles of sustainable development.[1] However, to meet the ever-growing energy demand, alternative clean, safe, and renewable sources of energy such as solar energy, wind energy, tidal energy, biomass, and geothermal energy are highly desirable[2,3] and have become increasingly more significant. In particular, solar energy is undoubtedly one of the most abundant clean sources of energy with environmentally benign features.[4] In nature, solar energy gets converted into chemical energy for sustaining various life processes *via* photosynthesis wherein the existence of light-harvesting material also termed as "photoactive material" plays a decisive role. These materials have an intrinsic capacity to absorb light in the visible region and transform it into a suitable form for regulating various life-sustaining processes.[3] This transformation of energy is a key inspiration for the renaissance and the development of photovoltaics which has brought a paradigm shift in this area. In the view of the overall advancement of the photovoltaics, the designing and development of highly efficient photoactive materials are highly appealing.

1.2. Overview of photoactive material in the solar cell

The decades of studies in photovoltaics resulted in the development of the solar cells of different generations comprising of different photoactive materials. In the year 1954, the seminal work by Chapin and his group[5] introduced the exploitation of solar energy for the construction of the first generation solar cells by employing crystalline silicon-based photoactive materials demonstrating the power conversion efficiency (PCE) of 4.5%. Inspired by this work, the second-generation solar cell was evolved constituting thin film-based inorganic materials such as cadmium telluride and copper indium(gallium) diselenide.[6] The transition of photovoltaics from first to the second generation witnessed the improvement in the higher absorption of photons, spectral sensitivity, and photoactivity of the photoactive material. Despite the success in the

advancement of solar cells to some extent, the aforementioned strategies were not yet efficient due to various drawbacks. These include (a) low efficiency of the first and second generations photoactive materials under visible light (b) the high consumption of energy by UV sources, (c) instability during constant use (d) expensive nature of silicon, intrinsic toxicity of cadmium metal, scarcity of indium and low earth abundance of tellurium and (e) harsh preparation conditions.[1,7,8]

Intending to address these issues, the inception of the new generation photoactive material came in the forefront, also commonly known as third-generation photoactive materials or new emerging technology.[9,10] They are primarily based upon organic solar cells,[11–14] dye-sensitized solar cells (DSSCs),[7,15–17] quantum dots (QDs),[18–20] conjugated polymer[9,21] and perovskites.[22–29] Over the last decade, these new emerging technologies focused mostly on improving efficiency, stability, and reproducibility. Among various classes of third-generation photoactive materials, the colloidal organic-inorganic or fully inorganic semiconductor nanocrystals (NCs) have exhibited promising photophysical properties such as superior carrier mobilities, high optical absorption coefficient, improved thermal stability, high luminescence efficiency and lower exciton binding energy suitable for the study of photovoltaics.[30]

1.3. Colloidal semiconductor nanocrystal (NCs) or quantum dots (QDs)

Colloidal semiconductor NCs also known as QDs are tiny crystalline materials with typical physical dimensions in the range of 1-10 nm exhibiting properties in between the bulk and the molecular semiconductor.[31] They have gained much recognition in the past few years owing to their versatile tunable properties such as size,[32,33] size-distribution,[34] structure,[35] and compositional-dependent optoelectronic properties[36–38] as well as their desirable applications in the field of solar cells,[39,40] photo-catalysis,[41] molecular and cellular imaging and light-emitting diodes.[26,27,31,41–44] The most important feature of semiconductor QDs is the distinctive nature of their band structure (direct or indirect) and a bandgap energy (E_g) which lies in between $0 < E_g < 3$ eV and it is this minimum energy which is required to excite an electron from the valence band (VB) to the conduction band (CB). Therefore, it is inevitable to know the nature of band structure of semiconductor NCs, such as the energy values of valence band maximum (VBM, also known as highest occupied molecular orbital or HOMO), the conduction band minimum (CBM, also called lowest unoccupied molecular orbital or LUMO) and the band gap to come across the relationship between their structure and physical

properties.[42] In semiconductor NCs, an electron gets excited from HOMO to LUMO by absorption of a photon of energy equal to or greater than E_g leaving behind a positively charged called hole in the VBM. While applying the electric field the negatively charged electron and the positively charged hole may get mobilized resulting in a production of current but at their lowest state the electron and the hole get bound due to electrostatic Coulomb force known as exciton. Furthermore, the relaxation of the excited electron towards the VB leads to emission of photon, known as radiative recombination. Depending on the material, exciton has finite size within the crystal varying from 1-10 nm.[31,44] If the size of the nanocrystal is smaller than the Bohr's exciton radius which is given by following equation:

$$\alpha_B = \frac{4\Pi\varepsilon\mathcal{C}\hbar^2}{\mu q^2}$$

[Where ε = absolute permittivity of the vacuum, $\mathcal{C}$ = permittivity of the dielectric constant of semiconductor, $\hbar = \frac{h}{2\pi}$, h = Planck's constant, μ = reduced mass, q = charge of an electron] shows a strong quantum confinement effect which is a major feature of semiconductor NCs.[31] Within this quantum confinement regime, nanocrystal will display quantized energy level which is distinct from the continuous band of the bulk counterparts mimicking a characteristic of discrete molecular semiconductor, as shown in figure 1.1.
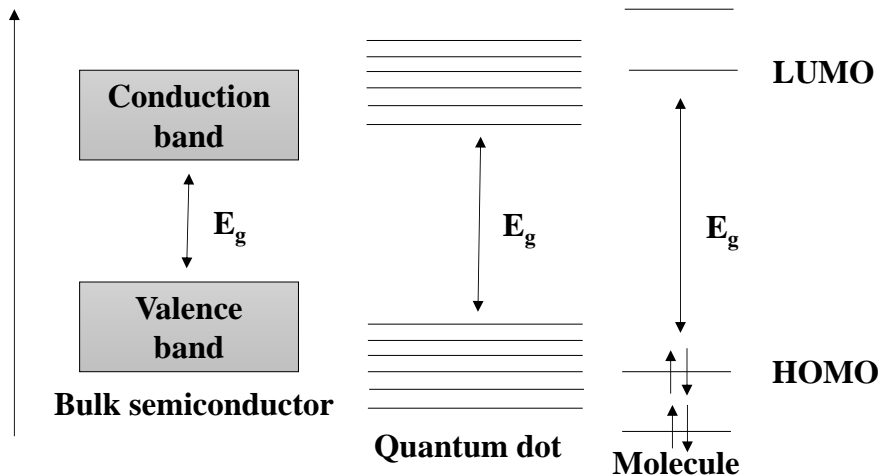
Figure 1.1: Systematic representation of the energy levels in a bulk semiconductor, a quantum dot, and a molecule.

The size-dependent optical and electronic properties of the QDs are directly associated with the quantum confinement effects.[45,46] These intriguing size-dependent optoelectronic properties of materials within the quantum confinement regime have a tremendous prospect for various optoelectronic applications. One of the interesting

properties of these QDs is their tunable band-edge alignments which can be tailored to a large extent simply by varying the physical size of the QDs without introducing any changes in the chemical composition. The phenomenon of the quantum size effect motivates the researchers to exploit the possibilities of tuning the optical and electrical properties of QDs simply by monitoring the size and growth processes of QDs. As a result, researchers can tune the luminescence of semiconductor QDs throughout the ultraviolet, visible, near-infrared, and mid-spectral range.

1.4. General methods for the synthesis of colloidal semiconductor NCs

As far as the preparation of colloidal semiconductor QDs is concerned, it involves the traditional colloidal-based hot injection (HI) method,[47,48] room temperature ligand assisted reprecipitation (LARP) method[49] and heating-up methods.[50–52] Typically, the precise control of the colloidal synthesis of QDs in terms of shape and size can be accomplished by adjusting the nucleation and growth processes of QDs. These processes in turn can be controlled by manipulating the reaction temperature,[53] nature of capping ligands[34], and composition of precursors[54], etc. For example, figure 1.2 showcases the size-controlled synthesis of the library of semiconductor NCs such as II-VI (CdS, CdSe),[32,35,55–62] III-V (InP, InAs),[63–66] IV-VI (PbS, PbSe, PbTe),[33,67–71] and perovskites [24,25,46] based NCs as a function of temperature, composition, and presence of capping ligands. Interestingly, the precise control was achieved at high temperature in the presence of suitable stabilizing ligands such as oleic acid, alkylamine (e.g., oleylamine, OAm; hexadecylamine, HDA), alkylphosphines (e.g., trioctyl phosphine, TOP), alkylphosphine oxide (e.g., trioctylphosphine oxide, TOPO), and as depicted in figure 1.2.

$$Cd(CH_3)_2 + C_8H_{17})PSe \xrightarrow{\text{300 °C, HDA-TOPO-TOP}} CdSe \text{ nanocrystals} \quad \text{................(I)}$$

$$InCl_3 + [(CH_3)_3Si]_3P \xrightarrow{\text{260 °C, TOP}} InP \text{ nanocrystals} \quad \text{................(II)}$$

$$Pb(CH_3COO)_2 + (C_8H_{17})_3PSe \xrightarrow{\text{180 °C, OAc}} PbS \text{ nanocrystal} \quad \text{................(III)}$$

$$\underset{\text{lead acetate}}{Pb(CH_3COO)_2} + X_2 + \underset{\text{cesium oleate}}{Cs(oleate)} \xrightarrow[\text{1-ODE}]{\text{200 °C, OAc , OAm}} \underset{\substack{\text{cesium lead} \\ \text{halide nanocrystal}}}{CsPbX_3} \quad \text{................(IV)}$$
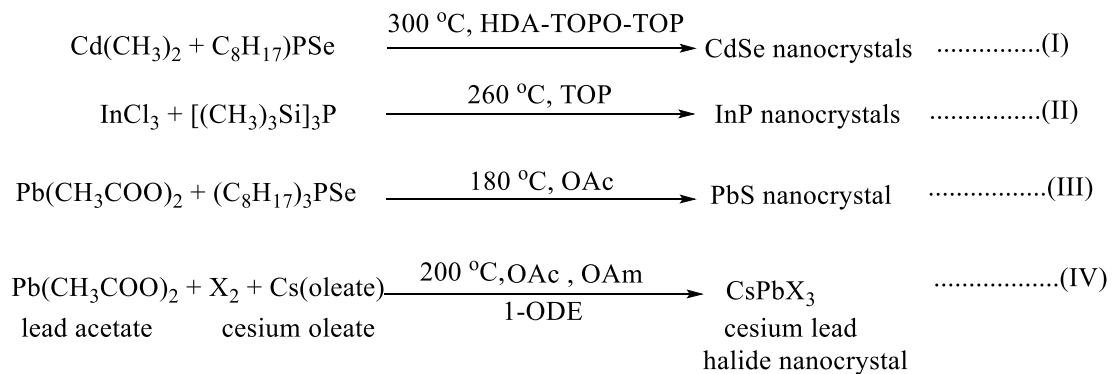
Figure 1.2: Syntheses of various size-controlled semiconductor QDs.

1.5. Perovskites NCs as a versatile new generation photoactive material

Among various semiconductor QDs, the metal halide-based perovskites semiconductor QDs (organic-inorganic or fully inorganic) has outperformed a broad range of photoactive materials for future energy fulfilment with facile low-cost synthesis and higher power conversion efficiency.[8,30,72] The word "perovskite" is generally termed for the materials bearing resemblance to the crystal structure of calcium titanate ($CaTiO_3$) which is expressed by A_nBX_{n+2}, where A represents an organic or inorganic cation, B is a metal cation and X represents a halide anion *viz.* Cl^-, Br^-, and I^- [73] as shown in figure 1.3. It was discovered by German mineralogist Gustav Rose in 1839 in the Ural mountain and named after the Russian Count, Lev A. Perovski.
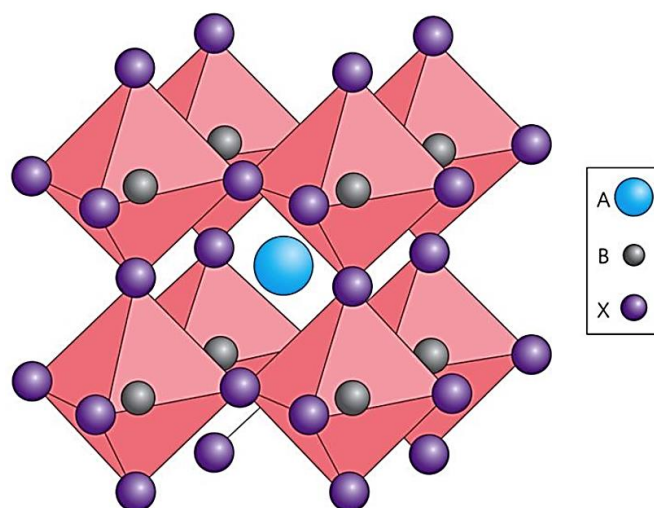
Figure 1.3: Crystal structure of perovskite A_nBX_{n+2}.[28]

It is further classified into two categories depending upon the type of the cation A. If the cation A is organic (e.g., methylammonium, MA or formamidinium, FA) and B an inorganic (e.g., divalent lead, tin, or germanium), the perovskite is referred to as hybrid organic-inorganic perovskites. In contrast, if the cation A is inorganic (e.g., monovalent cesium or rubidium), the structure is termed as fully inorganic perovskites. Moreover, the value of n in the general formula A_nBX_{n+2} describes the perovskite's structural dimensionality of NCs. When n=1, (e.g., $CsPbX_3$) the perovskite characterizes in the three-dimensional (3D) form. Similarly, when n=4, (e.g., Cs_4PbX_6) the perovskites structure becomes zero-dimensional (0D) in nature. Till date, the majority of research has focused on the 3D NCs of the type ABX_3 (e.g. $CsPbX_3$), since this class of NCs exhibit trap-free nature of surface defect.[74–78] Using this material, in the year 2009,

Kojima *et al.*[79] demonstrating PCE of solar cell ~3.8% and has dramatically increased to the current value of >25% in 2019 [38,80–85] as certified by the National Renewable Energy Laboratory (NREL) and further making advancements towards the theoretical limit. This ever-increasing PCE of perovskites QDs in photovoltaics is attributed to their easy solution processing, suitable bandgap energy, excellent photoelectric properties, lower exciton binding energy, high optical absorption coefficient, high dielectric constant, long diffusion length and slow radiative recombination of photoexcited charge carrier.[28,83,86–88] Furthermore, they have also been widely employed in other optoelectronic applications such as light-emitting diodes (LEDs),[27,54,55,89] low-threshold lasers [90,91] and photo-detectors.[24,92]

1.6. Motivation

As discussed above, the perovskites semiconductor QDs are a promising candidate for photovoltaic and other optoelectronic applications due to their low processing cost, tunable optical and electronic bandgap from near-infrared to the near ultraviolet range. These fascinating optoelectronic properties of semiconductor QDs have opened up a new avenue for their electrochemical studies. Since these studies would allow us to understand the effect of size,[25,26,93] shape, and composition[34,46,94] on band structures *viz.* VBM, CBM, quasi-particle gap.[43,94–99] To design and develop semiconductor QDs-based devices, the knowledge of band-gap engineering of their electronic structure is highly indispensable. Several instrumental methods such as photoemission spectroscopy in the air (PESA),[93,100] scanning tunneling spectroscopy (STS),[101,102] ultraviolet and X-ray photoelectron spectroscopy (UPS and XPS),[103] and cyclic voltammetry (CV),[43,60,104–106] offer an opportunity to evaluate the band structure (band-gap energy as well as the band edge (VBM and CBM) positions and the trap states) of the semiconductor NCs. Among those methods, CV has emerged an ideal tool to carry out such investigation as it is easy to access and can perform electrochemical studies directly from electroactive solution. Further, it also contributes to a better understanding of chemical reaction occurring at the interface of semiconductor NCs. By performing CV experiments in the year 2016, Nag *et. al.*[25] was able to correlate the systematic variation in band edge alignment of CsPbX$_3$ NCs through anion exchange reaction (effect of halide anions). However, as of now, the clear understanding of the effect of size over the band edge alignment and optical transition across these edges without

changing the composition of perovskites QDs have not been emphasized and the study of electrochemical investigation in this direction is highly noteworthy.

Thus, the main aim of this thesis is to understand the effect of size and capping ligands over a band edge position. Herein, we have prepared $CsPbBr_3$ QDs of varying sizes at different temperatures following the three-precursor method [36,107] with some modified experimental condition using $Cs:Pb:Br_2$ in the ratio of 1:1:6. The formed $CsPbBr_3$ QDs were characterized with the help of UV-visible spectroscopy, photoluminescence spectroscopy, Fourier infrared spectroscopy (FTIR), powder X-ray diffractometer (PXRD), X-ray photoelectron spectroscopy (XPS), and transmission electron spectroscopy. The main focus of our project relies on the electrochemical investigation of size-dependent $CsPbBr_3$ QDs and their effect on band edges without changing the halide composition at the various reaction temperature. Compared to other conventional visible-light-emitting semiconductors QDs, $CsPbBr_3$ QDs withstand with a unique promising photophysical property as mentioned above due to its high defect tolerant properties. Such exceptional properties of perovskite NCs are strongly dependent on the nature of band edges *i.e*., VBM and CBM. The correlation between the nature of VBM and CBM and optical transition across these edges can be extensively studied by performing CV experiments.

1.7. Aims and Objectives

The aims and objectives of the research are as follows:

- Preparations of colloidal semiconductor nanocrystals and its characterization using conventional spectroscopic and analytical tool.
- Electrochemical investigation of nanocrystals and estimation of energy level using cyclic voltammetry.
- Understanding the influence of particle size, and capping ligands on the energy level of HOMO and LUMO of the nanocrystals.
- Use of the acquired knowledge of band edge for direct application.

1.8. Literature Review

The electrochemical properties of semiconductor QDs are directly dependent on their band structures. A plethora of reports utilizing various electrochemical methods is well-documented for understanding the band structures of semiconductor QDs. However, in

this thesis, our focus is mostly on the electrochemical methods based on the CV for evaluating the electrochemical properties of colloidal semiconductor QDs. Some of the interesting and relevant work reported in the literature are presented here in detail.

In **2001**, Haram *et. al.* demonstrated the direct relationship between the electrochemical bandgap and the electronic spectra of tri-*n*-octylphosphine oxide (TOPO) capped cadmium sulfide (CdS) QDs.[60] They performed the electrochemical investigation in the presence of *N, N′*-dimethylformamide (DMF) solvent and tetrahexylammonium perchlorate (THAP) as the supporting electrolyte for the first time using CV under inert conditions. The NCs exhibited the bandgap of 2.96 eV with an oxidation (anodic) and reduction (cathodic) peaks at 0.80 V and -2.15 V respectively. They further concluded that the redox reaction was irreversible. The electrochemical behaviour of different sizes of CdS QDs was investigated and they observed the shifting of the band edge position with respect to particle dimension which was in accordance with the optical results (e.g., optical band-gap). Further, they concluded that the CdS QDs act as a multi-electron donor and acceptor at a given potential.

In **2003**, Sasaki *et. al.* revealed the band structure of self-assembled multilayer thin film of titania nanosheet on a conductive indium tin oxide (ITO) substrate using the electrochemical and photoelectrochemical technique.[94] They performed the electrochemical CV studies of titania nanosheet and anatase electrode in the non-aqueous electrolyte and exposed that the titania nanosheet underwent insertion/extraction of Li^+ ion due to the reduction/oxidation of Ti^{+4}/Ti^{+3}. The titania nanosheets were subjected to UV light irradiation ($\lambda < 320$ nm) under the presence of the positive potential (at around -1.27 V and above) to generate the photocurrent. From, the detailed electrochemical investigation, the estimated band-edge energy, and the flat-band potential values were noted at 3.84 eV and -1.27 ± 0.05 V respectively.

In **2003**, Nan *et. al.* reported the ionization potential (I.P), electron affinities (E.A), and the bandgap in CdSe NCs with the help of CV.[108] They performed the electrochemical measurements by modifying the gold disk microelectrode of radius 400 μm with a thin film of monodispersed CdSe NCs having a diameter of ~3.73 nm at a scan rate of 20 mVs^{-1} under nitrogen atmosphere. They used dry acetonitrile as a solvent and 0.1 M

tetrabutylammonium hexafluorophosphate (TBAPF$_6$) as a supporting electrolyte for the preparation of electrolyte solution. They noticed a prominent oxidation peak *i.e.*, I.P at around +1.4 V and reduction peak *i.e.,* E.A at around -0.75 V. For estimating the values of I.P and E.A, they used the following equation as shown below;

$$I.P = - (E_{ox} + 4.14) \text{ eV}$$
$$E.A = - (E_{red} + 4.14) \text{ eV}$$

Where, E$_{ox}$ = onset oxidation potential; E$_{red}$ = onset reduction potential. Furthermore, they also prepared the CdSe NCs of varying sizes such as 3.23, 3.48, 3.73, and 3.80 nm for investigating the effect of quantum confinement in their band edge energy level. With the increase in the size of the NCs, a decrease in the bandgap energy value and vice versa was noted.

In **2005**, Pron *et. al.* investigated the comparative studies of electrochemical properties of electrochemically inactive surface ligand such as TOPO-capped CdSe QDs with its analogous QDs containing electrochemically active oligoaniline ligands.[61] They focused on TOPO-capped QDs of different sizes in the broad range of 3 to 6.5 nm intending to amplify the effect of quantum confinement effect on electrochemical properties (the relative position of the HOMO and LUMO levels). The examined electrochemical data were in good agreement with absorption/emission spectroscopy and theoretically studies. Further, for electrochemically active ligand exchange *i.e.*, aniline tetramer, they noticed its profound influence on the band structure *viz.* HOMO and LUMO which shifted towards higher and lower potentials respectively. This study showed an interesting possibility of switching the electrochemically active ligand between its conducting and non-conducting states and opened the opportunity to address the electrical properties of individual semiconductors which were otherwise not possible for TOPO-capped ligands.

In **2005**, Gaponik *et. al*. synthesized thiol-caped CdTe NCs of various sizes and demonstrated the correlation between the effect of size-dependent electrochemical properties, optical properties, and their stability.[32] They conducted the electrochemical investigation in an aqueous buffer solution containing 0.1 M Na$_2$SO$_4$ and 0.02 M Na$_2$B$_4$O$_7$ (pH ~9.2) employing cyclic voltammetry. While investigating, they noticed a distinct oxidation and reduction peaks in the voltammogram and the peak positions varied as a function of the size of the NCs. The size-dependent oxidation and reduction

of NCs resulted in the increase or decrease of the bandgap position owing to the quantum confinement effect. The peak moved more towards negative potential due to the decrease in the size of NCs. During the process of the NCs oxidation, the total charge pass associated with a related peak was consistent with the photoluminescence efficiency of CdTe NCs. These experimental observations led them to conclude that the resulting peak was due to the oxidation of the Te-related surface trap. In contrast, with the increase in the size of the NCs, the Te-related surface trap moved towards the lower energies.

In **2005**, Nan *et. al.* disclosed the defect states of semiconductor NCs by employing CV. To understand the role of defect states in semiconductor NCs they prepared CdSe NCs in the presence of TOPO.[109] They performed the electrochemical study of CdSe/TOPO NCs in an inert atmospheric condition consisting of acetonitrile and 0.1 M TBAPF$_6$ in the presence of ionic liquid, 1-dodecyl-3-methylimidazolium-bis-(trifluoromethylsulfonamide) [C$_{12}$ mim] [Tf$_2$N] with a scan rate of 20 mVs^{-1}. The recorded voltammogram exhibited an additional oxidation and reduction peaks in between valence band and conduction band which was attributed to the existence of the defect states situated in between the bandgap of NCs.

In **2008**, Haram *et. al.* used cyclic voltammetry to come across the electrochemical determination of band structure parameters such as the conduction band edge, the valance band edge, and the quasi-particle gap of diffusing CdSe QDs.[43] These parameters changed as the function of particle size. Due to the poor dispersion capability of QDs in many polar solvents, the electrochemical studies were performed by modifying electrode with a thin film of QDs. Thomas Nann and co-workers[110] carried out CV measurements of modified thin-film electrodes and compared the results with values obtained from spectroscopic measurements (UV-visible absorption and PL spectra). However, during CV measurements of this modified electrode, only the anodic peak was estimated due to the degradation of QDs. To overcome the shortcoming of the modified thin-film electrode, Haram and his co-worker carried out voltammetric measurements in the dispersed medium. They chose TOPO-capped CdSe QD for this purpose. CV measurements were carried out in the size range of 1.9 nm to 3.6 nm and the results were correlated with theoretical calculations based on semi-empirical pseudo-potential method (SEPM) and displayed strong correlation especially in the

strong quantum confinement regime of QDs *i.e.*, below 3 nm. Figure 1.4.(a) showed the measured CV curves in the presence and absence of dispersed QDs in the DMSO-toluene solution containing 100 mM of TBAP as a supporting electrolyte with a scan rate of 100 mVs^{-1}. The potential difference between irreversible cathodic (C$_1$) and anodic peaks (A$_1$) as indicated at -1.56 V and 0.80 V *vs* NHE respectively were in accordance with bandgap energy obtained from optical bandgap. Furthermore, the separations between the irreversible cathodic and anodic peaks of different size of QDs leads to a quasi-particle gap (ε_{gap}^{qp}) which were also found to be in good agreement with the optical band gap as shown in figure 1.4. (b).
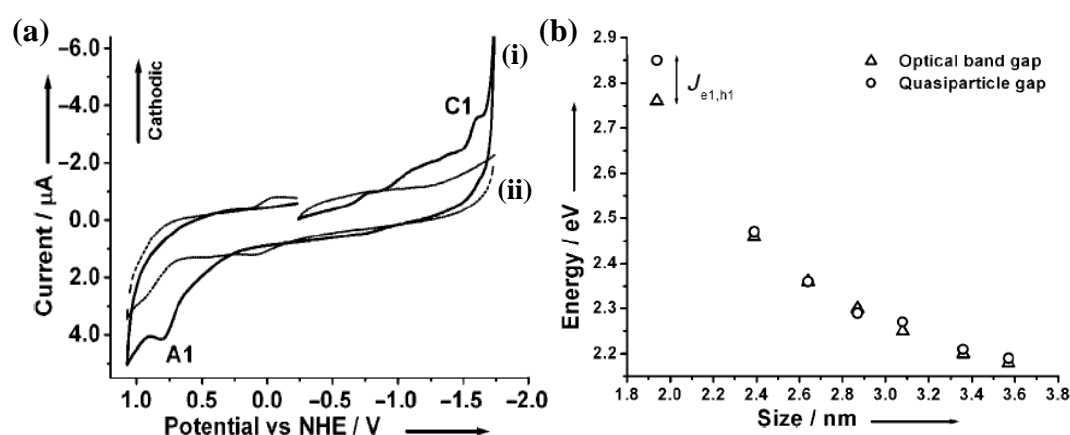
Figure 1.4: (a) Representation of cyclic voltammogram in the presence (i) and absence (ii) of TOPO-capped CdSe QDs dispersed in DMSO-toluene solution, and (b) the comparative study of the effect of size over electrochemical and optical band gap.[43]

In **2010**, Yahaya *et. al*. described a technique to estimate the HOMO and LUMO of an *n*-type polymer of [6,6]-phenyl C61-butyric acid 3-ethylthiophene ester (PCBE) and a *p*-type polymer of poly (3-octyl-thiophene-2,5-diyl) (P$_3$OT).[111] Based on CV studies, they reported the electrochemical bandgap of these materials to be around 1.83 eV (for P$_3$OT, HOMO = 5.59 eV and LUMO = 3.76 eV) and 1.93 eV (for PCBE, HOMO = 5.87 eV and LUMO = 3.91 eV). These electrochemical data were found to be in correlation with the optical band-gap values obtained from the optical absorption spectroscopy. For the estimation of the energy level of HOMO and LUMO they operated an empirical relation as shown below;

$$E_{LUMO} = [E_{red} - E_{1/2(ferrocene)} + 4.8] \text{ eV.}$$

$$E_{HOMO} = [E_{ox} - E_{1/2(ferrocene)} + 4.8] \text{ eV.}$$

Having studied the electrochemical band structure of these materials, they further exhibited their application in the construction of the solar cells comprising of P$_3$OT and PCBE with an open-circuit voltage up to 750 mV.

Again, in the year **2011**, Haram *et. al.* reported the effect of size quantization on the band edge position of CdTe stabilized by oleic acid with the help of cyclic voltammetry.[112] They carried out the electrochemical investigation under inert atmospheric condition by purging high purity argon gas in a DCM solution containing tetra butyl ammonium perchlorate (TBAP) as a supporting electrolyte. All the experiments were reported with a scan rate of 100 mVs^{-1}. They clearly demonstrated the effect of size over the VBM (HOMO) and CBM (LUMO) and their corresponding influence towards the UV-visible absorption and emission spectra as depicted in figure 1.5. They further correlated their simulated results with density functional theory (DFT) as a function of size and the DFT results exhibited a good agreement with the values obtained from UV-visible Spectroscopy
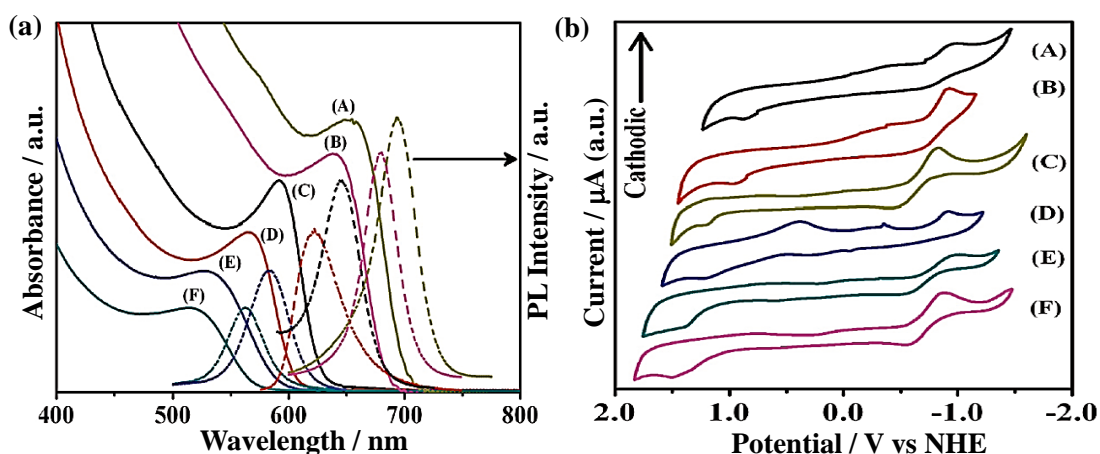
Figure 1.5: Effect of size of CdTe QDs towards the (a) UV-visible absorption and emission spectra and (b) their corresponding effect on the VBM and CBM as shown by cyclic voltammogram curve.[112]

In **2013**, Branzoi *et. al.* demonstrated the estimation of the energy level of HOMO and LUMO and the bandgap between organic materials through cyclic voltammetry.[99] They selected biodegradable organic semiconductors *viz.* indigo, cibalackrot, vat yellow 1, and vat orange 3 for developing biodegradable photovoltaic devices. The energy levels of HOMO and LUMO were estimated by employing ferrocene as an internal standard reference. The values of the energy levels were estimated by using empirical equation reported by Bredas *et. al*.[113] as shown under;

$$E \text{ (HOMO)} = -e \, [E_{ox}^{onset} + 4.4]$$

$$E \text{ (LUMO)} = -e \, [E_{red}^{onset} + 4.4]$$

Furthermore, the values of the optical band gap energy (E_g) were estimated using the following relation, where, the λ_{onset} represents the longest absorption wavelength.

$$E_g = 1242 \, / \, \lambda_{onset}$$

They showed that the estimated energy level values obtained from electrochemical studies were in good agreement with the bandgap estimated from optical absorption spectroscopy. Besides, they also revealed that the indigo and cibalackrot displayed an ability to carry both types of charges (positive and negative).

In **2013**, Haram *et.al.* employed CV to understand the effect of graphene oxide (GO) on the band edge position of NCs of CdTe. For this purpose, they carried out the reduction of GO to give the reduced graphene oxide (r-GO)[114] and prepared the composite of CdTe with r-GO (r-GO-CdTe). The electrochemical measurement of CdTe NCs and r-GO-CdTe composite were performed in a solution consisting of 0.1M Na_2SO_4 and 0.02 M $Na_2B_4O_7$ (borate buffer of pH 9.53) on gold disk electrode. They observed that the r-GO-CdTe composite displayed quasi-particle bandgap energy of 2.10 eV which was higher in comparison to CdTe NCs (1.93 eV) in the absence of r-GO. Thus, they concluded that the tunability in the band edge position can be achieved simply by introducing r-GO in the matrix of CdTe NCs.

In **2014**, Liu *et. al.* prepared CdSe NCs to understand the electronic band structure and their electrochemical properties.[34] They explored the influence of the concentration of the CdSe NCs on both solution-based and thin film-based electrochemical studies in the presence of electrolyte solution consisting of 10 mL of acetonitrile and 0.1 M $TBAPF_6$ at different scan rates of 10-30 mVs^{-1}. On contrary to a weak electrochemical signal in a solution-based system, a strong signal was noted in the case of a thin film-based counterpart as shown in figure 1.6. (a). Next, they put their efforts in tracing the impact of water in the electrolyte solution consisting of NCs which revealed that the presence of water resulted in the generation of undesired peaks due to the degradation of NCs as shown in figure 1.6.(b).
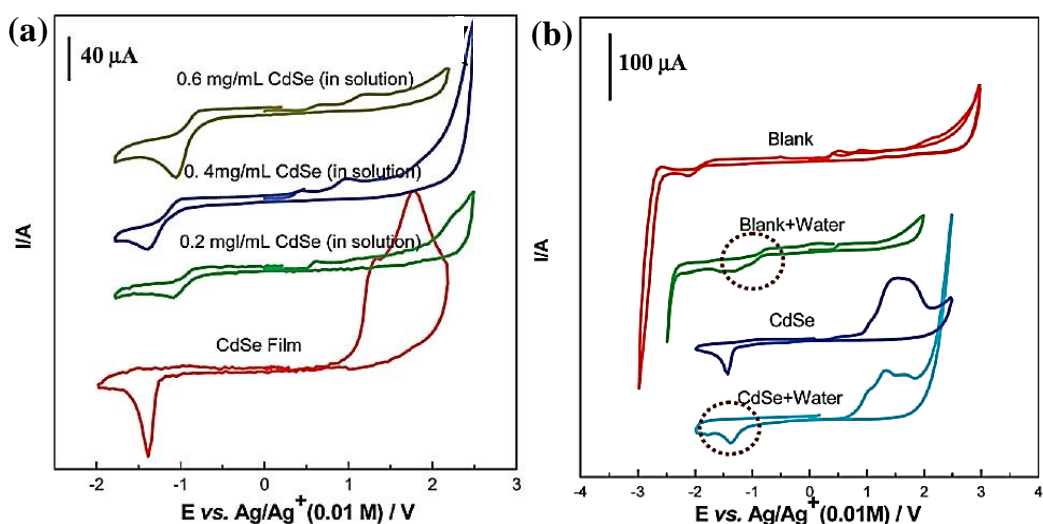
Figure 1.6: (a) Results of CV experiments in solution-based and in thin film-based; (b) Effect of water in the electrolyte solution and its significant effect towards electrochemical signal.[34]

Again, they examined the fate of electrochemical signals of NCs with respect to the extent of washing and without washing. The proper washing of NCs led to a significant improvement in the quality of the signal as compared to crude NCs (without washing) as shown in figure 1.7. (a). The poor electrochemical signals in the case of crude CdSe NCs were attributed to the presence of unreacted ligands. Also, they studied the effect of thickness of CdSe NCs on the thin film-based as shown in figure.1.7. (b). Based on the experimental results, they concluded that the NCs with an appropriate film on the electrode displayed a clean and distinct electrochemical signal. However, the too thin and thick film gave negative results (poor signals).
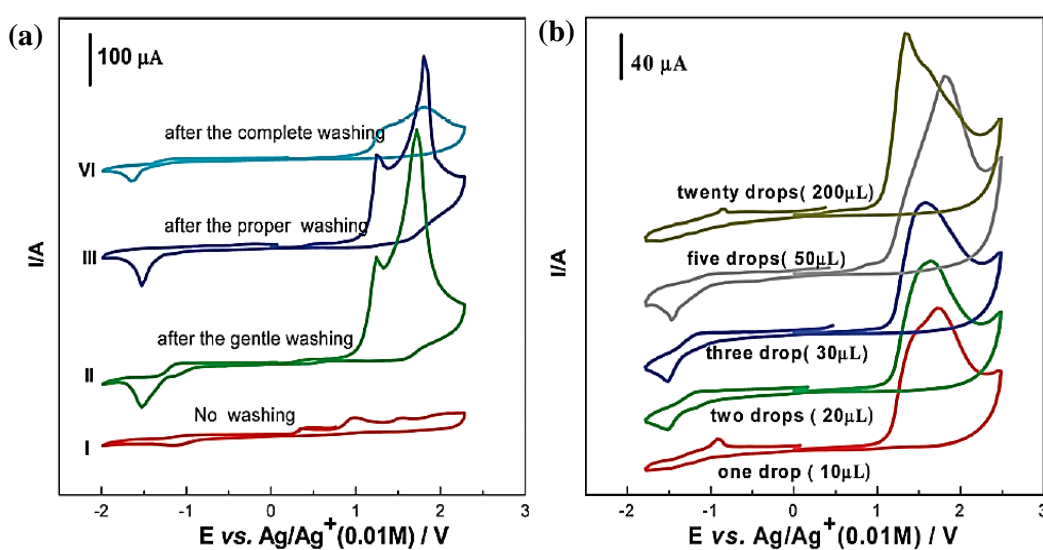
Figure 1.7: Comparative effect on electrochemical signal displayed by NCs (a) effect of various extent of washing (b) effect of thickness of film on the working electrode.[34]

Furthermore, they performed the CV experiments to evaluate the effect of the size of CdSe NCs on their band edge energy levels and figured out that the onset potentials of both cathodic and anodic peak were shifted towards more negative and positive potential respectively with the decrease in the particle size. Lastly, they investigated the influence of capping ligands on the band structure of CdSe NCs and noticed the considerable change in the electrochemical bandgap as shown in the figure: 1.8. (a) and (b).
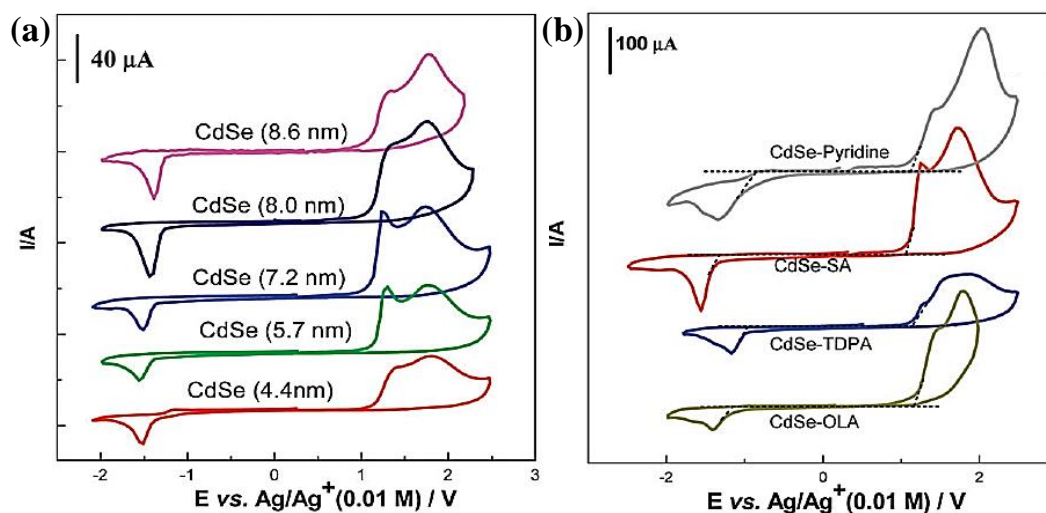
Figure 1.8: (a) Effect of different size of NCs on their respective band edge position, (b) cyclic voltammogram of CdSe with different capping ligand such as pyridine (PY); Stearic acid (SA); tetradecylphosphonic acid (TDPA) and oleyl amine (OLA) respectively.[34]

The presence of the pyridine (Py) and stearic acid (SA) coated NCs showed the lowest (2.02 eV) and highest (2.35 eV) bandgap values respectively. Therefore, they concluded that the size of NCs and the presence of various capping ligands on the surface of NCs could efficiently modulate the band-gap of NCs to a large extent.

In **2016**, Nag *et. al.* reported the electrochemical investigation of the colloidal nanocrystal, predominantly, all inorganic cesium lead halide ($CsPbX_3$, where X = Cl, Br and I) perovskites.[25] These NCs were first reported by Protesescu *et al.*[115] in the year 2015 and have been widely used in light-emitting diodes and other optoelectronic devices. Such exceptional optoelectronic properties could be attributed to the nature of valence band edge, conduction band edge, and optical transition across these edges. The CV experiments were used to study the systematic variation of these band edges in the solution phase at room temperature and ambient atmospheric conditions. The electrochemical properties of $CsPbBr_3$ NCs were studied by dispersing them into a 1:4

v/v acetonitrile and toluene solution in a 50 mM TBAP with a scan rate of 50 mVs^{-1} as shown in figure 1.9.
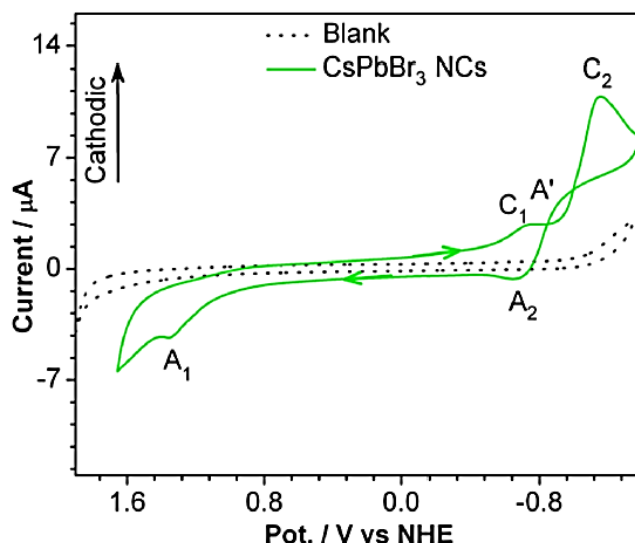
Figure 1.9: (a) Cyclic voltammogram of CsPbBr$_3$ QDs dispersed in 50 mM TBAP 1:4 v/v acetonitrile and toluene solution.[25]

The peak potential difference between the point A1 and C2 are 2.50 V which was very close to the optical band-gap of 2.48 eV. This result led them to conclude that the A$_1$ (anodic peak) and C$_2$ (cathodic peak) were the points where the electron transfer between the NCs and the electrode interface took place. The anion exchange reactions were carried out by employing PbX$_2$ salts following the reported protocol[115–117] to investigate the effect of halide composition to achieve a systematic variation in the optical band gap and electrochemical bandgap from blue to red without changing the size of NCs as shown in figure 1.10.
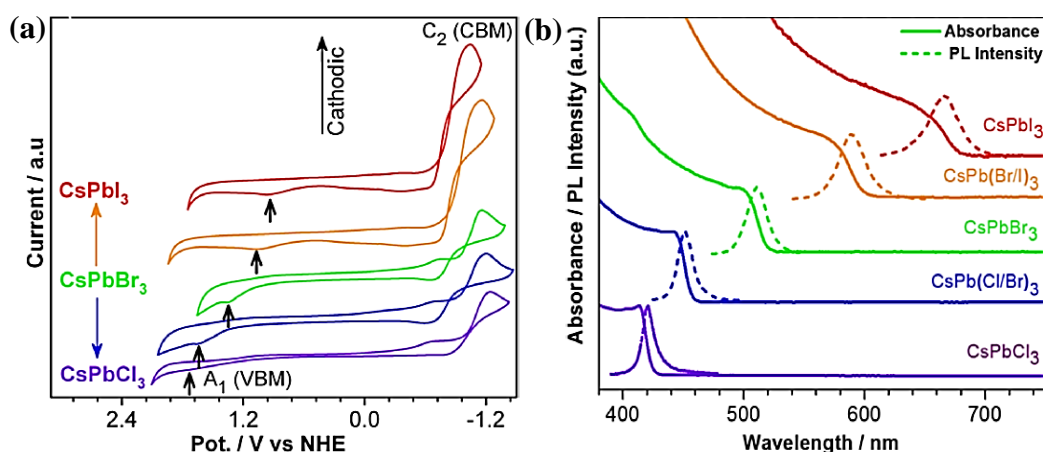
Figure 1.10: (a) Cyclic voltammogram curve of CsPbX$_3$ NCs with different halide composition; (b) UV-visible absorption and PL spectra of CsPbX$_3$ (X= Cl, Br and I) showing the tunable optical gap across the visible region.[25]

They found that the optoelectronic properties of this material vary from Cl to Br to I with a significant shift in VBM by 0.80 eV whereas the shift in CBM is small by 0.19 eV. Based on these experimental results, they concluded that VBM played a vital role in tuning the optical bandgap covering the entire visible region by systematic variation of halide composition but the shift towards CBM with halide composition is small.

In **2017**, Zakhidov *et. al.* reported the effect of various solvents on the electrochemical properties of hybrid organic-inorganic perovskite films, especially, methylammonium lead iodide perovskites.[26] Several solvents such as isopropanol (IPA), dimethylformamide (DMF), water, acetonitrile, toluene, hydrofluoroethers of type 7100 and 7300 (HFEs), and diethyl carbonate (DEC) were screened. Among them, HFE-7100 (a mixture of isomers: methyl nonafluoroisobutyl ether and methyl nonafluorobutyl ether) turned out to be the best solvent. The small amount of DEC (~3 volume %) along with bis (trifluoromethane) sulfonamide lithium (LiTFSI) salt were added to enhance the conductivity of HFE electrolyte. The CV experiments were performed by using coated-thin film (400 nm thick) of $CH_3NH_3PbI_3$ with indium tin oxide (ITO) as a working electrode and lithium metal as a reference electrode with a scan rate of 10 mVs^{-1}. The anodic and cathodic current (IPA = 2.8 x 10^{-7} A and IPC = 1.5 x 10^{-7} A) were noted at 4.96 V and 4.65 V respectively as shown in figure 1.11. The observed redox peak was attributed to the oxidation of $CH_3NH_3PbI_3$/ITO but not due to the redox reaction of ITO in the HFE electrolyte.
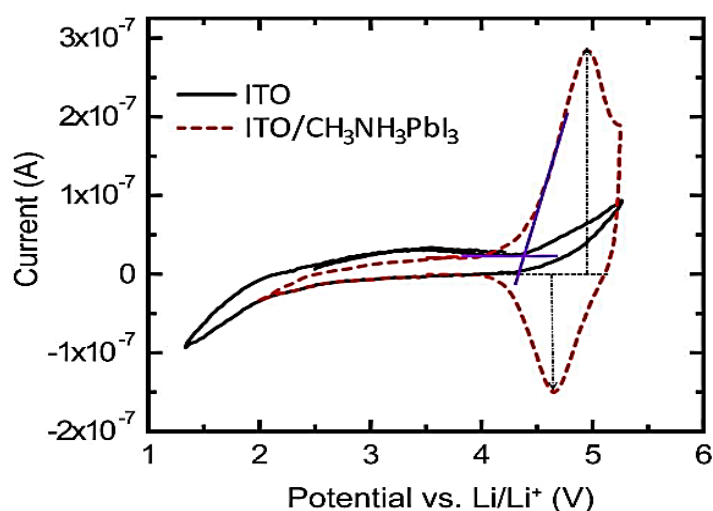
Figure 1.11: (a) Cyclic voltammogram of $CH_3NH_3PbI_3$/ITO and bare ITO represented by the dotted line and solid line respectively.[26]

In **2018**, Janaky *et. al.* showcased the boundary conditions for the electrochemical analysis of cesium lead bromide ($CsPbBr_3$) and the hybrid organic-inorganic methylammonium lead iodide ($MAPbI_3$) perovskites NCs.[118] The stability window for both $CsPbBr_3$ and $MAPbI_3$ NCs at around -1.0 to +0.6 V and -0.65 to +0.55 V respectively were reported. The CV study was performed under inert atmospheric condition by modifying the working electrode with titanium oxide coated with a thin film of fluorine-doped tin oxide (FTO) in an electrolyte solution consisting of DCM solvent and $TBAPF_6$ as the supporting electrolyte. The thin film-based $CsPbBr_3$ NCs and $MAPbI_3$ NCs exhibited stability for up to 2 h and 1 h respectively in DCM solvent. Various analytical techniques such as XRD, XPS, SEM-EDX were employed to analyse the driving force for the generation of the observed redox peaks. The noticeable redox signals were due to the oxidation and reduction of Pb to Pb^{+2} and vice-versa as shown by the following plausible reactions.

Oxidation:

$$CsPbBr_3 - e^- \longrightarrow PbBr_2 + Cs^+ + 0.5\ Br_2$$

$$PbBr_2 - 2e^- \longrightarrow Pb^{+2} + Br_2$$

Reduction:

$$CsPbBr_3 + 2e^- \longrightarrow Pb + Cs^+ + 3Br^-$$
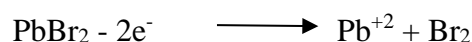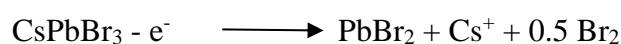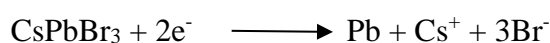
Figure 1.12: Plausible redox reaction of cesium lead bromide QDs during electrochemical investigation.[118]

In **2018**, Garcia-Gutierrez *et. al.* synthesized lead sulfide (PbS) nanocrystal of varying size-distribution in the presence of the different capping ligands such as oleic acid, myristic acid, and hexanoic acid.[98] In this work, the authors demonstrated the influence of the nature of capping ligands and quantum size effect of NCs on the relative positions of band energy levels of NCs (HOMO and LUMO). The shift in the relative positions of HOMO and LUMO of PbS NCs was attributed to the different atomistic arrangement surface of NCs and phonon vibrations with the various capping ligand. They proposed that the anodic oxidation signal was due to the dissolution of PbS nanocrystal whereas the reduction signal was attributed to the cathodic reduction of Pb^{+2} to Pb^0.

References

(1)   Parida, B.; Iniyan, S.; Goic, R. A Review of Solar Photovoltaic Technologies. *Renew. Sustain. Energy Rev.* **2011**, *15*, 1625–1636.

(2)   Asim, N.; Sopian, K.; Ahmadi, S.; Saeedfar, K.; Alghoul, M. A.; Saadatian, O.; Zaidi, S. H. A Review on the Role of Materials Science in Solar Cells. *Renew. Sustain. Energy Rev.* **2012**, *16*, 5834–5847.

(3)   Etgar, L. Semiconductor Nanocrystals as Light Harvesters in Solar Cells. *Materials* **2013**, *6*, 445–459.

(4)   Mora-Seró, I.; Bisquert, J. Breakthroughs in the Development of Semiconductor-Sensitized Solar Cells. *J. Phys. Chem. Lett.* **2010**, *1*, 3046–3052.

(5)   Chapin, D. M.; Fuller, C. S.; Pearson, G. L. A New Silicon P-n Junction Photocell for Converting Solar Radiation into Electrical Power. *J. Appl. Phys.* **1953**, *25*, 676–677.

(6)   Ramanujam, J.; Singh, U. P. Copper Indium Gallium Selenide Based Solar Cells - A Review. *Energy Environ. Sci.* **2017**, *10*, 1306–1319.

(7)   Hagfeldt, A.; Boschloo, G.; Sun, L.; Kloo, L.; Pettersson, H. Dye-Sensitized Solar Cells. *Chem. Rev.* **2010**, *110*, 6595–6663.

(8)   Zhou, D.; Zhou, T.; Tian, Y.; Zhu, X.; Tu, Y. Perovskite-Based Solar Cells: Materials, Methods, and Future Perspectives. *J. Nanomater.* **2018**, *8*, 1–15.

(9)   Yan, J.; Saunders, B. R. Third-Generation Solar Cells: A Review and Comparison of Polymer: Fullerene, Hybrid Polymer and Perovskite Solar Cells. *RSC Adv.* **2014**, *4*, 43286–43314.

(10)   Conibeer, G. Third-Generation Solar Cells. *Sol. Cell Mater. Dev. Technol.* **2014**, *16*, 283–314.

(11)   Yao, H.; Cui, Y.; Qian, D.; Ponseca, C. S.; Honarfar, A.; Xu, Y.; Xin, J.; Chen, Z.; Hong, L.; Gao, B.; Yu, R.; Zu, Y.; Ma, W.; Chabera, P.; Pullerits, T.; Yartsev, A.; Gao, F.; Hou, J. 14.7% Efficiency Organic Photovoltaic Cells Enabled by Active Materials with a Large Electrostatic Potential Difference. *J. Am. Chem. Soc.* **2019**, *141*, 7743–7750.

(12)   Heinrichová, P.; Pospíšil, J.; Stříteský, S.; Vala, M.; Weiter, M.; Toman, P.; Rais, D.; Pfleger, J.; Vondráček, M.; Šimek, D.; Fekete, L.; Horáková, P.; Dokládalová, L.; Kubáč, L.; Kratochvílová, I. Diketopyrrolopyrrole-Based Organic Solar Cells Functionality: The Role of Orbital Energy and Crystallinity. *J. Phys. Chem. C* **2019**, *123*, 11447–11463.

(13)   Kan, B.; Zhang, Q.; Li, M.; Wan, X.; Ni, W.; Long, G.; Wang, Y.; Yang, X.; Feng, H.; Chen, Y. Solution-Processed Organic Solar Cells Based on Dialkylthiol-Substituted Benzodithiophene Unit with Efficiency near 10%. *J. Am. Chem. Soc.* **2014**, *136*, 15529–15532.

(14)   Huang, C.; Liao, X.; Gao, K.; Zuo, L.; Lin, F.; Shi, X.; Li, C. Z.; Liu, H.; Li, X.; Liu, F.; Chen, Y.; Chen, H.; Jen, A. K. Y. Highly Efficient Organic Solar Cells Based on S, N-Heteroacene Non-Fullerene Acceptors. *Chem. Mater.* **2018**, *30*, 5429–5434.

(15)   Lee, T. D.; Ebong, A. U. A Review of Thin Film Solar Cell Technologies and Challenges. *Renew. Sustain. Energy Rev.* **2017**, *70*, 1286–1297.

(16)   Gong, J.; Sumathy, K.; Qiao, Q.; Zhou, Z. Review on Dye-Sensitized Solar Cells (DSSCs): Advanced Techniques and Research Trends. *Renew. Sustain. Energy Rev.* **2017**, *68*, 234–246.

(17)   Mathew, S.; Yella, A.; Gao, P.; Humphry-baker, R.; Curchod, B. F. E.; Ashari-astani, N.; Tavernelli, I.; Rothlisberger, U.; Nazeeruddin, K.; Gra, M. Dye-Sensitized Solar Cells with 13% Efficiency Achieved through the Molecular Engineering of Porphyrin Sensitizers. *Nat. Chem.* **2014**, *6*, 242–247.

(18)   Pan, Z.; Rao, H.; Mora-sero, I.; Bisquert, J.; Zhong, X. Quantum Dot-Sensitized Solar Cells. *Chem. Soc. Rev.* **2018**, *47*, 7659–7702.

(19)   Ramade, J.; Qu, J.; Chu, A.; Gréboval, C.; Livache, C.; Goubet, N.; Martinez, B.; Vincent, G.; Lhuillier, E. Potential of Colloidal Quantum Dot Based Solar Cells for Near-Infrared Active Detection. *ACS Photonics* **2020**, *7*, 272–278.

(20)   Chebrolu, V. T.; Kim, H. J. Recent Progress in Quantum Dot Sensitized Solar Cells: An Inclusive Review of Photoanode, Sensitizer, Electrolyte, and the Counter Electrode. *J. Mater. Chem. C* **2019**, *7*, 4911–4933.

(21)   Koster, L. J. A.; Mihailetchi, V. D.; Blom, P. W. M.; Koster, L. J. A.; Mihailetchi, V. D.; Blom, P. W. M. Ultimate Efficiency of Polymer / Fullerene Bulk Heterojunction Solar Cells. *Appl. Phys. Lett.* **2006**, *88*, 093511–09353.

(22)   Park, N. G. Perovskite Solar Cells: An Emerging Photovoltaic Technology. *Mater. Today* **2015**, *18*, 65–72.

(23)   Im, J.; Lee, C.; Lee, J.; Park, S.; Park, N. 6.5% Efficient Perovskite Quantum-Dot-Sensitized Solar Cell. *Nanoscale* **2011**, *3*, 4088–4093.

(24)   Manser, J. S.; Christians, A.; Kamat, P. V. Intriguing Optoelectronic Properties of Metal Halide Perovskites. *Chem. Rev.* **2016**, *116*, 12956–13008.

(25)   Ravi, V. K.; Markad, G. B.; Nag, A. Band Edge Energies and Excitonic Transition Probabilities of Colloidal $CsPbX_3$ (X = Cl, Br, I) Perovskite Nanocrystals. *ACS Energy Lett.* **2016**, *1*, 665–671.

(26)   Hasan, M.; Venkatesan, S.; Lyashenko, D. A.; Slinker, J. D.; Zakhidov, A. A Solvent Toolkit for Electrochemical Characterization of Hybrid Perovskite Films. *Anal. Chem.* **2017**, *89*, 9649–9653.

(27)   Song, J.; Li, J.; Li, X.; Xu, L.; Dong, Y.; Zeng, H. Quantum Dot Light-Emitting Diodes Based on Inorganic Perovskite Cesium Lead Halides ($CsPbX_3$). *Adv. Mater* **2015**, *27*, 7162–7167.

(28)   Green, M. A.; Ho-baillie, A.; Snaith, H. J. The Emergence of Perovskite Solar Cells. *Nat. Photonics* **2014**, *8*, 506–513.

(29)   Sum, T. C.; Mathews, N. Advancements in Perovskite Solar Cells: Photophysics behind the Photovoltaics. *Energy Environ. Sci.* **2014**, *7*, 2518–2534.

(30)   Snaith, H. J. Perovskites: The Emergence of a New Era for Low-Cost, High-Efficiency Solar Cells. *J. Phys. Chem. Lett.* **2013**, *4*, 3623–3630.

(31)   Chang, J.; Waclawik, E. R. Colloidal Semiconductor Nanocrystals : Controlled Synthesis and Surface Chemistry in Organic Media. *RSC Adv.* **2014**, *4*, 23505–23527.

(32)   Poznyak, S. K.; Osipovich, N. P.; Shavel, A.; Talapin, D. V; Gao, M.; Eychmu, A.; Gaponik, N. Size-Dependent Electrochemical Behavior of Thiol-Capped

CdTe Nanocrystals in Aqueous Solution. *J. Phys. Chem. B* **2005**, *109*, 1094–1100.

(33) Hines, M. A.; Scholes, G. D. Colloidal PbS Nanocrystals with Size-Tunable Near-Infrared Emission : Observation of Post- Synthesis Self-Narrowing of the Particle Size Distribution. *Adv. Mater.* **2003**, *15*, 1844–1849.

(34) Liu, J.; Yang, W.; Li, Y.; Fan, L.; Li, Y. Electrochemical Studies of the Effects of the Size, Ligand and Composition on the Band Structures of CdSe, CdTe and Their Alloy Nanocrystals. *Phys. Chem. Chem. Phys.* **2014**, *16*, 4778–4788.

(35) Yong, K.; Sahoo, Y.; Swihart, M. T.; Prasad, P. N. Shape Control of CdS Nanocrystals in One-Pot Synthesis. *J. Phys. Chem. C* **2007**, *111*, 2447–2458.

(36) Jeon, N. J.; Noh, J. H.; Yang, W. S.; Kim, Y. C.; Ryu, S.; Seo, J.; Seok, S. Il. Compositional Engineering of Perovskite Materials for High-Performance Solar Cells. *Nature* **2015**, *517*, 476–480.

(37) Imran, M.; Caligiuri, V.; Wang, M.; Goldoni, L.; Prato, M.; Krahne, R.; De Trizio, L.; Manna, L. Benzoyl Halides as Alternative Precursors for the Colloidal Synthesis of Lead-Based Halide Perovskite Nanocrystals. *J. Am. Chem. Soc.* **2018**, *140*, 2656–2664.

(38) Zhou, Y.; Zhu, K. Perovskite Solar Cells Shine in the "Valley of the Sun." *ACS Energy Lett.* **2016**, *1*, 64–67.

(39) Swarnkar, A.; Marshall, A. R.; Sanehira, E. M.; Chernomordik, B. D.; Moore, D. T.; Christians, J. A.; Chakrabarti, T.; Luther, J. M. Quantum Dot – Induced Phase Stabilization of a -CsPbI 3 Perovskite for High-Efficiency Photovoltaics. *Science* **2016**, *354*, 92–95.

(40) Gao, G.; Xi, Q.; Zhou, H.; Zhao, Y.; Wu, C.; Wang, L.; Guo, P.; Xu, J. Novel Inorganic Perovskite Quantum Dots for Photocatalysis. *Nanoscale* **2017**, *9*, 12032–12038.

(41) Samu, G. F.; Scheidt, R. A.; Kamat, P. V. Electrochemistry and Spectroelectrochemistry of Lead Halide Perovskite Films: Materials Science Aspects and Boundary Conditions. *Chem. Mater.* **2018**, *30*, 561–569.

(42) Inamdar, S. N.; Ingole, P. P.; Haram, S. K. Determination of Band Structure

Parameters and the Quasi-Particle Gap of CdSe Quantum Dots by Cyclic Voltammetry. *ChemPhysChem* **2008**, *9*, 2574–2579.

(43)   Smith, A. M.; Nie, S. Semiconductor Nanocrystals : Structure, Properties, and Band Gap Engineering. *Acc. Chem. Res.* **2009**, *43*, 190–200.

(44)   Van Hecke, M. Semiconductor Nanocrystal. *Science* **2007**, *317*, 49–50.

(45)   Dong, Y.; Qiao, T.; Kim, D.; Parobek, D.; Rossi, D.; Son, D. H. Precise Control of Quantum Confinement in Cesium Lead Halide Perovskite Quantum Dots via Thermodynamic Equilibrium. *Nano Lett.* **2018**, *18*, 3716–3722.

(46)   Yarema, M.; Yarema, O.; Lin, W. M. M.; Volk, S.; Yazdani, N.; Bozyigit, D.; Wood, V. Upscaling Colloidal Nanocrystal Hot-Injection Syntheses via Reactor Underpressure. *Chem. Mater.* **2017**, *29*, 796–803.

(47)   Williams, J. V.; Kotov, N. A.; Savage, P. E. Materials and Interfaces a Rapid Hot-Injection Method for the Improved Hydrothermal Synthesis of CdSe Nanoparticles. *Ind. Eng. Chem. Res.* **2009**, *48*, 4316–4321.

(48)   Liu, M.; Matuhina, A.; Zhang, H.; Vivo, P. Advances in the Stability of Halide Perovskite Nanocrystals. *Materials* **2019**, *12*, 1–37.

(49)   Lee, D.; Kim, M. H.; Woo, H. Y.; Chae, J.; Lee, D.; Jeon, S.; Oh, S. J.; Paik, T. Heating-up Synthesis of Cesium Bismuth Bromide Perovskite Nanocrystals with Tailored Composition, Morphology, and Optical Properties. *RSC Adv.* **2020**, *10*, 7126–7133.

(50)   Cui, J.; Wang, L.; Yu, X. A Simple and Generalized Heat-up Method for the Synthesis of Metal Sulfide Nanocrystals. *New J. Chem.* **2019**, *43*, 16007–16011.

(51)   Van Embden, J.; Chesman, A. S. R.; Jasieniak, J. J. The Heat-up Synthesis of Colloidal Nanocrystals. *Chem. Mater.* **2015**, *27*, 2246–2285.

(52)   Thanh, N. T. K.; Maclean, N.; Mahiddine, S. Mechanisms of Nucleation and Growth of Nanoparticles in Solution. *Chem. Rev.* **2014**, *114*, 7610–7630.

(53)   Thapa, S.; Bhardwaj, K.; Basel, S.; Pradhan, S.; Eling, C. J.; Adawi, A. M.; Bouillard, J. S. G.; Stasiuk, G. J.; Reiss, P.; Pariyar, A.; Tamang, S. Long-Term Ambient Air-Stable Cubic $CsPbBr_3$ Perovskite Quantum Dots Using Molecular

Bromine. *Nanoscale Adv.* **2019**, *1*, 3388–3391.

(54)   Murray, C. B.; Noms, D. J.; Bawendi, M. G. Synthesis and Characterization of Nearly Monodisperse CdE (E = S, Se, Te) Semiconductor Nanocrystallites. *J. Am. Chem. Soc.* **1993**, *115*, 8706–8715.

(55)   Talapin, D. V; Rogach, A. L.; Kornowski, A.; Haase, M.; Weller, H. Highly Luminescent Monodisperse CdSe and CdSe / ZnS Nanocrystals Synthesized in a Hexadecylamine − Trioctylphosphine Oxide − Trioctylphospine Mixture. *Nano Lett.* **2001**, *1*, 207–211.

(56)   Blackman, B.; Battaglia, D. M.; Mishima, T. D.; Johnson, M. B.; Peng, X. Control of the Morphology of Complex Semiconductor Nanocrystals with a Type II Heterojunction, Dots vs Peanuts, by Thermal Cycling. *Chem. Mater* **2007**, *19*, 3815–3821.

(57)   Peng, Z. A.; Peng, X. Nearly Monodisperse and Shape-Controlled CdSe Nanocrystals via Alternative Routes: Nucleation and Growth. *J. Am. Chem. Soc.* **2002**, *124*, 3343–3353.

(58)   Steigerwald, M. L.; Gibson, M.; Harris, D.; Kortan, R.; Muller, A. J.; Duncan, T. M.; Douglass, D. C.; Brus, L. E. Surface Derivatization and Isolation of Semiconductor Cluster Molecules. *J. Am. Chem. Soc.* **1988**, *110*, 3046–3050.

(59)   Haram, S. K.; Quinn, B. M.; Bard, A. J. Electrochemistry of CdS Nanoparticles : A Correlation between Optical and Electrochemical Band Gaps. *J. Am. Chem. Soc.* **2001**, *123*, 8860–8861.

(60)   Querner, C.; Reiss, P.; Sadki, S.; Zagorska, M.; Pron, A. Size and Ligand Effects on the Electrochemical and Spectroelectrochemical Responses of CdSe Nanocrystals. *Phys.Chem.Chem. Phys* **2005**, *7*, 3204 –3209.

(61)   Brus, L. E. Electron – Electron and Electronhole Interactions in Small Semiconductor Crystallites : The Size Dependence of the Lowest Excited Electronic State Electron-Electron and Electron-Hole Interactions in Small Semiconductor Crystallites : The Size Dependence O. *J. Chem. Phys.* **1984**, *80*, 4403–4409.

(62)   Tamang, S.; Lincheneau, C.; Hermans, Y.; Jeong, S.; Reiss, P. Chemistry of InP

Nanocrystal Syntheses. *Chem. Mater.* **2016**, *28*, 2491−2506.

(63)   Talapin, D. V; Rogach, A. L.; Shevchenko, E. V; Kornowski, A.; Haase, M.; Weller, H. Dynamic Distribution of Growth Rates within the Ensembles of Colloidal II - VI and III - V Semiconductor Nanocrystals as a Factor Governing Their Photoluminescence Efficiency. *J. Am. Chem. Soc.* **2002**, *124*, 5782–5790.

(64)   Micic, O.; Curtis, C. J.; Jones, K. M.; Sprague, J. R.; Nozik, A. J. Synthesis and Characterization of InP Quantum Dots. *J. Phys. Chem* **1994**, *98*, 4966–4969.

(65)   Battaglia, D.; Peng, X. Formation of High Quality InP and InAs Nanocrystals in a Noncoordinating Solvent. *Nano Lett* **2002**, *9*, 1027–1030.

(66)   Lin, W.; Fritz, K.; Guerin, G.; Bardajee, G. R.; Hinds, S.; Sukhovatkin, V.; Sargent, E. H.; Scholes, G. D.; Winnik, M. A. Highly Luminescent Lead Sulfide Nanocrystals in Organic Solvents and Water through Ligand Exchange with Poly (Acrylic Acid). *Langmuir* **2008**, *24*, 8215–8219.

(67)   Lee, S.; Jun, Y.; Cho, S.; Cheon, J. Single-Crystalline Star-Shaped Nanocrystals and Their Evolution : Programming the Geometry of Nano-Building Blocks. *J. Am. Chem. Soc.* **2002**, *124*, 11244–11245.

(68)   Cademartiri, L.; Bertolotti, J.; Sapienza, R.; Wiersma, D. S.; Freymann, G. Von; Ozin, G. A. Multigram Scale, Solventless, and Diffusion-Controlled Route to Highly Monodisperse PbS Nanocrystals. *J. Phys. Chem. B* **2006**, *110*, 671–673.

(69)   Talapin, D. V; Murray, C. B. PbSe Nanocrystal Solids for N- and p-Channel Thin Film Field-Effect Transistors. *Science* **2005**, *310*, 86–88.

(70)   Urban, J. J.; Talapin, D. V; Shevchenko, E. V; Murray, C. B. Self-Assembly of PbTe Quantum Dots into Nanocrystal Superlattices and Glassy Films. *J. Am. Chem. Soc.* **2006**, *128*, 3248–3255.

(71)   Ha, S. T.; Su, R.; Xing, J.; Zhang, Q.; Xiong, Q. Metal Halide Perovskite Nanomaterials: Synthesis and Applications. *Chem. Sci.* **2017**, *8*, 2522–2536.

(72)   Chen, D.; Chen, X. Luminescent Perovskite Quantum Dots: Synthesis, Microstructures, Optical Properties and Applications. *J. Mater. Chem. C* **2019**, *7*, 1413–1446.

(73)   James, C. Featured Graphic. Lives on the Line: Mapping Life Expectancy along the London Tube Network. *Environ. Plan. A* **2012**, *44*, 1525–1528.

(74)   Swarnkar, A.; Ravi, V. K.; Nag, A. Beyond Colloidal Cesium Lead Halide Perovskite Nanocrystals: Analogous Metal Halides and Doping. *ACS Energy Lett.* **2017**, *2*, 1089–1098.

(75)   Zhang, C.; Wang, B.; Wan, Q.; Kong, L.; Zheng, W.; Li, Z.; Li, L. Critical Role of Metal Ions in Surface Engineering toward Brightly Luminescent and Stable Cesium Lead Bromide Perovskite Quantum Dots. *Nanoscale* **2019**, *11*, 2602–2607.

(76)   Akkerman, Q. A.; Martínez-Sarti, L.; Goldoni, L.; Imran, M.; Baranov, D.; Bolink, H. J.; Palazon, F.; Manna, L. Molecular Iodine for a General Synthesis of Binary and Ternary Inorganic and Hybrid Organic-Inorganic Iodide Nanocrystals. *Chem. Mater.* **2018**, *30*, 6915–6921.

(77)   Akkerman, Q. A.; Rainò, G.; Kovalenko, M. V.; Manna, L. Genesis, Challenges and Opportunities for Colloidal Lead Halide Perovskite Nanocrystals. *Nat. Mater.* **2018**, *17*, 394–405.

(78)   Kojima, A.; Teshima, K.; Shirai, Y.; Miyasaka, T. Organometal Halide Perovskites as Visible-Light Sensitizers for Photovoltaic Cells. *J. Am. Chem. Soc.* **2009**, *131*, 6050–6051.

(79)   Singh, S. P.; Nagarjuna, P. Organometal Halide Perovskites as Useful Materials in Sensitized Solar Cells. *Dalt. Trans.* **2014**, *43*, 5247–5251.

(80)   Lee, M. M.; Teuscher, J.; Miyasaka, T.; Murakami, T. N.; Snaith, H. J. Efficient Hybrid Solar Cells Based on Meso-Superstructured Organometal Halide Perovskitesfile. *Science* **2012**, *338*, 643–646.

(81)   Kim, H.; Lee, C.; Im, J.; Lee, K.; Moehl, T.; Marchioro, A.; Moon, S.; Humphry-baker, R.; Yum, J.; Moser, J. E.; Gra, M. Lead Iodide Perovskite Sensitized All-Solid-State Submicron Thin Film Mesoscopic Solar Cell with Efficiency Exceeding 9%. *Sci. Rep.* **2012**, *591*, 1–7.

(82)   Chung, I.; Lee, B.; He, J.; Chang, R. P. H.; Kanatzidis, M. G. All-Solid-State Dye-Sensitized Solar Cells with High Efficiency. *Nature* **2012**, *485*, 486–489.

(83) Gra, M. Sequential Deposition as a Route to High-Performance Perovskite-Sensitized Solar Cells. *Nature* **2013**, *499*, 316–319.

(84) Zhou, H.; Chen, Q.; Li, G.; Luo, S.; Song, T.; Duan, H.-S.; Hong, Z.; You, J.; Liu, Y.; Yang, Y. Interface Engineering of Highly Efficient Perovskite Solar Cells Huanping. *Science* **2014**, *345*, 542–546.

(85) Stoumpos, C. C.; Malliakas, C. D.; Kanatzidis, M. G. Semiconducting Tin and Lead Iodide Perovskites with Organic Cations: Phase Transitions, High Mobilities, and Near-Infrared Photoluminescent Properties. *Inorg. Chem.* **2013**, *15*, 9019–9038.

(86) Kojima, A.; Teshima, K.; Shirai, Y.; Miyasaka, T. Organometal Halide Perovskites as Visible-Light Sensitizers for Photovoltaic. *J. Am. Chem. Soc.* **2009**, *131*, 6050–6051.

(87) Luan, M.; Song, J.; Wei, X.; Chen, F.; Liu, J. Controllable Growth of Bulk Cubic-Phase $CH_3NH_3PbI_3$ Single Crystal with Exciting Room-Temperature Stability. *Cryst Eng Comm* **2016**, *18*, 5257–5261.

(88) Li, G.; Wisnivesky, F.; Rivarola, R.; Davis, N. J. L. K.; Bai, S.; Jellicoe, T. C.; Peña, F. De; Hou, S.; Ducati, C.; Gao, F.; Friend, R. H.; Greenham, N. C.; Tan, Z. Highly Efficient Perovskite Nanocrystal Light-Emitting Diodes Enabled by a Universal Crosslinking Method. *Adv. Mater.* **2016**, *28*, 3528–3534.

(89) Li, X.; Wang, Y.; Sun, H.; Zeng, H. Amino-Mediated Anchoring Perovskite Quantum Dots for Stable and Low-Threshold Random Lasing. *Adv. Mater.* **2017**, *29*, 1701185-1701194.

(90) Huang, C.; Zou, C.; Mao, C.; Corp, K. L.; Yao, Y.; Lee, Y.; Schlenker, C. W.; Jen, A. K. Y.; Lin, L. Y. $CsPbBr_3$ Perovskite Quantum Dot Vertical Cavity Lasers with Low Threshold and High Stability. *ACS Photonics* **2017**, *4*, 2281−2289.

(91) Yakunin, S.; Sytnyk, M.; Kriegner, D.; Shrestha, S.; Richter, M.; Matt, G. J.; Azimi, H.; Brabec, C. J.; Stangl, J.; Kovalenko, M. V; Heiss, W. Detection of X-Ray Photons by Solution-Processed Lead Halide Perovskites. *Nat. Photonics* **2015**, *9*, 444–449.

(92)   Jasieniak, J.; Califano, M.; Watkins, S. E. Size-Dependent Valence and Conduction Band-Edge Energies of Semiconductor Nanocrystals. *ACS Nano* **2011**, *5*, 5888–5902.

(93)   Sakai, N.; Ebina, Y.; Takada, K.; Sasaki, T. Electronic Band Structure of Titania Semiconductor Nanosheets Revealed by Electrochemical and Photoelectrochemical Studies. *J. Am. Chem. Soc.* **2004**, *126*, 5851–5858.

(94)   Li, B. Y.; Zhong, H.; Li, R.; Zhou, Y.; Yang, C.; Li, Y. High-Yield Fabrication and Electrochemical Characterization of Tetrapodal CdSe , CdTe , and CdSe$_x$ Te$_{1-x}$ Nanocrystals. *Adv. Funct. Mater.* **2006**, *16*, 1705–1716.

(95)   Jiang, F.; Li, Y.; Ye, M.; Fan, L.; Ding, Y.; Li, Y. Ligand-Tuned Shape Control , Oriented Assembly , and Electrochemical Characterization of Colloidal ZnTe Nanocrystals. *Chem. Mater.* **2010**, *22*, 4632–4641.

(96)   Brandt, R. E.; Stevanovic, V.; Ginley, D. S. G.; Buonassisi, T. Identifying Defect-Tolerant Semiconductors with High Minority-Carrier Lifetimes : Beyond Hybrid Lead Halide Perovskites. *MRS Commun.* **2015**, *5*, 265–275.

(97)   Garcia-gutierrez, D. F.; Hernandez-casillas, L. P.; Cappellari, M. V.; Fungo, F.; Mart, E.; Ixcoatl, D. Influence of the Capping Ligand on the Band Gap and Electronic Levels of PbS Nanoparticles through Surface Atomistic Arrangement Determination. *ACS Omega* **2018**, *3*, 393–405.

(98)   Leonat, L.; Sbarcea, G.; Branzoi, I. V. Cyclic Voltammetry For Energy Levels Estimation Of Organic Materials. *U.P.B. Sci. Bull* **2013**, *75*, 1454–2331.

(99)   Davis, R. J.; Lloyd, M. T.; Ferreira, S. R.; Bruzek, M. J.; Watkins, S. E.; Lindell, L.; Sehati, P.; Fahlman, M.; Anthony, J. E.; Hsu, J. W. P. Determination of Energy Level Alignment at Interfaces of Hybrid and Organic Solar Cells under Ambient Environment. *J. Mater. Chem.* **2011**, *21*, 1721–1729.

(100) Lupo, M. G.; Sala, F. D.; Carbone, L.; Zavelani-Rossi, M.; Fiore, A.; Lüer, L.; Polli, D.; Cingolani, R.; Manna, L.; Lanzani, G. Ultrafast Electron-Hole Dynamics in Core/Shell CdSe/CdS Dot/Rod Nanocrystals. *Nano Lett.* **2008**, *8*, 4582–4587.

(101) Soreni-Harari, M.; Yaacobi-Gross, N.; Steiner, D.; Aharoni, A.; Banin, U.;

Millo, O.; Tessler, N. Tuning Energetic Levels in Nanocrystal Quantum Dots through Surface Manipulations. *Nano Lett.* **2008**, *8*, 678–684.

(102) Schlaf, R.; Parkinson, B. A.; Lee, P. A.; Nebesny, K. W.; Armstrong, N. R. HOMO/LUMO Alignment at PTCDA/ZnPc and PTCDA/ClInPc Heterointerfaces Determined by Combined UPS and XPS Measurements. *J. Phys. Chem. B* **1999**, *103*, 2984–2992.

(103) Yu, D.; Wang, C.; Guyot-Sionnest, P. N-Type Conducting CdSe Nanocrystal Solids. *Science* **2003**, *300*, 1277–1280.

(104) Eckhardt, H.; Shacklette, L. W.; Jen, K. Y.; Elsenbaumer, R. L. The Electronic and Electrochemical Properties of Poly (Phenylene Vinylenes) and Poly (Thienylene Vinylenes): An Experimental and Theoretical Study. *J. Chem. Phys.* **1989**, *91*, 1303–1315.

(105) Gao, J.; Li, Y.; Yu, G.; Heeger, A. J. Polymer Light-Emitting Electrochemical Cells with Frozen Junctions. *J. Appl. Phys.* **1999**, *86*, 4594–4599.

(106) Sun, H.; Li, Z.; Kong, L.; Wang, B.; Zhang, C.; Yuan, Q.; Huang, S.; Liu, Y.; Li, L. Enhancing the Stability of $CsPbBr_3$ Nanocrystals by Sequential Surface Adsorption of S^{2-} and Metal Ions. *Chem. Commun.* **2018**, *54*, 9345–9348.

(107) Kucur, E.; Riegler, J.; Urban, G. A.; Nann, T. Determination of Quantum Confinement in CdSe Nanocrystals by Cyclic Voltammetry. *J. Chem. Phys.* **2003**, *119*, 2333–2337.

(108) Kuçur, E.; Bücking, W.; Giernoth, R.; Nann, T. Determination of Defect States in Semiconductor Nanocrystals by Cyclic Voltammetry. *J. Phys. Chem. B* **2005**, *109*, 20355–20360.

(109) Kucur, E.; Riegler, J.; Urban, G. A.; Nann, T. Determination of Quantum Confinement in CdSe Nanocrystals by Cyclic Voltammetry. *J. Chem. Phys.* **2003**, *199*, 2333–2337.

(110) Shafiee, A.; Salleh, M. M.; Yahana, M. Determination of HOMO and LUMO of [6, 6]-Phenyl C61-Butyric Acid through Voltametry Characterization. *Sains Malaysiana* **2011**, *40*, 173–176.

(111) Haram, S. K.; Kshirsagar, A.; Gujarathi, Y. D.; Ingole, P. P.; Nene, O. A.;

Markad, G. B.; Nanavati, S. P. Quantum Confinement in CdTe Quantum Dots : Investigation through Cyclic Voltammetry Supported by Density Functional Theory (DFT). *J. Phys. Chem. C* **2011**, *115*, 6243–6249.

(112) Brédas, J. L.; Silbey, R.; Boudreaux, D. S.; Chance, R. R. Chain-Length Dependence of Electronic and Electrochemical Properties of Conjugated Systems: Polyacetylene, Polyphenylene, Polythiophene, and Polypyrrole. *J. Am. Chem. Soc.* **1983**, *105*, 6555–6559.

(113) Markad, G. B.; Battu, S.; Kapoor, S.; Haram, S. K. Interaction between Quantum Dots of CdTe and Reduced Graphene Oxide : Investigation through Cyclic Voltammetry and Spectroscopy. *J. Phys. Chem. C* **2013**, *117*, 20944–20950.

(114) Protesescu, L.; Yakunin, S.; Bodnarchuk, M. I.; Krieg, F.; Caputo, R.; Hendon, C. H.; Yang, R. X.; Walsh, A.; Kovalenko, M. V. Nanocrystals of Cesium Lead Halide Perovskites ($CsPbX_3$, X = Cl, Br, and I): Novel Optoelectronic Materials Showing Bright Emission with Wide Color Gamut. *Nano Lett.* **2015**, *15*, 3692–3696.

(115) Nedelcu, G.; Protesescu, L.; Yakunin, S.; Bodnarchuk, M. I.; Grotevent, M. J.; Kovalenko, M. V. Fast Anion-Exchange in Highly Luminescent Nanocrystals of Cesium Lead Halide Perovskites ($CsPbX_3$, X = Cl, Br, I). *Nano Lett.* **2015**, *15*, 5635–5640.

(116) Swarnkar, A.; Chulliyil, R.; Ravi, V. K.; Irfanullah, M.; Chowdhury, A.; Nag, A. Colloidal $CsPbBr_3$ Perovskite Nanocrystals: Luminescence beyond Traditional Quantum Dots. *Angew. Chemie - Int. Ed.* **2015**, *54*, 15424–15428.

(117) Samu, G. F.; Scheidt, R. A.; Kamat, P. V.; Janáky, C. Electrochemistry and Spectroelectrochemistry of Lead Halide Perovskite Films: Materials Science Aspects and Boundary Conditions. *Chem. Mater.* **2018**, *30*, 561–569.

CHAPTER II
MATERIALS AND METHODS

CHAPTER – II
MATERIALS AND METHODS

2.1. Materials

The essential chemicals required for the synthesis of quantum dots are lead acetate (Pb(OAc)$_2$, (Sigma-Aldrich), molecular bromine (Br$_2$, 99%, Rankem), oleic acid (OA, technical grade, Sigma-Aldrich), 1-octadecene (ODE, technical grade, Sigma-Aldrich), oleylamine (OAm, technical grade technical grade, Sigma-Aldrich), cesium carbonate (Cs$_2$CO$_3$, 99.9%, Sigma-Aldrich), dodecylamine (TCI, 97%), stearylamine (85%, TCI) and ocetylamine (99.9%, Sigma-Aldrich) were purchased. The required solvents such as toluene (99%, Finar), hexane (95%, Finar), acetonitrile (99.9%, Finar) ethanol (99%, Merck.) were purchased. Chemical such as tetrabutyl ammonium bromide, sodium perchlorate were purchased from Thomas Baker (99%) and Himedia (85-90%) respectively. Alumina powder required for the polishing of electrodes were purchased from TCI. All the solvents used for electrochemical studies were dried before use.

2.2. Physical Methods

2.2.1. Colloidal Synthetic Methods

To synthesize semiconductor NCs a various reliable synthetic procedure has been developed to obtain a high degree of optical properties such as tunable emission wavelength, high photoluminescence quantum yield (PLQY), narrow full width at half maximum and high defect tolerance as a function of control tunable shape and size. Generally, the synthetic route for the preparation of colloidal nanocrystals according to the state of reaction medium have been broadly classified into two categories *viz.* "top-down'' and "bottom-up'' synthetic strategies.[1,2] Top-down strategy involves the structuring and fragmentation of macroscopic solid either chemically or mechanically whereas bottom-up involves the reaction of molecules and ions in gas or liquid-phase both at room and high reaction temperatures.[3–5] But, due to the certain drawback of precursor and instrumentations vapour-phase of bottom-up and solid-phase of top-down synthetic approaches has been ruled out for the preparation of high degree phase purity of NCs. In contrast, colloidal semiconductor NCs synthesized from liquid-phase approach of bottom-up has been found to be an efficient route.[5–7]

Depending upon the type of reaction media, the liquid-phase approach has been further sub-divided into three main categories *viz.* (a) the organic-based approach,[8] (b) aqueous-based approach[9,10] and (c) the aqueous-organic based approach.[11] However, these methods under mild reaction temperature were unable to control the shape-size and phase purity of NCs. To tailor a well uniformity in morphology of NCs, a non-aqueous method has been proven to be the best strategic methodology in which it involves kinetic control over nucleation and growth processes by employing high boiling organic solvents and ligands.[12,13] The various non-aqueous methods that have been evolved during past few decades are hot-injection method, heat-up (non-injection) method and the ligand-assisted reprecipitation method. The brief introduction about these various non-aqueous methods have been discuss below.

2.2.1.1. Hot-Injection Method

The wet chemical colloidal synthesis offers a preparation of colloidal particles of a wide range of organize shape and size with high degree of controllability and reproducibility.[14,15] The colloidal synthetic methodology can be traced back to pioneering work of Faraday on gold nanoparticles/colloid.[16] Murray *et al*.[17] for the first time popularized hot-injection method through the synthesis of cadmium chalcogenide nanocrystal (*figure 2.1*). The method follows the swift injection of reactive precursors into the hot solution of remaining precursors, ligands and high boiling solvent which triggers monomer formation resulting into the rapid burst of nucleation.[15,18,19] In doing so, the solution temperature drops along with the rapid depletion of monomer concentration due to nuclei formation resulting into the termination of nucleation process. Subsequently, this allow to the growth of nanocrystal with no new formation of nuclei and this happens only if the reactions get quenched in ice-bath when it is still in size focusing regime.

The method is very much reliable for the preparation of monodisperse NCs and is based on concepts developed by LaMer and Dinegar *et. al*.[20] The method allows for synthesis of colloidal NCs with narrow size distribution by attaining the temporal separation between the nucleation and growth stages.
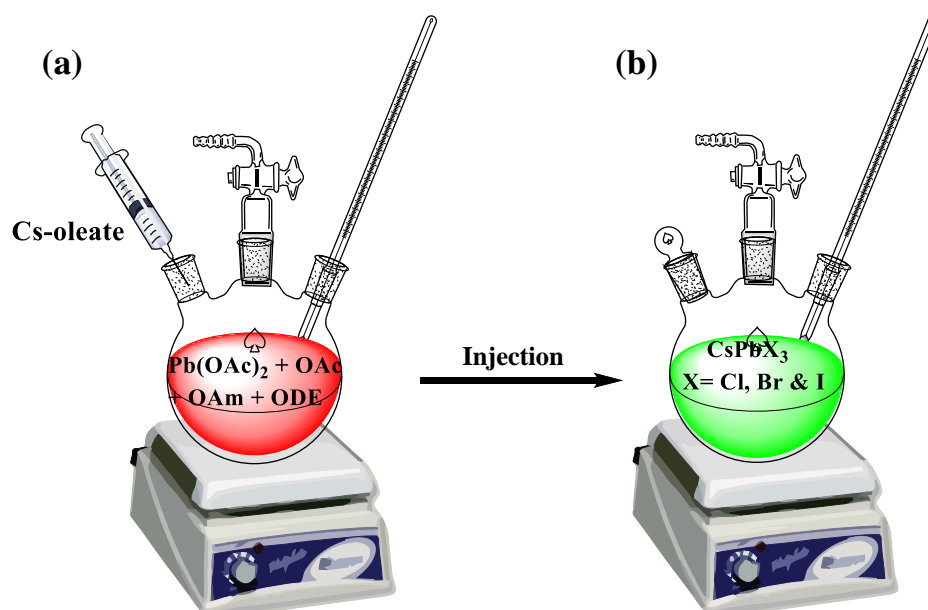
Figure 2.1: Representation of hot injection method (a) Before injection of precursor; (b) after injection of precursor.

The important factors that facilitate to control the size, size-distribution and shape of colloidal semiconductor NCs synthesized by hot-injection methods are (1) the injection temperature of the precursor, (2) the reactivity and concentration of precursor, (3) the reaction time, (4) the ratio of capping ligand to precursors, and (5) the effect of surfactant, solvent and pH, etc.[8] The hot-injection method is particularly effective because by varying the reaction temperature, concentration of ligands and reaction time it offers the formation of NCs of various tunable size. Furthermore, the method is very much feasible for the preparation of various type of NCs. Currently, the method is widely applicable for synthesizing all inorganic cesium lead halide perovskite NCs with high quality. In the year 2015, Protesescu *et. al.*[21] for the first-time synthesized lead-based perovskite NCs ($CsPbX_3$ where X = Cl, Br, and I) with a typical hot-injection method. It involves the rapid injection of Cs-oleate in an octadecene solution consisting of lead halide, oleylamine and oleic acid at high temperature typically in the range of 140-200 °C. The $CsPbX_3$ perovskite NCs synthesized through this method led to the development of NCs that cover the entire visible spectral region with narrow emission line width, high photoluminescence quantum yield as well as tunable band gap energy by varying the size and composition.[22–24] However, the method has certain drawback as it failed to scale-up thus hindering the larger scale in industrial productions.

2.2.1.2. Heat-Up Method

The heat-up based technique also known as the "non-injection method" is an alternative method for the preparation of colloidal nanocrystals. The method involves the participation of the precursors, stabilizing ligands and high boiling solvent into the reaction vessel followed by controllable heating of reaction mixture from room temperature to elevated temperature to induce the nucleation and growth of NCs provided that precursors should have negligible reactivity at low temperature and considerable reactivity at elevated temperature.[25–27] In order to obtain a high quality of nanocrystal a choice of precursors with suitable level of reactivity and heating rate is of great importance during reaction scheme.[28] In 2015, Van Embden *et. al.* [29] have reported the role of precursors, ligands and the reaction heating condition on the nucleation and growth of nanocrystals and hence the size distribution. In contrast to the hot-injection approach heat-up method have provided a synthesis of colloidal nanocrystals in large scale with batch-to-batch consistency and reproducibility.

2.2.1.3. Ligand-Assisted Reprecipitation Method

Ligand-assisted reprecipitation is a supersaturated recrystallisation process that has been conveniently employed for producing supersaturated solution without the protective atmospheric or heating condition. The process involved during the reaction is very simple. It consists of desired ions dissolving in an appropriate solvent until an equilibrium concentration is reached thereby attaining the reaction mixture to nonequilibrium state of supersaturation.[12] There are several approaches through which supersaturated state can be attained *viz.* by evaporating the solvent, by varying the reaction temperature, or by introducing the ion which has low solubility. Under such circumstances, when the reaction mixture attained the equilibrium state a spontaneous precipitation and crystallisation will observed. The method were found to be very much feasible for the preparation of organic NCs along with the synthesis of polymer dots.[30,31]

The precise control of reaction temperature is very much crucial due to the injection of precursor which tends to cause poor reproducibility as well as inhibiting large scale industrial production in case of perovskite NCs, thus to overcome such an issue an alternative low temperature synthesis method known as LARP is a promising strategy.[32] It involves the mixing of precursor salt solution dissolved in a good polar solvent such as dimethylsulfoxide (DMSO), dimethyl formamide (DMF) etc. and ligands into a non-

polar solvent such as toluene, hexane etc. under vigorous stirring condition at room temperature (*figure 2.2*).
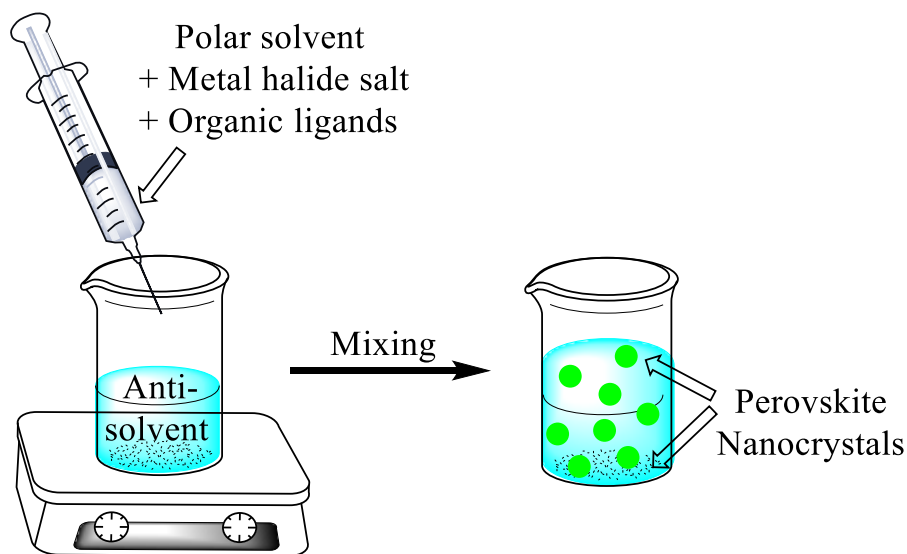
Figure 2.2: Representation of LARP synthetic approach.

The mixture of these solvent brings rapid supersaturation, which generate the nucleation and growth of perovskite NCs. In general, the precursor salts involved in LARP approaches are of MX_2 (where M represents metal such as Pb, Sn, etc.), CsX, MAX and FAX type (where MA and FA represent methylammonium and formamidinium respectively) X represents halide such as Cl, Br and I). The method is very much practicable for the scale-up production of metal halide perovskite NCs.[33–35] For the first time Papavassiliou *et. al.*[36] were able to synthesize hybrid organic-inorganic lead halide based perovskite NCs by dissolving the mixture of $MAPbX_3$, $(MA)(CH_3C_6H_4CH_2NH_3)_2Pb_2X_7$ or $(MA)(C_4H_9NH_3)_2Pb_2X_7$ (where X = Cl, Br, I) salts in DMF thereby further mixing the solution in toluene. In the year 2015, for the first time Zhang *et al.*[37] applying LARP method synthesize organic-inorganic $MAPbBr_3$ NCs by mixing the solution $PbBr_2$, MABr salts in alkyl amine, carboxylic acid and DMF with toluene at room temperature under vigorous stirring condition to form colloidal NCs. For gram scale production of $CsPbBr_3$ QDs, Wei *et. al.*[32] has developed homogenous reaction process at room temperature under ambient condition by dissolving all the precursor such as Pb^{+2}, Cs^+ and Br^- in non-polar solvents (e.g., hexane, toluene, dichloromethane, chloroform etc.). In addition, long-chain carboxylate acid

such as butyric acid, octanoic acid or oleyl amine, hexanoic acid plays an important role for synthesizing homogenous reaction mixture at room temperature.

Furthermore, the method is very much suitable for preparing lead-free and fully inorganic perovskite NCs. In the year 2017, Li *et. al.*[38] synthesizes cesium bismuth halide ($Cs_3Bi_2X_9$) perovskite NCs by mixing solution of CsX and BiX_3 precursor in a polar solvent such as DMSO into 2-propanol as a non-polar solvent. Though the method has potential to scale up the production of nanocrystal but to have precise control over size and morphology is very much crucial, which can be instead easily carried out via the hot-injection method.

2.2.2. Analytical Methods

The analysis of the synthesized materials was characterised with the help of various analytical techniques. The working principles that have been involved in the different techniques have been summarised below;

2.2.2.1. Spectrofluorometer-PL (Photoluminescence)

PL spectroscopy is a widely used analytical characterisation technique which is based on study of fluorescence emission characteristics, quantum yield of materials and their correlation with the concentration and internal electronic structure of the material. It is a simple, contactless and non-destructive technique for characterization of fluorescent quantum dots and dyes.[39–41]

Generally, a high intensity light source is directed onto the sample which absorbs photons resulting in excitation of electrons from a lower energy state (valence band/ HOMO) to higher energy state (conduction band/LUMO). After this initial photo-excitation process the excited electrons revert back to the ground state level dissipating the excess amount of energy (Fluorescence). The intensity, the line width and position of the emitted light provide insights about the electronic as well as physical properties of the material such as band gap, size of the colloidal nanocrystals, size distribution, surface defects etc.

During the photo-excitation process, the electrons of the material get excited within the permissible excited state, meaning that an electron goes from ground singlet state to an excited singlet state, by absorbing photon of equal or greater energy. Within the femtosecond (typically 10^{-8} sec. after excitation) the material undergoes transition from an upper electronically excited state to the equilibrium state by releasing an excess energy which may involve the emission of light (a radiative process) or may not (a non-radiative process) as shown in figure 2.3.
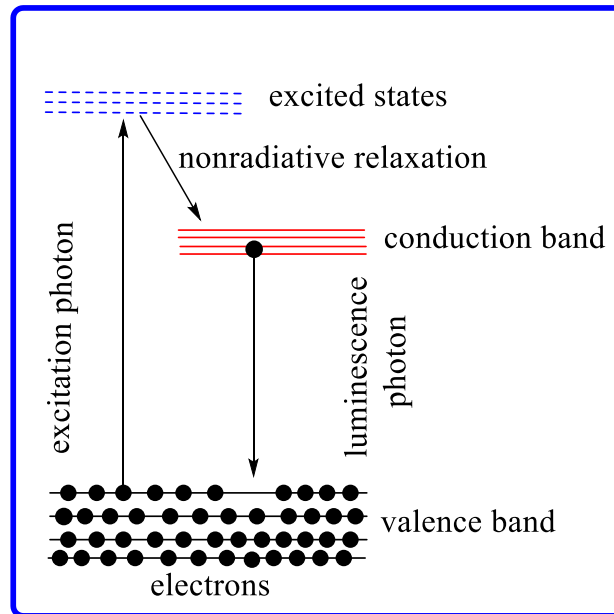
Figure 2.3: Principle of photoluminescence spectroscopy (PL).

The difference between the excitation wavelength and the emission wavelength is known as Stoke's shift and is given by the following equation as shown below;

$$\text{Stoke's shift (cm}^{-1}) = 10^7 \left(\frac{1}{\lambda_{ex}} - \frac{1}{\lambda_{em}}\right) \quad \text{............. (i)}$$

The PL spectrophotometer gives only characteristic properties of the low-lying energy level of the system. With regards to the luminescence semiconductor system, generally the radiative transition takes place from the conduction band to valence band and the energy difference between these band is known as the band gap. The examination of PL spectrum leads to the identification of specific defect or impurities present in the semiconductor system as during the radiative transition in semiconductor it may also involve localized defects or impurity levels. Furthermore, the magnitude of PL spectrum allows us to determine their concentration. Thus, according to the analytical

data of PL, we can conclude the type of band gap, impurities, defect levels and crystalline quality of semiconducting material. From the peak intensity of PL spectra, we can reveal the composition of materials and further with the help of PL, we can investigate the internal interface of hetero-structure which cannot be determine with that of general physical or electronic measurements.

PL is quite different from absorption spectrum as it is an embodiment of radiative recombination and involve the transition of photon from excited state to the ground state whereas absorption spectrum involves the excitation of photon from ground state to excited state. The time period between the emission and absorption is very small. An excitation spectrum is the relative efficiency of different wavelengths of exciting radiation in causing fluorescence which looks very much similar to an absorption spectrum and is independent of wavelength at which fluorescence is measured.

The fluorescence quantum yield (QY) is measured by taking the ratio of the number of photons emitted to the number photons absorbed and is expressed by the following equation;

$$QY = \frac{photons_{emitted}}{photons_{absorbed}} \qquad \text{............. (ii)}$$

The relative quantum yield (QY$_R$) of an unknown sample is determined by comparing the known quantum yield (QY$_S$) of standard dye with that of the integrated photoluminescence of the sample using the equation;

$$QY_S = QY_R \frac{I_S \text{ X } A_R \text{ X } n_S^2}{I_R \text{ X } A_S \text{ X } n_R^2} \qquad \text{.......... (iii)}$$

Where I is the integrated PL intensity, A is the absorbance, and n is the refractive index.

Equation (iii) may be written as:

$$QY_S = QY_R \text{ X } \frac{\frac{I_S}{A_S}}{\frac{I_R}{A_R}} \text{ X } \frac{n_S^2}{n_R^2} \qquad \text{......... (iv)}$$

2.2.2.1.1. Experimental Set-Up

A spectrofluorometer is an analytical instrument used to determine and record both the emission and excitation of fluorescence material. The instrument is capable to monitor the variation of signal with time, temperature, concentration and other variable accessories. The flow chart diagram of fluorescence spectrometer is show in figure 2.4.

The experimental set up of spectrofluorometer consist of illuminator source, monochromators, gratings, slits, shutters, sample compartment, detector and computer control. For this project, unless otherwise stated, we have used HORIBA scientific spectrophotometer (Model: PTI-QM 510) and the data were processed using FelixGX 4.9 version software. The dispersed sample in hexane solvent were excited at 400 nm using a xenon lamp source coupled to a monochromator. For all the experiments the excitation slits were set to 1.92 nm for entrance and 1.92 for the exit. For emission, slit were set to 0.96 nm for entrance and 0.96 for the exit. The figure 2.4. shows the instrument installed in our laboratory.
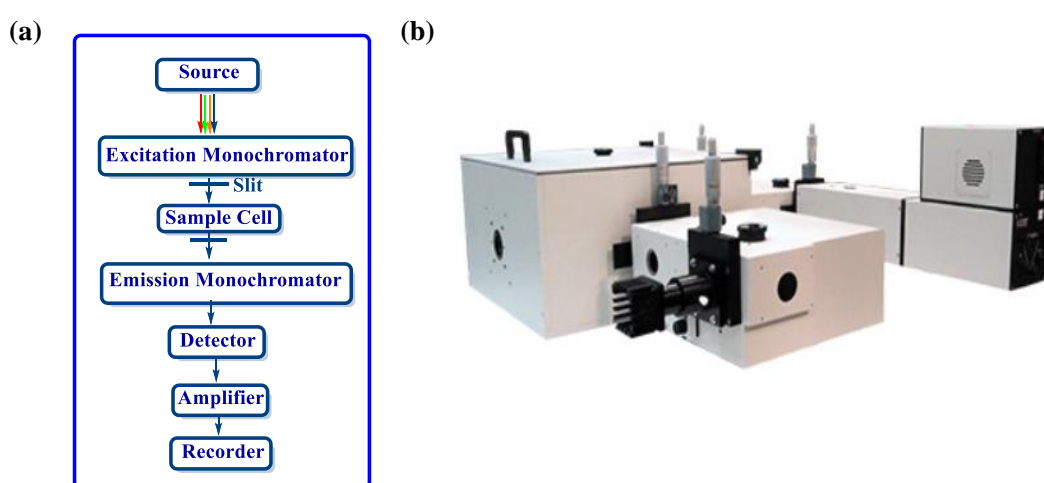
Figure 2.4: (a) Flow chart diagram of fluorescence spectrometer and (b) HORIBA scientific spectrophotometer.

2.2.2.2. Powder X-ray Diffraction (P-XRD)

Powder X-ray diffraction (XRD) is one of the most prevailing nondestructive analytical technique primarily employed for phase identification of a crystalline materials. It provides information on crystal structure, phase, preferred crystal alignment and various other properties such as grain size, crystallinity, crystal defect and strain.[42,43] The sample should be finely grounded and homogenized in case of solid sample. For colloids, the sample is prepared on a glass slide /sample holder by drop-casting a concentrated solution of the colloidal materials.

Historically, in 1912 Max von Laue and his co-worker [44] discovered that the crystalline materials behave as a three-dimensional diffraction grating for X-ray since the

wavelength of a X-ray beam is comparable to the spacing of planes in a crystal lattice. X-rays produced in a cathode tube is filtered to generate monochromatic radiation which is subsequently directed towards the sample. The diffraction patter is the result of the constructive interference of monochromatic X-rays as predicted by Bragg's equation:

$$n\lambda = 2d_{hkl} \sin \theta \ldots\ldots\ldots\ldots \text{(i)}$$

Where, n is an integer, λ is the wavelength of the incident X-rays beams, d_{hkl} is the interplanar spacing between the neighbouring lattice plane with Miller indices *hkl* and θ is the half angle between the incident and diffracted beams. The interplanar distance, d_{hkl} with the precise Miller indices for cubic and orthorhombic systems are determined using the following equations:

Cubic:

$$\frac{1}{d_{hkl}^2} = \frac{h^2 + k^2 + l^2}{a^2} \qquad \ldots\ldots\ldots\ldots\ldots \text{(ii)}$$

Orthorhombic:

$$\frac{1}{d_{hkl}^2} = \frac{h^2}{a^2} + \frac{k^2}{b^2} + \frac{l^2}{c^2} \qquad \ldots\ldots\ldots\ldots \text{(iii)}$$

Where a, b, c are unit cell parameters.

The law corelates the wavelength of electromagnetic radiation to the diffraction angle, 2θ and the lattice spacing d_{hkl} in a crystalline material. Due to the random positioning of the powder materials all the possible diffraction directions of the lattice will be observed while scanning the sample at the range of 2θ. Consequently, a family of planes generates a diffraction peak only at a specific angle, 2θ. Furthermore, the change of diffraction peaks to d-spacing permits the identification of the materials as each material has its own set of unique-d-spacings.

2.2.2.2.1. Experimental Set-Up

The instrument installed in our laboratory is PANalytical X' Pert Pro diffractometer using Cu Kα (λ = 1.54 Å) as the incident radiation (30 kV and 15 mA). All the experiment was performed with a scan rate of 0.02 $\degree$s^{-1}. Data collection and analysis

was performed with Data Collector of version 3.0 C (3.0.3.188) and High Score Plus of version 3.0C (3.0.3) respectively. X-ray diffractometer comprises of three basic elements viz. an X-ray tube, a sample holder and an X-ray detector. The experimentally obtained XRD signal were compared with the signal obtained after simulation or from different sources so that the phase and purity of the materials can be determined. The other techniques that can complement or cross-validate the results obtained in PXRD are XAFS, HR-TEM, SAXS, etc.[45]

Figure 2.5: Panalytical X'Pert Pro P-XRD instrument.

2.2.2.3. Fourier Transform Infrared Spectroscopy (FT-IR)

Infrared spectroscopy is an important technique used to determine the vibrational frequency of functional groups associated with the molecules with characteristic infrared absorption band which corresponds to the fundamental vibration of the functional group.[46–48] It is an easy technique to categorize the presence of certain functional groups in a molecule. Analysis through infrared spectroscopy is primarily based on the vibration of chemical bonds in the mid infrared region of electromagnetic spectrum: ~ 4000 cm^{-1} to ~ 200 cm^{-1}. It is further divided into two main region- the region from 200-1600 cm^{-1} is known as finger print region and from 1600-4000 cm^{-1} is known as functional group region. The vibrational spectra of the molecule is determined by following the Hooke's law and is given by the following equation;[49]

$$\bar{\upsilon} = \frac{1}{2\pi c} \sqrt{\frac{k}{\mu}} \text{ cm}^{-1} \quad \ldots\ldots\ldots\ldots\text{(i)}$$

Where $\bar{\upsilon}$ is a wave number in cm^{-1}, c is the speed of light in cm sec^{-1}, k is the force constant in dyne cm^{-1} and μ is the reduced mass of atoms.

When a molecule is irradiated with a beam of infrared radiation it will absorb those radiation only which is equal to or greater than the molecular vibrational frequencies. The absorbed frequencies of infrared radiation are measured by an infrared spectrometer. The signal obtained by plotting the absorbed energy vs frequency is known as infrared spectrum of the material. Each material has its own vibration, yielding different infrared spectra as a result of which identification of material become possible. Furthermore, it is possible to determine the type of various functional group present in the materials through frequencies of the absorption.

For a linear molecule possessing N atoms, there are 3N-5 normal modes or fundamental vibration motions of the molecule are possible and 3N-6 for non-linear molecules. A normal mode of vibration is infrared active if there is a change in the dipole moment of the molecules during vibration. In the mid-infrared region (4000-1000 cm^{-1}) two commonly known vibrational modes of the molecules are observed *viz.* stretching and bending. In stretching mode, vibration takes place along the bond resulting in the change in bond-length whereas in the bending mode, vibration lead to the change in bond angle (δ-in plane and π-out of the plane). Furthermore, stretching mode is sub-divided into two main types - symmetric and ant-symmetric stretching as demonstrated in figure 2.6.

(a)　　　　　　　　　　　　　**(b)**

symmetric stretching　　　　　anti-symmetric stretching
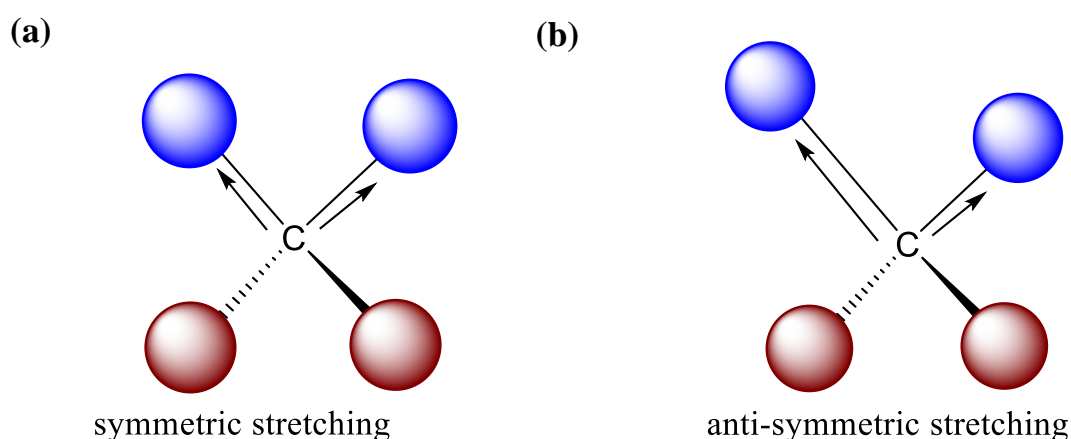
Figure 2.6: Representation of different mode of stretching vibration (a) symmetric stretching and (b) anti-symmetric stretching.

In symmetric stretching, two bonds will elongate and contract simultaneously at the same time and require lower energy. But in case of anti-symmetric stretching mode, one of the two atom moves towards the central atom while another atom moves away from central atom and thus require higher energy.

Further, bending mode of vibration are also called deformation vibration and it is classified into two types:

(a) In-plane Bending vibrations, and

(b) Out of plane Bending vibrations

(a) In-plane bending- This type of vibration lead to the change in bond angle and takes place within the same plane. It is of two types.

- **Scissoring** in which bond angle decreases due to the movement of two atoms simultaneously towards or away from the central atom.
- **Rocking** in which two bond moves in clockwise or anticlockwise direction within the same plane maintaining bond angle.

(a) **(b)**

scissoring   rocking
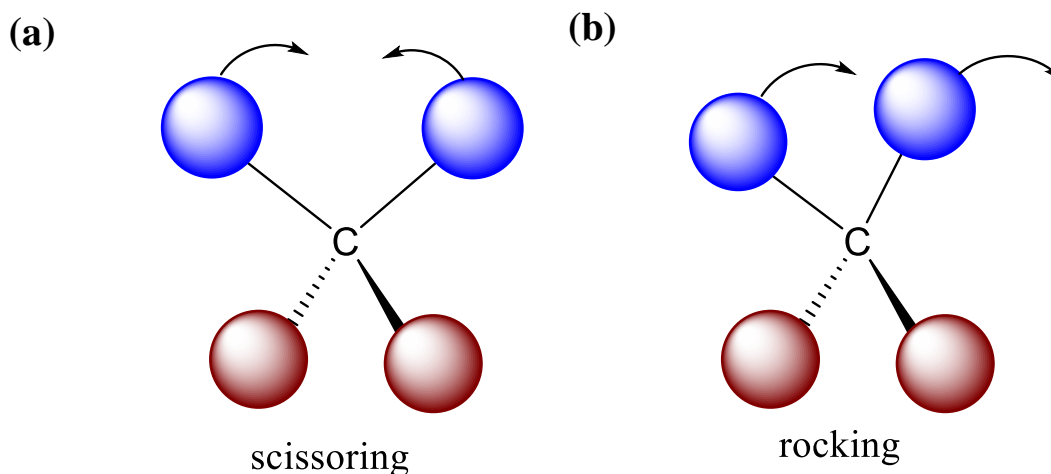
Figure 2.7: Different mode of in-plane bending (a) scissoring and (b) rocking.

(b) Out of plane bending- This type of bending vibration takes place out of the plane of molecule. It is of two types.

- **Wagging** in which two atom moves in V direction to one side of the plane.
- **Twisting** in which one atom is moving above the plane and the other is below the plane.
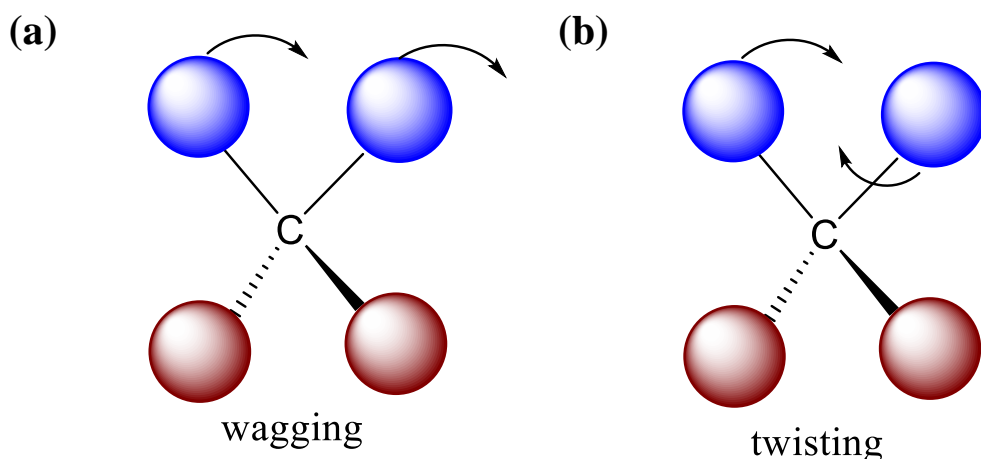
Figure 2.8: Different mode of out of a plane bending (a) wagging and (b) twisting.

2.2.2.3.1. Experimental Set-Up

The instrument installed in our laboratory is Bruker ALPHA E, 200396 spectrophotometers as shown in figure 2.9.(a). The spectra were recorded between the range of 600-4000 cm^{-1} with a resolution of 4 cm^{-1}. The instrument consists of following basic components such as light source, monochromator, sample holder and the detector as shown systematically in figure 2.9.(b).

Both the liquid and solid state of sample can be studied in our set-up. Basically, the light source used in this instrument is Globar filament or Nernst filament consisting of red or white light which are used to heat for at least half an hour before analysis. The produced light is incident over the sample on the silver layered mirror and will pass toward the monochromator for generating equivalent energy of light with respect to the experimental sample. Thin film of sample is introduced over ATR crystal surface and then the detector will detect by sensing the heating effect. The detected signal is digitised and sent to the computer where the Fourier transformation takes place to get the IR spectrum.

(a)   **(b)**
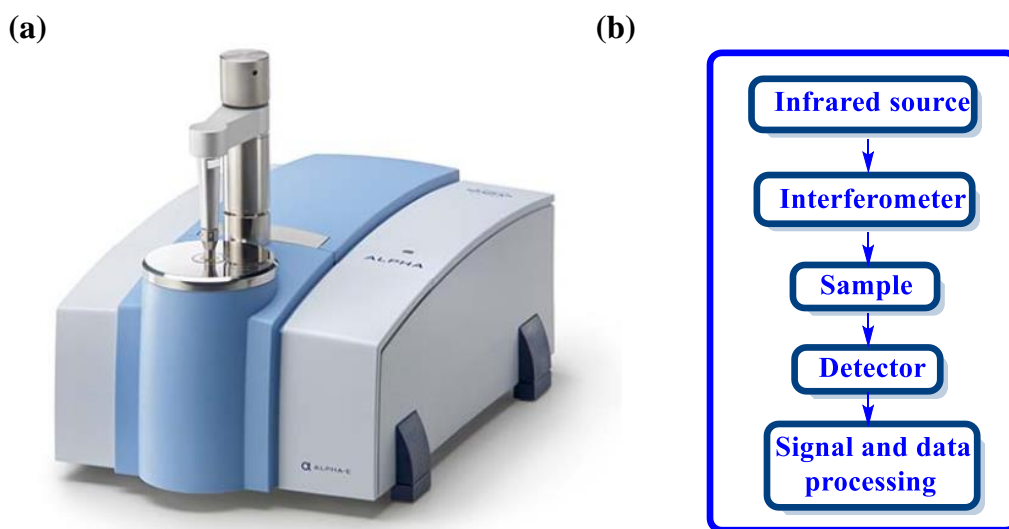
Figure 2.9: (a) Bruker Alpha FT-IR Spectrophotometer, and (b) Flowchart diagram of FT-IR spectrophotometer.

2.2.2.4.   Ultraviolet-Visible Spectroscopy

UV-Visible spectroscopy is employed to investigate the type of electronic transitions present in the molecules as they absorb light in the UV and visible regions of the electromagnetic spectrum. It is used for analysing solids, liquids and gases by irradiating electromagnetic radiations in the far and near ultra-violet (UV), visible (Vis) and near-infrared (NIR) region of the electromagnetic spectrum. The values of the electromagnetic radiation wavelength for UV, Vis and NIR radiation are defined as follows:[50,51]

- UV radiation – 300 - 400 nm
- Vis. radiation – 400 - 765 nm
- NIR radiation – 765 - 3200 nm

Basically, spectroscopy is related to the interaction of electromagnetic radiations with the matter. The absorption of UV or Vis radiation by the matter results in an increase in the energy content of the atoms or molecules resulting in the transition among electronic energy level hence it is also often known as electronic spectroscopy.

UV-Visible spectroscopy is based upon the principle of Beer-Lambert Law.[50] It corelates a linear relationship between the absorbance and the concentration of an absorbing species. It states that when a beam of monochromatic light is passed through a uniform solution of an absorbing substance, the rate of decrease of intensity of

radiation with thickness of the absorbing solution is proportional to the incident radiation as well as the concentration of the solution. It is expressed as;

$$A = \log (I_0/I) = \epsilon c l \ \ldots\ldots\ldots\ldots (i)$$

Where, A is the absorbance, I_0 intensity of the incident light upon sample cell, I is the intensity of transmitted light, c is the molar concentration of the solute, l is the path length of the sample cell in cm and ϵ is the molar absorptivity or the molar extinction coefficient of the substance.

Generally, the transition of electron takes place from the highest occupied molecular orbital (HOMO) to the lowest unoccupied molecular orbital (LUMO) by absorbing photon of certain wavelength and energy which is equal to the energy required for electron to get promoted to higher energy state. The resulting species is said to be in an excited state. The theory revolving around this concept is that the wavelength at which absorbance take place is equal to the energy difference between the HOMO and LUMO. The energy of the transmitted light from the material afterwards is measured with the help of photo detector and produces a distinct spectrum.

A various type of electronic transition will take place during interaction of electromagnetic radiation with a molecule. Basically, there are three principal types of molecular orbital viz.- sigma (σ) orbitals, pi (π) orbitals and filled but nonbonding orbitals (n) in which the molecule will contains valence electron in the ground state. In the electronic transition, the excitation of electron will take place from one of the three ground state (σ, π or n) to one of the two excited state (σ*, or π*). This excitation of electron will result into six possible transitions – σ-σ*; σ-π*; π-π*; π-σ*; n-π*; n-σ*. The said electronic transitions is clearly depicted in figure 2.10.
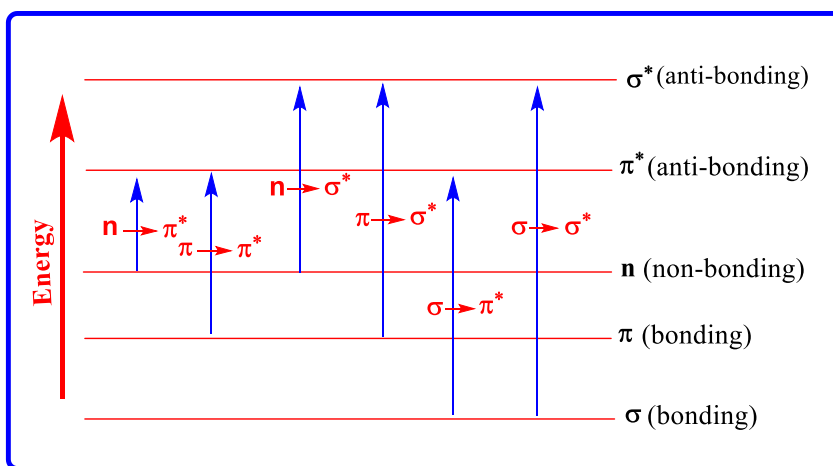
Figure 2.10: Electronic transition in UV-visible spectroscopy.

From the figure 2.10. we can see that in each transitions the electron is excited from the lower energy state (ground state) to the higher energy state (excited state) and for each transition a definite amount of energy is required. Furthermore, larger the gap between the energy levels greater the amount of energy is required to promote an electron to the next higher energy levels. As a result, an electromagnetic radiation of higher frequency is required thereby absorbing in shorter wavelength. An important mode of electronic transitions is described below;

- **σ-σ*** - The transition of an electron from a bonding sigma orbital to an anti-bonding sigma orbital is known as σ to σ* transition. This type of transition requires a larger amount of energy as the σ bond is very strong. Thus, this type of transition includes shorter wavelength (< 150 nm) and usually fall outside the range of UV-visible spectrophotometer (200-800 nm).

- **π-π*** - The transition of an electron from a bonding pi orbital to an anti-bonding pi orbital is known as π-π* transition. Usually, these types of transition are seen in compounds having one or more unsaturated group such as alkene, carbonyl, nitrile, nitro etc. This type of transition requires lesser amount of energy as compared to n to σ* transition.

- **n-σ*** - The transition of an electron from a non-bonding orbital to an anti-bonding sigma orbital is designated as n-σ* transition. This type of transition is shown by molecules having lone pairs of electrons such as amine, saturated alcohol, halides etc. It requires less amount of energy than σ-σ* transition.

- **n-π*** - The transition of an electron from a non-bonding orbital to an anti-bonding orbital is known as n to π* transition. Usually, the carbonyl compound shows n to π* transition along with π-π* transition. The transition from n to π* appears at longer wavelength as this type of transition requires least amount of energy.

Colloidal quantum dots also absorb UV or Visible or near infrared light, resulting in the generation of coulombically connected electron-hole pair known as excitons. The absorption band width, position and pattern reflect the electronic structure of the material such as optical band gap.

2.2.2.4.1. Experimental Set-Up

The instrument used in our lab is Perkin Elmer Lambda 25 spectrophotometer as shown in figure 2.11. (a). The data were collected using Lamda25 software. All the experiment were conducted with a scan rate of 480 nm min^{-1}. It consists of light source (UV and vis.), monochromator (wavelength selector), sample holder, detector and recorder. Figure 2.11. (b) shows a systematic set up of UV-visible spectrophotometer.
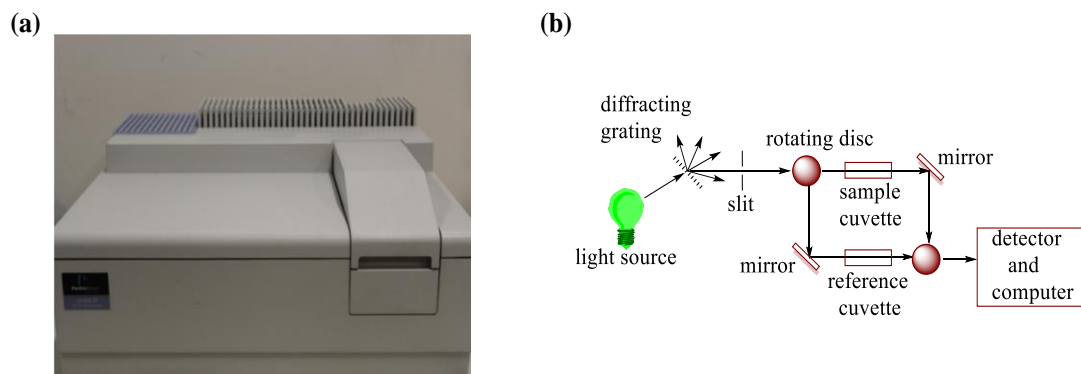
Figure 2.11 (a) Perkin Elmer Lambda25 UV-visible spectrophotometer. (b) Systematic diagram of UV-visible spectroscopy.

UV-vis spectra are measured by preparing a very dilute solution of sample in a suitable solvent. The solvent should be inert to the sample. Some of the commonly used solvents are hexane, ethanol, water etc. Before investigation of the experiment background correction is necessary by placing the suitable solvent for the experiment in a transparent cell of 1 cm path length of quartz cuvette. After completing the background correction both the sample solution and the previous reference solution is again placed in a sample holder by setting the absorption wavelength from 800-200 nm. The various source of radiation is used such as tungsten filament, a deuterium arc lamp which is continuous over the ultraviolet region, and more recently light emitting diodes (LED) and xenon arc lamp is used for the visible wavelengths. Photodiodes are used with the monochromators in order to filter the light so that only a light of single wavelength is detected by detector to record spectra.

2.2.2.5. Thermogravimetric Analyser (TGA)

It is simple analytical technique used to investigates the change in the mass of a substance as a function of time or temperature in a controlled atmosphere.[52,53] The variation in weight is recorded when the sample is typically subjected to heating or

cooling under controlled environmental programmed condition. When the change in weight of a substance is recorded with respect to time than the said condition is termed as "isothermal mode". During the scanning mode, the weight loss is recorded as a function of temperature. The choice of temperature is programmed according to the type of information required about the substances. Furthermore, the type of atmosphere used in the TGA experiments plays an important role as it can be reactive or inert that flows over the sample in order to prevent oxidation or other uncertain reactions and exit through an exhaust. Change in the atmospheric condition can be made during experiment.

The principle involved in the TGA is that the loss of weight mass can be investigated under the controlled atmospheric condition. Thus, it is mainly employed to understand the thermal events such as decomposition, oxidation-reduction, absorption, adsorption, desorption and sublimation. Beside this, it can be used for the determination of volatile or gaseous lost product of substances such as nanomaterials, polymer, films, fibers, paints and coatings. Furthermore, it can perform kinetics of chemical reactions under various experimental conditions.[54]

TGA comprises of microbalance, programmable temperature, controller, sample holder, furnace and recorder. The microbalance is connected to the sensor so that a small deviation of an order of 10^{-6} g from the null point can be determined. Measurements were done by loading a sample in a pan composed of platinum or aluminium or ceramics and get suspended towards the furnace where a highly monitored heating environment is maintained. A plot of weight loss vs temperature is referred to as the thermogravimetric curve (TGA curve) or derivative thermogravimetric curve (DTG). At first the change in mass/weight vs time or temperature is plotted. Secondly, the plot is performed with respect to the rate of change in mass/weight vs time or temperature.[55] The TGA curves helps to determine the transparency of analytical sample along with their mode of transformation with respect to the specified range of temperature. As many weight loss curves look very similar, so a derivative weight loss curve can be implemented in order to find out the point at which the weight loss is most apparent.

2.2.2.5.1. Experimental Set-Up

The instrument used for the analysis of sample in our lab is TA Instrument's Q50 Analyser (*figure 2.12)* for thermogravimetry measurements.

Figure 2.12: TA Instrument's Q50 Analyser.

During the investigations, there is a controlled mechanism to regulate the system to heat at the rate of 20 °C min^{-1} up to 800 °C under inert atmospheric condition maintaining the flow of N$_2$ gas at the rate of 60 mL min^{-1} inside the heating furnace and 40 mL min^{-1} inside the balance chamber. Two platinum pans were supported by a precision balance, among them one of the pans were used as a reference and other one to hold the sample. Finally, the recorded data were plotted and obtain in the form of both TG and DTG curve.

2.2.2.6. Cyclic Voltammetry (CV)

Cyclic voltammetry is a very powerful tool and has become a significant and widely used electroanalytical technique in many fields of chemistry. It is generally used for the investigation and measurement of redox processes involving electron transfer reaction of an electro active molecular species which are soluble in an appropriate solvents.[56,57] It can provide important information about the reaction between the ions and surface atoms of the electrodes for understanding the reaction intermediate that brings stability to the reaction products.[58] Furthermore, it provides a qualitative information about the electrode reaction mechanism, charge transfer reaction between the electrolyte ions and electron from the electrode surface, determination of energy of HOMO-LUMO levels, to evaluate the ligand effects over the oxidation/reduction potential of the central metal

ion in complexes and multi nuclear cluster and compound stability under experimental conditions.[59,60] As similar to other organic or inorganic molecules, semiconductor NCs having unique intriguing tunable optoelectronic properties depend upon the size, so-called quantum size effect and the composition. They have attracted significant interest due to their influential effect towards the band edge position *viz.* the valence band edge (h_1) and the conduction band edge (e_1) which can be further attributed to the anodic and cathodic peak respectively in the cyclic voltammogram.
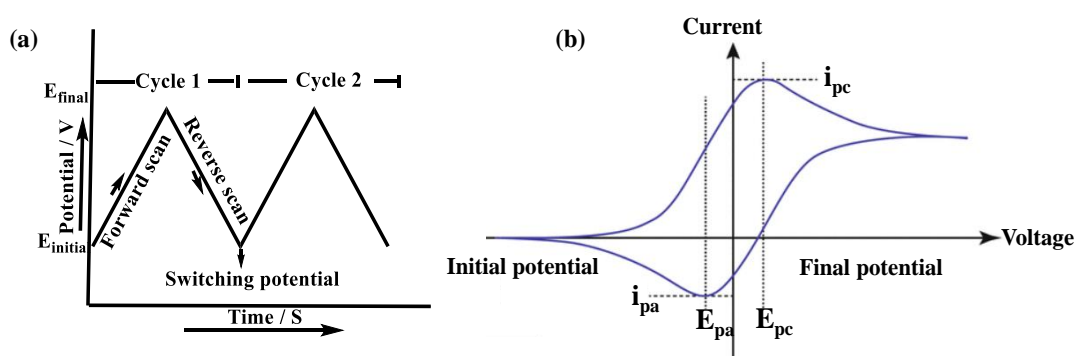
Figure 2.13: (a) Cyclic voltammetry potential triangular waveform; (b) representation of cyclic voltammogram.

It has been routinely employed since decades due to its mild experimental procedure at room temperature and at ambient atmospheric pressure [22,61–64]. Thus, it is a very useful electroanalytical technique to understand the redox reaction which plays a very decisive role for charge storage mechanism in the study of super capacitor.[65] It is potentiodynamic electrochemical measurements that involves the linear and cyclic variation of the applied potential between the working electrode and the reference electrode within a potential window in both the forward and reverse direction. The produced currents were measured between the working and the counter electrode. The potential that is applied across this electrode can be consider as excitation signal and is a linear potential scan with a triangular wave form as shown in figure 2.13.(a). A cyclic voltammogram (*figure 2.13. (b)*) is a curve obtained by measuring the current at the working electrode during the potential scan and generally two convention were commonly employed to represent CV data *viz.* the US convention and the IUPAC convention as depicted in figure 2.14.[57]
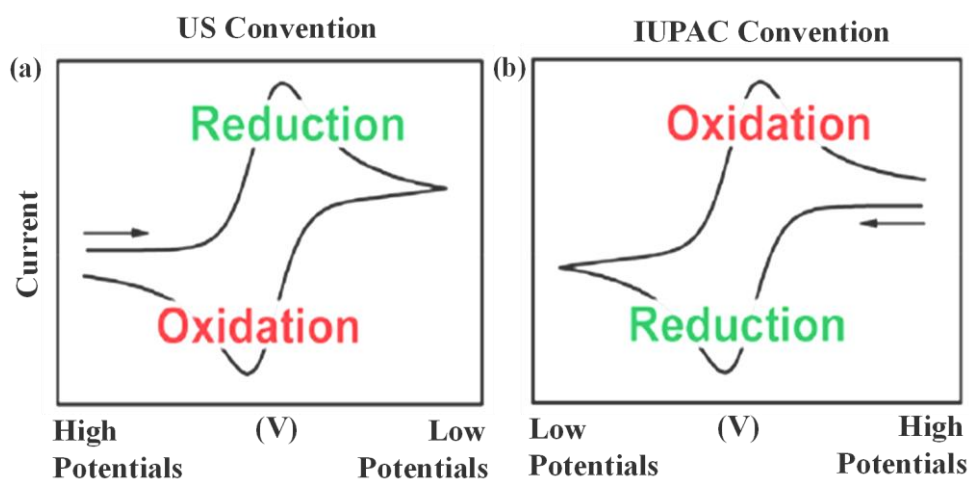
Figure 2.14: Representation of cyclic voltammogram (a) US convention, and (b) IUPAC convention.

For reversible redox reaction as shown below, the equilibrium is described by Nernst equation;

$$A^+ + e^{-1} \leftrightarrows B \qquad \ldots\ldots\ldots\ldots \text{(i)}$$

It relates the potential of an electrochemical cell (E) to the standard potential of an electroactive species (E^0) and the relative activities of the oxidised and reduced analyte at equilibrium.

$$E = E^0 + \frac{RT}{nF} \ln \frac{Oxi}{Red} \qquad \ldots\ldots\ldots\ldots \text{(ii)}$$

$$\text{Or, } E = E^0 + \frac{RT}{nF} 2.303 \log_{10} \frac{Oxi}{Red} \qquad \ldots\ldots\ldots. \text{(iii)}$$

Where, F is Faraday's constant, R is the universal gas constant, T is the temperature, n is the number of electrons.

The significant parameters of a cyclic voltammogram are the magnitude of peak current (i_{pc} & i_{pa}) and peak potential (E_{pc} & E_{pa}) of cathodic and anodic peaks respectively. These parameters are labelled in the figure 2.13.(b). In an electrochemically reversible couple system both the oxidised and reduced species will rapidly transfer an electron with the working electrode. The half wave potential ($E_{1/2}$) between the two peaks i.e. anodic peak potential (E_{pa}) and cathodic peak potential (E_{pc}) for a reversible couple in the voltammogram is given by;

$$E_{1/2} = \frac{E_{pc} + E_{pa}}{2} \qquad \ldots\ldots\ldots\ldots\ldots \text{(iv)}$$

Furthermore, the separation between the two peaks of the voltammogram is given by;

$$\Delta E_p = E_{pa} - E_{pc} \quad \dots\dots\dots\dots \text{ (v)}$$

If the system is electrochemically reversible, the peak-to-peak separation i.e. the difference between the anodic peak potential and cathodic peak potentials, ΔE_p is 57 mV at room temperature and the width at half max on the forward scan of the peak is 59 mV.[57]

The number of electrons (n) transferred during the reversible couple can be determined by the following equation;

$$\Delta E_p = E_{pa} - E_{pc} \cong \frac{0.059}{n} \quad \dots\dots\dots\dots \text{ (vi)}$$

For example, in the case of one electron reduction process of $[Fe^{III} (CN)_6]^{3-}$ to $[Fe^{II} (CN)_6]^{4-}$ the peak-to-peak separation was found to 0.059 V. The peak current, i_p for a reversible system is given by the equation known as Randles-Sevcik equation and this equation helps to describe that how the peak current increase linearly with the square root of the scan rate.[57,58] Furthermore, the equation helps to determine the diffusion coefficient of the analyte.

$$i_p = 0.446 n F A C^0 \left(\frac{n F v D_o}{RT} \right)^{\frac{1}{2}} \quad \dots\dots\dots\dots \text{ (vii)}$$

Where, A is the electrode surface area in cm^2, v is the scan rate in V s^{-1}, F is Faraday's constant, D_o is the diffusion coefficient of oxidised analyte in cm^2 s^{-1}, C^0 is the bulk concentration of the analyte in mol cm^{-3}, R is the universal gas constant and T is the temperature. The values of i_{pa} and i_{pc} should be identical for a reversible couple system i.e.;

$$\frac{i_{pa}}{i_{pc}} = 1 \quad \dots\dots\dots\dots \text{ (viii)}$$

2.2.2.6.1. Experimental Set-Up

The electrochemical investigation of the analyte was carried out on a solution using a BASI INC, USA/EPSILON electrochemistry workstation. Basically, it is a three

electrodes system consisting of a working electrode (e.g., platinum electrode, glassy carbon electrode), a counter or auxiliary electrode (e.g., platinum wire) and a reference electrode (e.g., silver/silver chloride, calomel electrode). Herein we have used Pt disc electrode, 1.6 mm diameter as a working electrode, Pt wire as a counter electrode and Ag/AgCl as a reference electrode. All the experiment were carried out with a scan rate of 50 mVs^{-1}.

- **Working electrode (WE)** – It is the electrode where the electrochemical event of interest is takes place. It is composed of redox inert material in the potential range of interest. It serves as surfaces on which the electrochemical event takes place thus, it is imperative to have extremely clean well define surface area.
- **Counter electrode (CE)** – It is the electrode which complete the electrical circuit during electrochemical investigation by passing the current from the external circuit through the cell as it serves as a source or sink for electrons. It has greater surface area than the working electrode.
- **Reference electrode (RE**) – It is the electrode used to determine the potential of working electrode. It has a well-defined and stable equilibrium potential as long as no current flows through it.

For electrochemical investigation the analyte was dispersed in a suitable solvent consisting of a tetrabutyl ammonium perchlorate (TBAP) or tetra butyl ammonium hexafluoro phosphate (TBAHFP) as a supporting electrolyte. Before investigation it is necessary to sparge the electrolyte solution with an inert gas for half an hour in order to remove dissolved oxygen as oxygen undergoes reversible one-electron reduction to form the oxygen radical anion, $O_2^{\bullet-}$ (superoxide).[66,67] Now, the voltammetric experiment were carried out by immersing the electrodes in a solution with varying applied potential within the set potential window. Figure 2.15 shows the experimental set up of cyclic voltammetry.
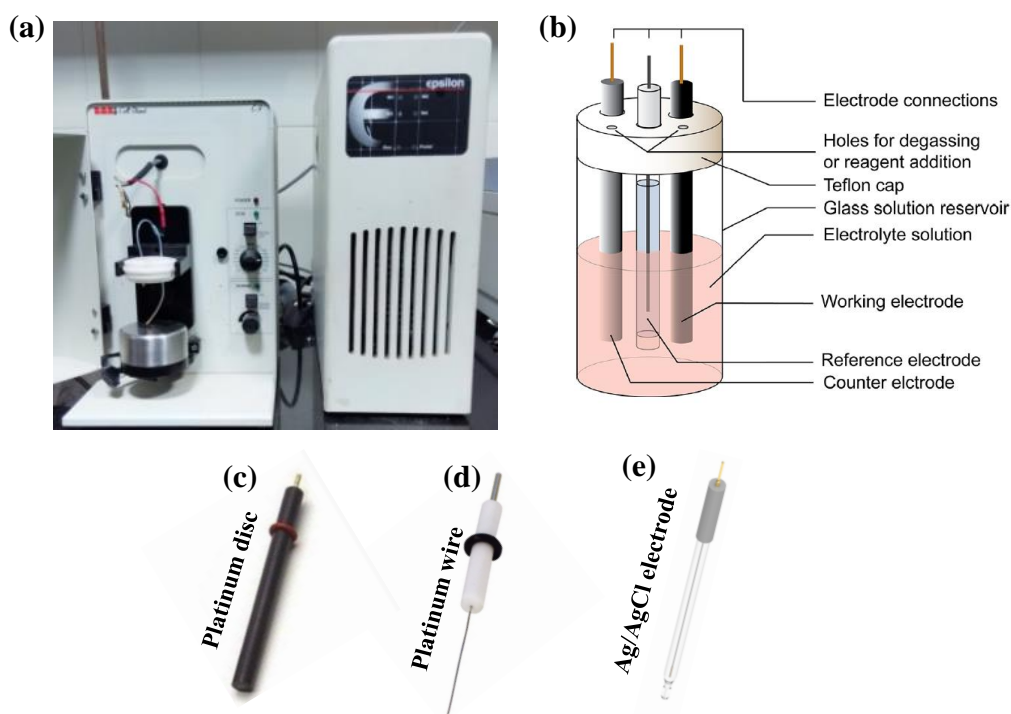
Figure 2.15: (a) BASi Epsilon electrochemical analyser; (b) systematic representation for an electrochemical CV experiment; (c) Pt electrode; (d) Pt wire and (e) Ag/AgCl electrode.

2.2.2.7. Transmission Electron Microscopy (TEM)

Transmission electron microscopy is considered to be a best suited analytical technique generally used for investigating the particle size, morphology, defects, crystallographic structure and even composition of the material.[68–70] It delivers a chemical information and images of nanoparticles at a level of atomic dimensions provided at specific resolution. It is very much similar to that of a light microscope whereby an electromagnetic wave is substituted by a beam of electrons, glass lenses by electromagnetic lenses and images are viewed in a screen instead of an eyepiece. During analysis an incident beam of electron is transmitted via an ultra-thin material thereby interreacting with the materials forming an image by the elastic and inelastic scattering of electron. The formed image is magnified and focused onto a fluorescent screen and get detected by a sensor such as a CCD camera. It is found that the elastic scattering of electron increases with the increase in atomic number and decrease with the increase in the electron beam energy whereas in case of inelastic scattering the probability depends upon the electronic structure of the element in the material. Both TEM and SEM examine the size, degree of aggression and dispersion as well as the heterogeneity of

the nanomaterials but in comparison to SEM, TEM has much more importance as it provide better resolution in good quality and provision of information regarding compound and element structure.

Unlike optical microscopy, electron microscopy has capability of imagining at a higher resolution by the interference of elastic scattered electron owing to the small De Broglie wavelength of electrons.[70–72] Thus, it leads the instrument to determine the finest micrographs about the internal lattice arrangement of the sample which is thousand times smaller than the resolved object seen in the light microscope. When the electron beam is exactly in the direction of the crystallographic orientations such micrographs will be readily obtained provided the crystallographic orientation has lower Miller indices. Furthermore, it provides a precise particle size of bright field images as well as dark field images. The bright field image is formed by passing an electron without diffraction on the thin film of sample but in case of dark field imaging mode, the diffracted beam is used for imaging.

The unprecedented high resolution and accuracy, high contrast, and a remarkable range of analytical capabilities have made TEM the leading technology. It is a powerful technique that form major analysis in the field of material science, virology, cancer research as well as pollution and semiconductor research.

2.2.2.7.1. Experimental Set-Up

The TEM images of as-synthesized QDs were taken in JEOL-JEM-2100 Plus electron microscope. The high-resolution TEM (HRTEM) images were obtained using 200 kV electron source. At first, the synthesized materials were washed and diluted in hexane followed by drop-casting of nanocrystal solution on a carbon coated copper grid, the grids were kept overnight in a vacuum desiccator. The lattice plane was obtained from lattice fringes using Image J software for calculations. The figure 2.16 shows the instrumental set up of TEM. TEM comprises of electron source to deliver electrons which is made up of hairpin like tungsten wire, thermionic gun to shoot the electrons from electron source, two condensers, electromagnetic lenses, electron beam, fluorescent screen, sample stage, vacuum chamber and computer. During analysis, TEM follows two methods for material observation viz. image mode and diffraction mode. While investigating an image mode, the beam of electron is controlled by the condenser lens and aperture before irradiating the specimen. The transmitted beam after interacting with the specimen will be focused thereby enlarged by the objective and

projector lens to form an image in the screen. In diffraction mode, illumination of electron beam results into the diffraction of signal on the fluorescent screen arising from the sample area. The signal formed after diffraction is equivalent to X-ray diffraction signal. The grain size and the lattice defects are analysed by an image mode whereas crystalline structure is examined by the diffraction mode.
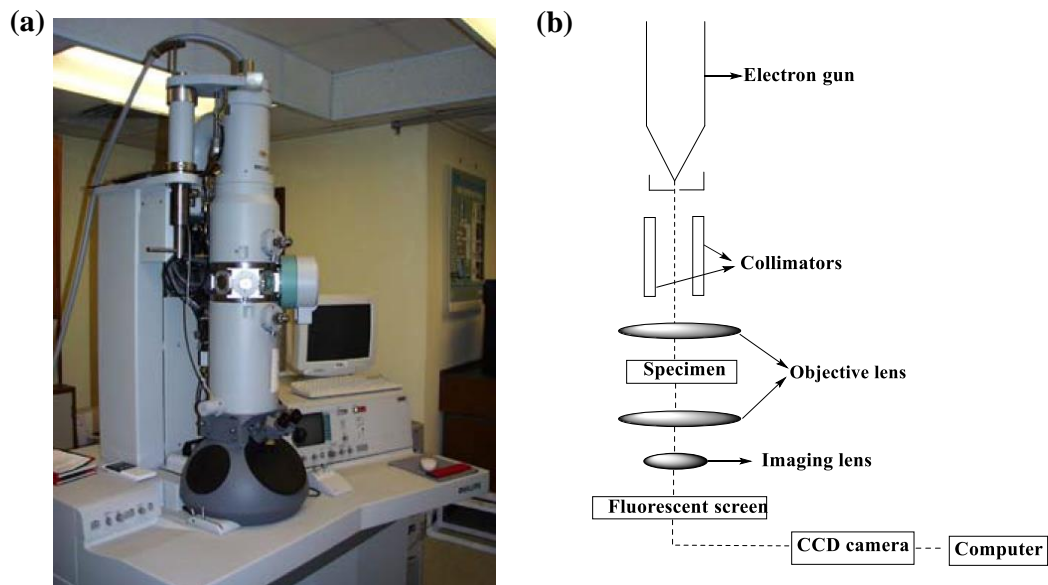
Figure 2.16: (a) Image of Transmission Electron Microscopy; (b) Systematic diagram of TEM analyser.

2.2.2.8. X-ray Photoelectron Spectroscopy (XPS)

XPS is a powerful analytical technique extensively used for the analysis of the surface of the materials. The method is effective for determination of oxidation state and chemical environment of the element. The method is also known as Electron Spectroscopy for Chemical Analysis (ESCA).[73] In this technique, photoelectrons excited by monochromatic X-ray radiation, hυ penetrating deep into the sample surface as a result of which electron get emitted from the lower energy X-rays evolving from inner atomic energy level where it is bound to the atomic nucleus with binding energy (BE). The emitted electron has measured kinetic energies as given by;[70,72,74,75]

$$KE = h\upsilon - BE - \phi_s \dots\dots\dots\dots\dots (i)$$

Where, hυ is the energy of the photon, BE is the binding energy of the atomic orbital from where the electron gets emitted and ϕ_s is the spectrometer work function.

The energy spectrum of the emitted photoelectron is determined by high-resolution electron spectrometer. The measured spectrum comprises of representative peaks which corresponds to electronic energy level of the analysed sample. The electron on the sample is characterised by their binding energies because each element possesses unique set of BE, thus, XPS can be used to identify and determine the concentration of the elemental composition of the sample at the surface. Furthermore, from the XPS data we can also determine the empirical formula of samples of interest. Also, it has capability to examine the chemical state of the investigated sample from their chemical shift and helps to determine the chemical state of the material. The shift in signal arises due the different chemical environment of the element in the compound, thus, oxidation state of the sample, bonding in polymer can be analysed.

2.2.2.8.1. Experimental Set-Up

The schematic diagram of XPS is shown in figure 2.17. XPS spectra were collected using Thermo-Scientific ESCALAB Xi^+ spectrometer with Al Kα (1486.7 eV) X-ray source. For high resolution spectra constant analyser energy (CAE) of 50 eV was used and for survey spectra (CAE) of 100 eV. It consists of an ultra-high vacuum (UHV) chamber, an electron collection lenses, an electron energy analyser, an electron detector system, a sample introduction chamber, sample mounts, a sample stage having ability to heat or cool the sample and a set of stage manipulators.
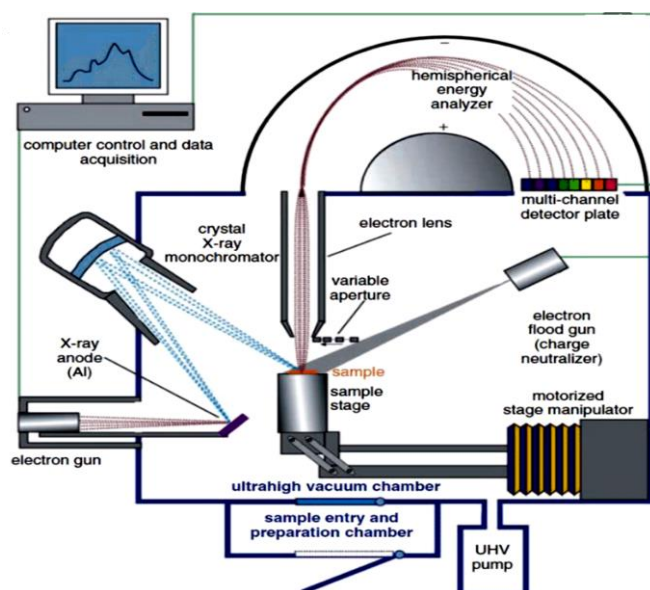
Figure 2.17: Systematic diagram of XPS analyser.

It depends upon the photoelectric effect which leads to continuous loss of electron from the surface of species into vacuum and enters the analyser slit of the spectrometer which is capable of measuring electron current as a function of energy. The most prevalent electron spectrometer for XPS is the hemispherical electron analyser with high energy resolution. Electrons are detected using electron multipliers. The plot of intensity vs energy gives XPS spectra.

References

(1)   Wang, Y.; Xia, Y. Bottom-Up and Top-Down Approaches to the Synthesis of Monodispersed Spherical Colloids of Low Melting-Point Metals. *Nano Lett.* **2004**, *4*, 2047–2050.

(2)   Pradhan, N. Journey of Making Cesium Lead Halide Perovskite Nanocrystals: What's Next. *J. Phys. Chem. Lett.* **2019**, *10*, 5847–5855.

(3)   Schlipf, J.; Askar, A. M.; Pantle, F.; Wiltshire, B. D.; Schneider, P.; Huber, L.; Shankar, K.; Müller-buschbaum, P. Top-Down Approaches Towards Single Crystal Perovskite Solar Cells. *Sci. Rep.* **2018**, *8*, 1–8.

(4)   Xie, L.; Lin, K.; Lu, J.; Feng, W.; Song, P.; Yan, C.; Liu, K.; Shen, L.; Tian, C.; Wei, Z. Efficient and Stable Low-Bandgap Perovskite Solar Cells Enabled by a $CsPbBr_3$ - Cluster Assisted Bottom-up Crystallization Approach. *J. Am. Chem. Soc.* **2019**, *141*, 20537–20546.

(5)   Sardar, S.; Jana, A.; Mukherjee, A.; Dhara, A.; Bandyopadhyay, A. Bottom-up Synthesis of Bright Fluorescent, Moisture-Resistant Methylammonium Lead Bromide Poly(3-Bromothiophene). *New J. Chem* **2020**, *44*, 2053–2058.

(6)   Yoon, K. Liquid-Phase Bottom-up Synthesis of Graphene Nanoribbons. *Mater. Chem. Front* **2020**, *4*, 29–45.

(7)   Zhuang, Z.; Peng, Q.; Li, Y. Controlled Synthesis of Semiconductor Nanostructures in the Liquid Phase. *Chem. Soc. Rev.* **2011**, *40*, 5492–5513.

(8)   Chang, J.; Waclawik, E. R. Colloidal Semiconductor Nanocrystals : Controlled Synthesis and Surface Chemistry in Organic Media. *RSC Adv.* **2014**, *4*, 23505–23527.

(9)   Li, Z.; Hu, Q.; Tan, Z.; Yang, Y.; Leng, M.; Liu, X.; Ge, C.; Niu, G.; Tang, J. Aqueous Synthesis of Lead Halide Perovskite Nanocrystals with High Water Stability and Bright Photoluminescence. *ACS Appl. Mater. Interfaces* **2018**, *10*,

43915–43922.

(10) Jing, L.; Kershaw, S. V; Li, Y.; Huang, X.; Li, Y.; Rogach, A. L.; Gao, M. Aqueous Based Semiconductor Nanocrystals. *Chem. Rev.* **2016**, *116*, 10623–10730.

(11) Chiang, C. H.; Wu, C. G. A Method for the Preparation of Highly Oriented MAPbI$_3$ Crystallites for High-Efficiency Perovskite Solar Cells to Achieve an 86% Fill Factor. *ACS Nano* **2018**, *12*, 10355–10364.

(12) Shamsi, J.; Urban, A. S.; Imran, M.; Trizio, L. De; Manna, L. Metal Halide Perovskite Nanocrystals : Synthesis , Post-Synthesis Modifications , and Their Optical Properties. *Chem. Rev.* **2019**, *119*, 3296–3348.

(13) Cao, M.; Djerdj, I.; Antonietti, M.; Niederberger, M.; August, R. V. Nonaqueous Synthesis of Colloidal ZnGa$_2$O$_4$ Nanocrystals and Their Photoluminescence Properties Fluorescent Semiconductor Nanocrystals Have Attracted Intensive Interest during the Past Decade Because of Their Promising Applications in Various Fields. *Chem. Mater.* **2016**, *19*, 5830–5832.

(14) Ye, Q.; Zhang, J.; Guo, P.; Fan, H.; Shchukin, D.; Wei, B.; Wang, H. Wet-Chemical Synthesis of Surface-Passivated Halide Perovskite Microwires for Improved Optoelectronic Performance and Stability. *ACS Appl. Mater. Interfaces* **2018**, *10*, 43850–43856.

(15) Chan, E. M.; Xu, C.; Mao, A. W.; Han, G.; Owen, J. S.; Cohen, B. E.; Milliron, D. J. Reproducible, High-Throughput Synthesis of Colloidal Nanocrystals for Optimization in Multidimensional Parameter Space. *Nano Lett.* **2010**, *10*, 1874–1885.

(16) Faraday, M. The Bakerian Lecture : Experimental Relations of Gold (and Other Metals) to Light. *Phil. Trans. R. Soc. Lond.* **1857**, *147*, 145–181.

(17) Murray, C. B.; Noms, D. J.; Bawendi, M. G. Synthesis and Characterization of Nearly Monodisperse CdE (E = S, Se, Te) Semiconductor Nanocrystallites. *J. Am. Chem. Soc.* **1993**, *115*, 8706–8715.

(18) Zacharaki, E.; Kalyva, M.; Fjellvåg, H.; Sjåstad, A. O. Burst Nucleation by Hot Injection for Size Controlled Synthesis of ε - Cobalt Nanoparticles. *Chem. Cent. J.* **2016**, *10*, 1–11.

(19) Murray, C. B.; Norris, D. J.; Bawendi, M. G. Synthesis and Characterization of Nearly Monodisperse CdE (E = S , Se , Te) Semiconductor Nanocrystallites. *J. Am. Chem. Soc.* **1993**, *115*, 8706–8715.

(20)   Lamer, V. K.; Dinegar, H. Theory, Production and Mechanism of Formation of Monodispersed Hydrosols. *J. Am. Chem. Soc.* **1950**, *72*, 4847–4854.

(21)   Protesescu, L.; Yakunin, S.; Bodnarchuk, M. I.; Krieg, F.; Caputo, R.; Hendon, C. H.; Yang, R. X.; Walsh, A.; Kovalenko, M. V. Nanocrystals of Cesium Lead Halide Perovskites ($CsPbX_3$, X = Cl, Br, and I): Novel Optoelectronic Materials Showing Bright Emission with Wide Color Gamut. *Nano Lett.* **2015**, *15*, 3692–3696.

(22)   Ravi, V. K.; Markad, G. B.; Nag, A. Band Edge Energies and Excitonic Transition Probabilities of Colloidal $CsPbX_3$ (X = Cl, Br, I) Perovskite Nanocrystals. *ACS Energy Lett.* **2016**, *1*, 665–671.

(23)   Akkerman, Q. A.; Rainò, G.; Kovalenko, M. V.; Manna, L. Genesis, Challenges and Opportunities for Colloidal Lead Halide Perovskite Nanocrystals. *Nat. Mater.* **2018**, *17*, 394–405.

(24)   Shamsi, J.; Urban, A. S.; Imran, M.; De Trizio, L.; Manna, L. Metal Halide Perovskite Nanocrystals: Synthesis, Post-Synthesis Modifications, and Their Optical Properties. *Chem. Rev.* **2019**, *119*, 3296–3348.

(25)   Park, J.; An, K.; Hwang, Y.; Park, J.; Noh, H.; Kim, J.; Park, J.; Hwang, N.; Hyeon, T. Ultra-Large-Scale Syntheses of Monodisperse Nanocrystals. *Nat. Mater.* **2004**, *3*, 891–895.

(26)   Park, J.; Joo, J.; Kwon, S. G.; Jang, Y.; Hyeon, T. Synthesis of Monodisperse Spherical Nanocrystals Angewandte. *Angew. Chem. Int. Ed.* **2007**, *46*, 4630–4660.

(27)   Lee, D.; Kim, M. H.; Woo, H. Y.; Chae, J.; Lee, D.; Jeon, S.; Oh, S. J.; Paik, T. Heating-up Synthesis of Cesium Bismuth Bromide Perovskite Nanocrystals with Tailored Composition, Morphology, and Optical Properties. *RSC Adv.* **2020**, *10*, 7126–7133.

(28)   Tamang, S.; Lincheneau, C.; Hermans, Y.; Jeong, S.; Reiss, P. Chemistry of InP Nanocrystal Syntheses. *Chem. Mater.* **2016**, *28*, 2491−2506.

(29)   Van Embden, J.; Chesman, A. S. R.; Jasieniak, J. J. The Heat-up Synthesis of Colloidal Nanocrystals. *Chem. Mater.* **2015**, *27*, 2246–2285.

(30)   Zhao, Y. S.; Fu, H.; Peng, A.; Ma, Y.; Xiao, D.; Yao, J. Low-Dimensional Nanomaterials Based on Small Organic Molecules: Preparation and Optoelectronic Properties. *Adv. Mater.* **2008**, *20*, 2859–2876.

(31)   Kasai, H.; Nalwa, H. S.; Oikawa, H.; Okada, S.; Matsuda, H.; Minami, N.;

Kakuta, A.; Ono, K.; Mukoh, A.; Nakanishi, H. A Novel Preparation Method of Organic Microcrystals. *Jpn. J. Appl. Phys.* **1992**, *31*, 1132–1134.

(32)   Wei, S.; Yang, Y.; Kang, X.; Wang, L.; Huang, L.; Pan, D. Room-Temperature and Gram-Scale Synthesis of. *Chem. Commun.* **2016**, *52*, 7265–7268.

(33)   Ng, C. K.; Yin, W.; Li, H.; Jasieniak, J. J. Scalable Synthesis of Colloidal CsPbBr$_3$ Perovskite Nanocrystals with High Reaction Yields through Solvent and Ligand Engineering. *Nanoscale* **2020**, *12*, 4859–4867.

(34)   Sun, S.; Yuan, D.; Xu, Y.; Wang, A.; Deng, Z. Ligand-Mediated Synthesis of Shape-Controlled Cesium Lead Halide Perovskite Nanocrystals via Reprecipitation Process at Room Temperature. *ACS Nano* **2016**, *10*, 3648–3657.

(35)   Shamsi, J.; Rastogi, P.; Caligiuri, V.; Abdelhady, A. L.; Spirito, D.; Manna, L.; Krahne, R. Bright-Emitting Perovskite Films by Large-Scale Synthesis and Photoinduced Solid-State Transformation of CsPbBr$_3$ Nanoplatelets. *ACS Nano* **2017**, *11*, 10206–10213.

(36)   Papavassiliou, G. C.; Pagona, G.; Karousis, N.; Mousdis, G. A.; Koutselas, I.; Vassilakopoulou, A. Nanocrystalline/Microcrystalline Materials Based on Lead-Halide Units. *J. Mater. Chem.* **2012**, *22*, 8271–8280.

(37)   Zhang, F.; Zhong, H.; Chen, C.; Wu, X. G.; Hu, X.; Huang, H.; Han, J.; Zou, B.; Dong, Y. Brightly Luminescent and Color-Tunable Colloidal CH$_3$NH$_3$PbX$_3$ (X = Br, I, Cl) Quantum Dots: Potential Alternatives for Display Technology. *ACS Nano* **2015**, *9*, 4533–4542.

(38)   Yang, B.; Chen, J.; Hong, F.; Mao, X.; Zheng, K.; Yang, S.; Li, Y.; Pullerits, T.; Deng, W.; Han, K. Lead-Free, Air-Stable All-Inorganic Cesium Bismuth Halide Perovskite Nanocrystals. *Angew. Chemie - Int. Ed.* **2017**, *56*, 12471–12475.

(39)   Povrozin, Y.; Barbieri, B. Fluorescence Spectroscopy; Handbook of Measurement in Science and Engineering, John Wiley & Sons. **2016**, *3*, 2475–2498.

(40)   Karoui, R.; Blecker, C. Fluorescence Spectroscopy Measurement for Quality Assessment of Food Systems-a Review. *Food Bioprocess Technol.* **2011**, *4*, 364–386.

(41)   Romani, A.; Clementi, C.; Miliani, C.; Favaro, G. Fluorescence Spectroscopy: A Powerful Technique for the Noninvasive Characterization of Artwork. *Acc. Chem. Res.* **2010**, *43*, 837–846.

(42)   F, H. C.; E, S. R. Tutorial on Powder X-Ray Diffraction for Characterizing

Nanoscale Materials. *ACS Nano* **2019**, *13*, 7359–7365.

(43) Lansing, E. Principles of Powder Diffraction. *R. Soc. Chem.* **2008**, *20*, 1–19.

(44) Bunaciu, A. A.; S, E. G. U. X-Ray Diffraction : Instrumentation and Applications. *Crit. Rev. Anal. Chem.* **2015**, *45*, 289–299.

(45) Thakral, N. K.; Zanon, R. L.; Kelly, R. C.; Thakral, S. Applications of Powder X-Ray Diffraction in Small Molecule Pharmaceuticals : Achievements and Aspirations. *J. Pharm. Sci.* **2018**, *107*, 2969–2982.

(46) Ismail, A. A.; Voort, F. R. Van De; Sedman, J. Chapter 4 Fourier Transform Infrared Spectroscopy : Principles and Applications. *Tech. Instrum. Anal. Chem.* **1997**, *18*, 93–139.

(47) Furutani, Y.; Shimizu, H.; Asai, Y.; Fukuda, T.; Oiki, S.; Kandori, H. ATR-FTIR Spectroscopy Revealing the Different Vibrational Modes of the Selectivity Filter Interacting with K^+ and Na^+ in the Open and Collapsed Conformations of the KcsA Potassium Channel. *J. Phys. Chem. Lett.* **2012**, *3*, 3806–3810.

(48) Solteira, I.; Solteira, I.; Solteira, I. Infrared Specgtroscopy : A Tool for Determination of the Degree of Conversion In. *J Appl Oral Sci.* **2008**, *16*, 145–149.

(49) Coates, J. Interpretation of Infrared Spectra , A Practical Approach. *Encycl. Anal. Chem.* **2006**, 1–23.

(50) Mantele, W.; Deniz, E. UV-VIS Absorption Spectroscopy: Lambert-Beer Reloaded. *Spectrochem. acta* **2016**, *173*, 965–968.

(51) Klotz, I. M. Ultraviolet Absorption Spectroscopy. *J. Chem. Educ.* **1945**, *22*, 328–336.

(52) Coats, A. W.; Redfern, J. P. Thermogravimetric Analysis. *Analyst* **1963**, *88*, 906–924.

(53) Sharp, J. H. Thermal Analysis. *Proc. Soc. Anal. Chem* **1971**, *8*, 112–115.

(54) Dollimore, D.; Lerdkanchanaporn, S. Thermal Analysis. *Anal. Chem.* **1998**, *70*, 27–36.

(55) Simon, J. Introduction to Thermal Analysis Techniques Applications. Brown, M. E., Ed.; Kluwer Academic Publishers, **2001**.

(56) Mabboil, G. A. An Introduction to Cyclic Voltammetry. *J. Chem. Educ.* **1983**, *60*, 697–702.

(57) Elgrishi, N.; Rountree, K. J.; McCarthy, B. D.; Rountree, E. S.; Eisenhart, T. T.; Dempsey, J. L. A Practical Beginner's Guide to Cyclic Voltammetry. *J. Chem.*

Educ. **2018**, *95*, 197–206.

(58) Sandford, C.; Edwards, M. A.; Klunder, K. J.; Hickey, D. P.; Li, M.; Barman, K.; Sigman, M. S.; White, H. S.; Minteer, S. D. A Synthetic Chemist's Guide to Electroanalytical Tools for Studying Reaction Mechanisms. *Chem. Sci.* **2019**, *10*, 6404–6422.

(59) Killa, M.; Mercer, E. E.; Philp, R. H. Applications of Cyclic Voltammetry in the Characterization of Complexes at Low Ligand Concentrations. *Anal. Chem.* **1984**, *56*, 2401–2405.

(60) Querner, C.; Reiss, P.; Sadki, S.; Zagorska, M.; Pron, A. Size and Ligand Effects on the Electrochemical and Spectroelectrochemical Responses of CdSe Nanocrystals. *Phys.Chem.Chem. Phys* **2005**, *7*, 3204 –3209.

(61) Inamdar, S. N.; Ingole, P. P.; Haram, S. K. Determination of Band Structure Parameters and the Quasi-Particle Gap of CdSe Quantum Dots by Cyclic Voltammetry. *ChemPhysChem* **2008**, *9*, 2574–2579.

(62) Kucur, E.; Riegler, J.; Urban, G. A.; Nann, T. Determination of Quantum Confinement in CdSe Nanocrystals by Cyclic Voltammetry. *J. Chem. Phys.* **2003**, *199*, 2333–2337.

(63) Haram, S. K.; Quinn, B. M.; Bard, A. J. Electrochemistry of CdS Nanoparticles: A Correlation between Optical and Electrochemical Band Gaps. *J. Am. Chem. Soc.* **2001**, *123*, 8860–8861.

(64) Haram, S. K.; Kshirsagar, A.; Gujarathi, Y. D.; Ingole, P. P.; Nene, O. A.; Markad, G. B.; Nanavati, S. P. Quantum Confinement in CdTe Quantum Dots : Investigation through Cyclic Voltammetry Supported by Density Functional Theory (DFT). *J. Phys. Chem. C* **2011**, *115*, 6243–6249.

(65) Hart, N. T.; Lane, W. C.; Garza, L. De. Electrochemical Quanti Fi Cation of Acetaminophen: An Engaging Cyclic Voltammetry Laboratory for the Quantitative Analysis Course. *J. Chem. Educ.* **2020**, *97*, 2254–2259.

(66) Hayyan, M.; Hashim, M. A.; Alnashef, I. M. Superoxide Ion: Generation and Chemical Implications. *Chem. Rev.* **2016**, *116*, 3029–3085.

(67) Jalilov, A. S.; Zhang, C.; Samuel, E. L. G.; Sikkema, W. K. A.; Wu, G.; Berka, V.; Kent, T. A.; Tsai, A. L.; Tour, J. M. Mechanistic Study of the Conversion of Superoxide to Oxygen and Hydrogen Peroxide in Carbon Nanoparticles. *ACS Appl. Mater. Interfaces* **2016**, *8*, 15086–15092.

(68) Nakamura, E.; Editor, G.; Sommerdijk, N. A. J. M.; Editor, G. Transmission

Electron Microscopy for Chemists. *Acc. Chem. Res.* **2017**, *50*, 1795–1796.

(69) Denny, M. S.; Parent, L. R.; Patterson, J. P.; Meena, S. K.; Pham, H.; Abellan, P.; Ramasse, Q. M.; Paesani, F.; Gianneschi, N. C.; Cohen, S. M. Transmission Electron Microscopy Reveals Deposition of Metal Oxide Coatings onto Metal − Organic Frameworks. *J. Am. Chem. Soc.* **2018**, *140*, 1348–1357.

(70) Ma, H.; Shieh, K.-J.; Qiao, T. X. Study of Transmission Electron Microscopy (TEM) and Scanning Electron Microscopy (SEM). *Nat. Sci.* **2006**, *4*, 14–22.

(71) Senthil Kumar, P.; Grace Pavithra, K.; Naushad, M. Characterization Techniques for Nanomaterials. *Nanomaterials for Solar Cell Applications* **2019,** *47*, 97-124.

(72) Kaech, A. An Introduction To Electron Microscopy Instrumentation, Imaging and Preparation. *Cent. Microsc. Image Anal.* **2013**, *25*, 1–26.

(73) Oswald, S. X-Ray Photoelectron Spectroscopy in Analysis of Surfaces, *John Wiley & Sons* **2013**.

(74) Markus, A. X-Ray Photoelectron Spectroscopy (XPS) as Part of the Course 'Characterization of Catalysts and Surfaces'. *IM Publications and Surface Spectra Ltd.* **2003**.

(75) Briggs, D. X-Ray Photoelectron Spectroscopy (XPS), *Perkin-Elmer Corporation*. **2005**.

CHAPTER III

SYNTHESIS AND CHARACTERIZATION OF COLLOIDAL CsPbBr$_3$ QDs

SYNTHESIS AND CHARACTERIZATION OF COLLOIDAL CsPbBr$_3$ QDs

3.1. Preparation of colloidal CsPbBr$_3$ perovskite QDs

The colloidal CsPbBr$_3$ QDs were synthesized following the "three precursor method" providing an individual tunning of the amount of all the three precursors *viz.* cesium oleate (CsOl), lead acetate Pb(OAc)$_2$, and molecular bromine (Br$_2$). The method is versatile for the synthesis of surface control and desired halide rich perovskite QDs. Herein, we synthesized halide-rich passivated CsPbBr$_3$ QDs in the ratio of Cs:Pb:Br~1:1:6 at high temperature. The reaction procedure for the synthesis of precursor, CsOl and CsPbBr$_3$ QDs were illustrated below.

3.1.1. Synthesis of Cesium Oleate Precursor
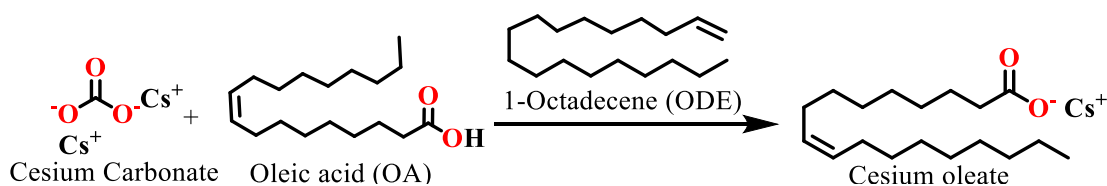
Cesium oleate was prepared by dissloving 0.81 g (2.5 mmol) of cesium carbonate (Cs$_2$CO$_3$) in 20 mL 1-octadecene (ODE) and 2.5 mL oleic acid (OA) in a 50 mL of two-necked round bottom flask. The solution was degassed under vacuum at room temperature for 30 min with constant stirring followed by degassing at 120 °C for another 30 min in an oil bath under vacuum until the clear solution was obtained. The formed transparent (CsOl) solution was kept in an inert atmospheric condition at 100 °C for future use.

3.1.2. General Synthesis of CsPbBr₃ QDs

$$Pb(OAc)_2 \; + \text{1-ODE} + OA \; + \; Br_2 \; \xrightarrow[\substack{\text{Ce-oleate} \\ 200\ ^\circ C}]{\text{Oleylamine (OAm)}} \; \textbf{CsPbBr}_3$$
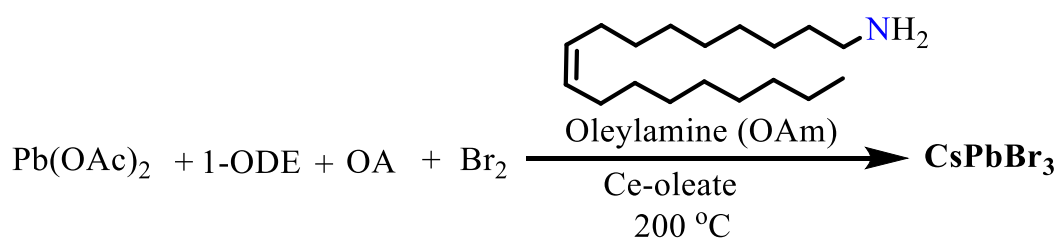
In a 50 mL of three-necked round bottom flask, 0.13 g of Pb(OAc)₂ (0.4 mmol) was dissolved in 16 mL of 1-octadecene (ODE) followed by the addition of 0.8 mL of oleic acid (OA) and 2 mL of oleyl amine (OAm). The solution mixture was mixed vigorously to ensure the complete dissolution of Pb(OAc)₂. To this reaction mixture, 2.4 mmol of molecular bromine was added (Warning: Br₂ was handled inside the fume hood as bromine vapours is hazardous to health). After complete set-up, the reaction mixture was degassed under vacuum at room temperature for half an hour followed by degassing at 120 °C for another 30 min in an oil-bath for complete removal of dissolved oxygen and water molecules present in the reaction mixture. The systematic representation for the preparation of CsPbBr₃ QDs were shown in figure 3.1. (a) and (b). Subsequently, the desired reaction temperature and time was maintained under inert atmospheric condition. After attaining the appropriate reaction injection temperature (200 °C), 0.8 mL of preheated cesium oleate solution synthesized in section 3.1.1 was injected swiftly into an opaque reaction mixture and within a few seconds the reaction mixture was quenched in an ice-water bath to obtained a small QDs of narrow size distribution. Figure 3.1. (c) represents the colloidal dispersion of as-synthesized QDs in hexane under the UV-lamp showing bright green luminescence.
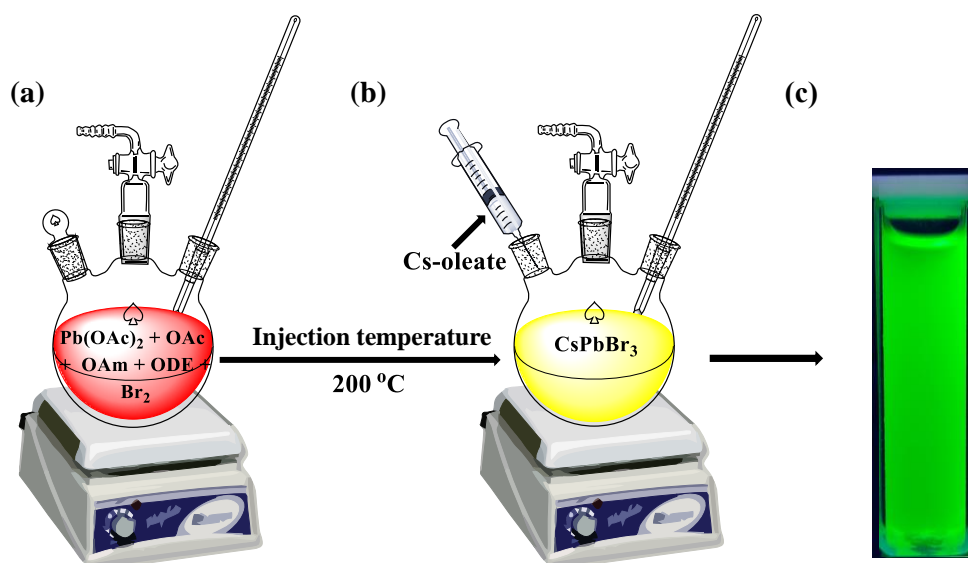
Figure 3.1: Experimental set-up for the preparation of CsPbBr$_3$ QDs (a) before injection of Cs-oleate precursor, (b) after injection of Cs-oleate precursor, and (c) colloidal dispersion of formed CsPbBr$_3$ QDs in hexane under UV-lamp.

The formed colloidal solution of CsPbBr$_3$ QDs was washed using dry toluene through centrifugation at 5000 rpm for 10 min. After repeating the washing process twice, the purified QDs was vacuumed for 1 h to obtain solid NCs. The digital photograph of crushed powder form of hardened jelly mass of the QDs under ambient light and UV lamp is demonstrated in the figure 3.2.
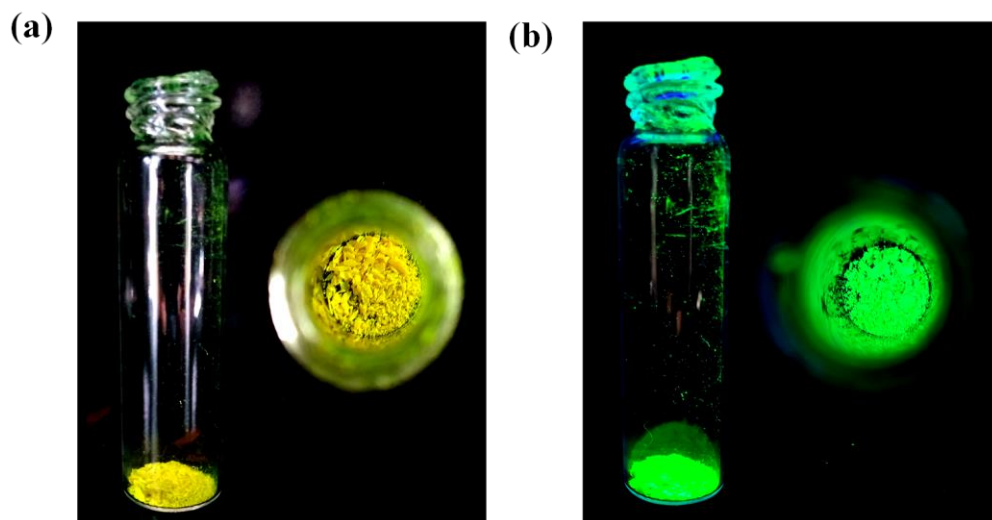
Figure 3.2: A representative image of purified CsPbBr$_3$ QDs (a) under ambient and (b) UV-lamp.

3.2. Characterization

The synthesized $CsPbBr_3$ QDs were characterized using conventional tools such as optical characterization (UV and PL), PXRD, FT-IR, XPS, TEM, TGA and CV.

3.2.1. Optical characterization

The absorption spectra of purified QDs were characterized using UV-visible absorption spectroscopy. The sample was prepared in 1 cm path length quartz cuvette fitted with an air-tight screw cap by dispersing minimum concentration of purified QDs in dry hexane solvent. QDs shows a strong absorption maximum at around 505 nm. The determination of the optical band-gap, of the as-synthesized QDs were carried out by taking the onset absorption edge, which is the higher-energy state of an electron after being excited by photon.[1] The optical band gap was found to be 2.45 eV.

Similarly, the same dispersed QDs was examined using steady-state PL spectrofluorometer on excitation at 400 nm. QDs exhibit PL emission maximum at 517 nm with narrow full width half-maximum (FWHM) of 28 nm. The emission line width and low FWHM confirm the narrow size distribution of QDs.[2–5] Figure 3.3. shows the absorption and emission maximum spectra of as-prepared $CsPbBr_3$ QDs. The observed absorption and emission spectra of QDs are very much consistence with the standard halide rich $CsPbBr_3$ QDs.[6]
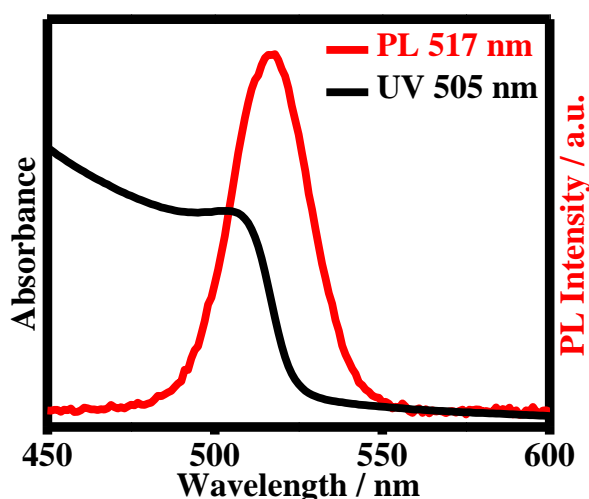
Figure 3.3: UV−visible absorption and PL spectra (exited at 400 nm) of $CsPbBr_3$ QDs in dry hexane.

3.2.2. X-ray Diffraction (XRD)

The dispersed concentrate solution of purified QDs in dry hexane were drop-casted on a clean and dry glass slide. The film on glass slide was run under the PANalytical X-Ray diffractometer using Cu Kα (λ= 1.54 Å) as the incident radiation (40 kV and 30 mA). The obtained X-ray diffraction patterns of QDs shows strong and distinct peak at (2θ) 15.33°, 21.62°, 30.75°, 34.43°, 37.85°, and 43.96° that corresponded to diffractions from the (100), (110), (200), (210), (211), and (220) crystal planes, respectively. The obtained peaks were correlated with the JCPDS card no. 00-054-0752 and was noted that all the peaks get well match with cubic phase which is shown in figure 3.4.
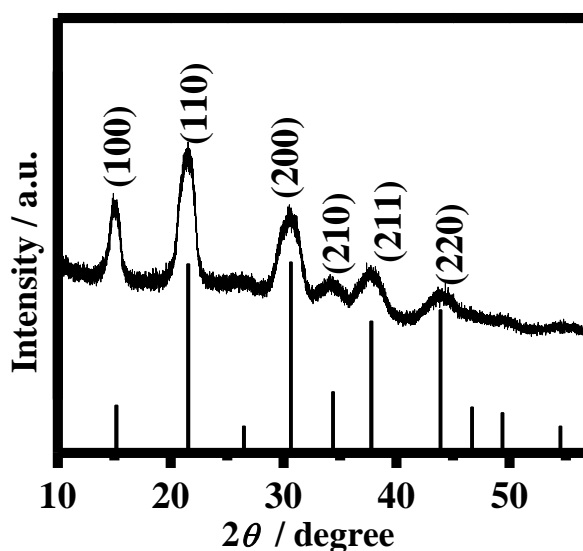
Figure 3.4: Powder X-ray diffractogram of as prepared CsPbBr$_3$ QDs confirming the cubic perovskite phase indicated as bars (JCPDS No. 00-054-0752).

Herein, we noted that there is slight shift in the 2θ angle towards small angle direction which may be attributed to ionic radius of bromine or due to the formation of an alloys and the results were found to be consistence as reported by others.[3,4,7,8] It was noted that the XRD pattern does not possess the peaks from either of the PbBr$_2$ and CsBr.[2,9] Furthermore, the highly crystalline and pure cubic phase of QDs without any defects was attributed from the intense diffraction from the (200) plane at 30.75 and its corresponding appearance with the secondary diffraction from the (100) plane at 15.33.[4] A well definite line broadening of the XRD-peaks confirm that the prepared material consists of particles in nanoscale range. The as-synthesized QDs shows long term stability in ambient air for a period of 30 days as shown in figure 3.5.
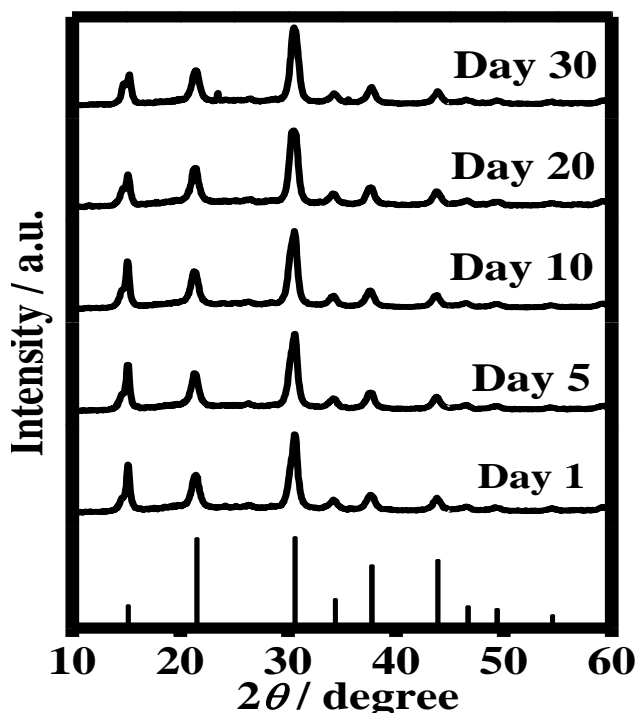
Figure 3.5: Powder X-ray diffractogram of as-synthesized QDs showing long term stability in ambient air for a period of 30 days.

3.2.3. X-ray Photoelectron Spectroscopy (XPS)

The XPS spectra of purified QDs were recorded using Thermo-Scientific ESCALAB Xi$^+$ spectrometer with Al Kα (1486.7 eV) X-ray source. For high resolution spectra constant analyser energy (CAE) of 50 eV was used and 100 eV for survey spectra. The analysis was performed by fabricating the purified QDs on a carbon coated silicon wafers to minimize charging in a glovebox. The previous studies have reported that the enhance phase stability of colloidal α-CsPbX$_3$ (X = Cl, Br, and I) is very much influential towards surface chemistry.[10–12] Thus, it was found that the exceptional air-stability of colloidal QDs crystallizing in a cubic phase is dominantly due to the halide salt passivation on the surface of NCs as depicted through XPS analyser. The XPS spectra were corrected using the maximum of the C 1s signal at 284.8 eV as shown in figure 3.5. (d) It is clear from the XPS survey (*figure 3.6*) that the Pb 4f core level spectra of QDs display a prominent two peaks at 138.4 and 143.2 eV which corresponds to the Pb 4f$_{7/2}$ and Pb 4f$_{5/2}$ levels respectively. The observed binding energy values is found to be slightly higher which corresponds to bromide rich surface passivation and found to be consistent with the previously reported CsPbBr$_3$ QDs.[13,14] Furthermore, Liu *et.al.* describe the XPS spectra of N 1s core level confirming the presence of protonated amine (NH$_3^+$) group at 401.8 eV which is in good agreement with our observation

(401.0 eV) as shown in figure 3.5.(e).[15] Further investigation of the Cs 3d, Pb 4f, and Br 3d peaks confirmed that the obtained CsPbBr$_3$ QDs surface is passivated by a bromide ion rich concentration (Cs: Pb: Br ~ 0.9:1:3.5). Thus, the long-term cubic phase stability of CsPbBr$_3$ QDs is attributed to the concomitant passivation of bromide and ammonium ions on the surface of the QDs.[6,16]
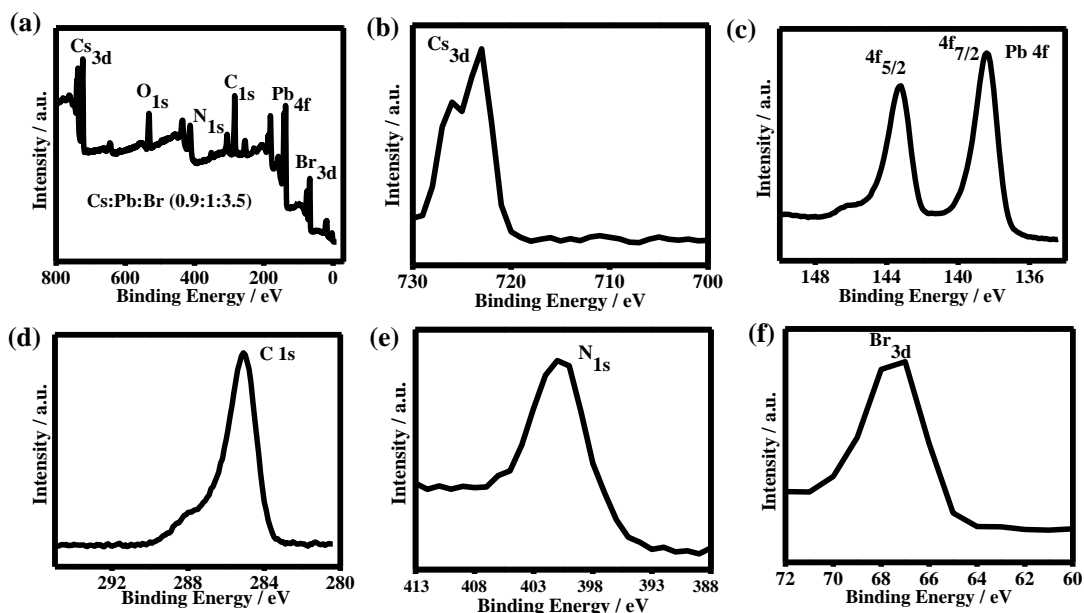
Figure 3.6: Characteristic binding energy peaks for the composition analysis of CsPbBr$_3$ QDs, (a) XPS analysis of as synthesized CsPbBr$_3$ QDs, (b) spectra of Cs 3d core level shows peak at 723.2 eV, (c) spectra of Pb 4f core level shows peak at 138.4 eV and 143.2 eV corresponding to 4f$_{5/2}$ and 4f$_{7/2}$ levels, (d) spectra of C 1s core level shows peak at 284.8 eV, (e) spectra of N 1s core level shows peak at 401.8 eV, and spectra of Br 3d core level shows peak at 67.4 eV

3.2.4. Transmission electron microscopy (TEM)

The high-resolution TEM (HRTEM) image of the QDs were shown in figure 3.7. indicates the high crystalline nature of the QDs exhibiting cubic morphology with an average edge length of 9.4±0.4 nm. The exciton Bohr radius of CsPbBr$_3$ QDs is 7 nm[17,18] and these shows that the as-synthesized QDs display in the moderate weak quantum confinement regime.[19] From the TEM images we can further revealed the uniform size-distribution of the QDs.
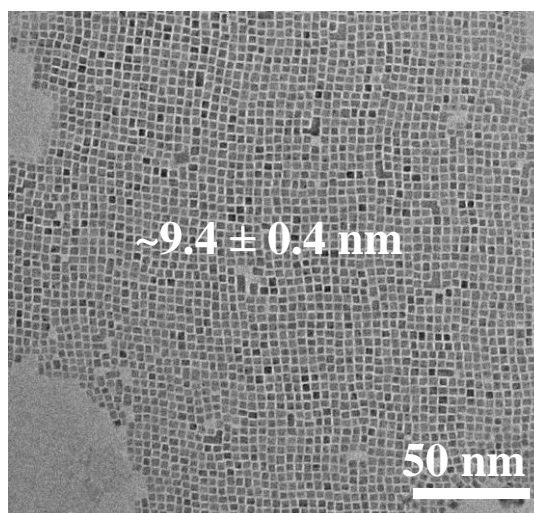
Figure 3.7: TEM images of as-prepared CsPbBr$_3$ QDs.

3.2.5. Fourier Transform Infrared Spectroscopy (FT-IR)

The FT-IR spectra of purified QDs shows (*figure 3.8*) characteristic absorption peak at 1639 cm^{-1} corresponds to the signature of protonated amine groups ($-NH_3^+$).[6,20] This feature together with the XPS results confirms the presence of bounded oleyl ammonium halide on the surface of NCs which in turn achieve long-term stability.[11,20] Furthermore, the additional peak at 1713 cm^{-1} and 1534 cm^{-1} is associated to the C=O stretching (free acid) and the surface bound oleate anions ($-COO-$) respectively.[15] The prominent peak at 1466 cm^{-1} is attributed to the bending vibration of C-H in CH$_2$ group which is described to be the integral part of the ligand.[21]
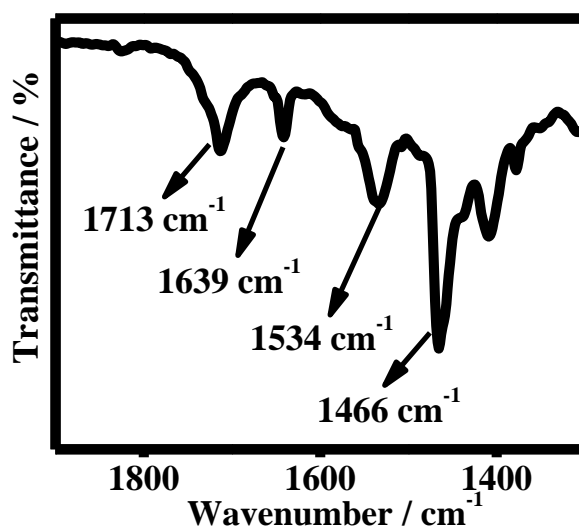
Figure 3.8: FT-IR spectra of CsPbPBr$_3$ QDs.

3.2.6. Thermogravimetric Analysis (TGA)

The TGA thermogram shown in figure 3.9 reveals that the QDs shows thermal degradation at onset temperature 500 °C. Weight loss of 4.37% at around 216-300 °C correspond to the loss of ligands present in the surface of QDs. Thus, we concluded that the 4.37% of ligands were passivated on the surface of QDs.
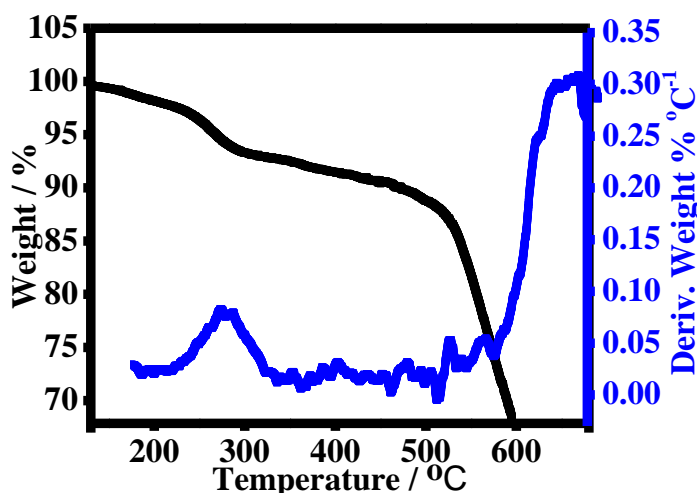
Figure 3.9: Representation of TGA graph of $CsPbBr_3$ QDs.

The derivative thermogravimetry (DTG) describe the change in weight percent per degree centigrade rise in temperature. The derivative curve (*i.e.,* blue line) increases smoothly at temperature 216 °C and gradually becomes flat at temperature 300 °C. The peak at around 290 °C shows the decomposition of surface passivated ligands whereas complete degradation at temperature above 550 °C, evident by sharp decrease of the thermogram.

3.2.7. Cyclic voltammetry measurement (CV)

The electrochemical studies of semiconductor QDs were carried out by employing CV to determine the electronic band structure *viz.* band gap energy, and band edge positions i.e., the valence band and conduction band. Precise knowledge of band structure parameters of semiconductor QDs is important for designing and developing QDs based devises.

The prepared QDs were subjected to CV experiment by dispersing it into a less polar solvents as it has tendency to degrade in other polar solvents and water.[6,22,23] We prepared 10 mL of dry 1:4 CH_3CN and toluene solution in the presence of TBAP [*t*-$Bu_4N(ClO_4)$] (0.1 M) as a supporting electrolyte[23] under inert atmospheric condition.[24]

Furthermore, the mixture of these solvent increases the dispersion ability of both QDs and TBAP. All the mixture of solvent was purged with N_2 for more than 20 min in order to avoid the interference from dissolved oxygen as it would undergoes reduction to form superoxide.[25–27] The potential window was set from +2.0 V to -2.0 V with a scan rate of 50 mVs^{-1}. The cyclic voltammogram of QDs were represented in figure 3.10. (a). The obtained cyclic voltammogram were compared with the blank sample without NCs. At first the potential is scan from 0 V towards more positive potential (anodic). At +1.26 V, a distinct anodic peak is observed labelled as A_1 in the figure 3.10. (a). From the point A_1 it is seen that there is gradual increase in current while moving towards more positive potential which may be due to the oxidation of QD.[23]
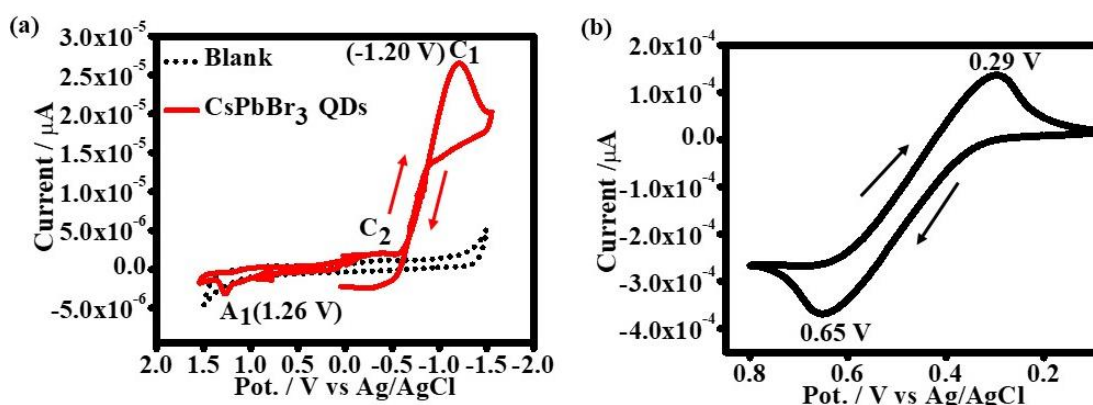
Figure 3.10: (a) Cyclic voltammograms of CsPbBr$_3$ QDs. The dotted line indicates the cyclic voltammogram of electrolyte solution without NCs, and (b) Cyclic voltammogram of ferrocene/ferrocenium redox couple used as an internal standard.

Further switching the potential towards more negative potential, a clear cathodic peak is observed at -1.20 V labelled as C_1 in figure 3.10. (a). The potential obtained for both the anodic and cathodic peak were converted to energies of HOMO and LUMO by applying ferrocene/ferrocenium redox couple as an internal standard.[25,28] The estimation can be done by applying the empirical relation;[29,30]

$$E_{HOMO} = [(E_{ox} - E_{1/2(ferrocene)}) + 4.8 \text{ eV}] \ldots\ldots\ldots\ldots \text{ (i)}$$

$$\text{or } E_{LUMO} = [(E_{red} - E_{1/2(ferrocene)}) + 4.8 \text{ eV}] \ldots\ldots\ldots\ldots \text{ (ii)}$$

Where E_{HOMO} = energy level of HOMO, E_{LUMO} = energy level of LUMO, E_{ox} = oxidation potential, E_{red} = reduction potential, and $E_{1/2(ferrocene)}$ = half wave potential of ferrocene/ferrocenium redox couple.

The formal redox potential[31] of Fc/Fc$^+$ couple (reference) *vs* Ag/AgCl in 1:4 v/v mixture of acetonitrile and toluene using 0.1 M TBAP as supporting electrolyte were measured to be 0.47 V as show in figure 3.10. (b). The value can be used for the estimation of E_{HOMO} and E_{LUMO}, thereby calculating the band gap of NCs following the general formula;

$$E_g = E_{HOMO} - E_{LUMO} \ldots\ldots\ldots\ldots \text{ (iii) where, } E_g = \text{band gap.}$$

Based upon CV results, QDs shows $E_{HOMO} = 5.56$ eV, $E_{LUMO} = 3.09$ eV and $E_g = 2.47$ eV. Thus, the electrochemical band gap between the peak A_1 (HOMO) and C_1 (LUMO) was found to be 2.47 eV which is very much in good agreement with the optical band gap of 2.45 eV as shown in figure 3.3. Here the electron transfer between the electrode interface and NCs take place from the peaks A_1 and C_1 via the VBM and CBM of QDs respectively.[23] To understand the origin of additional peak at C_2 we performed CV experiment of lead oleate and other ligands (*figure 3.11*) that have been used in synthesizing CsPbBr$_3$ QDs.
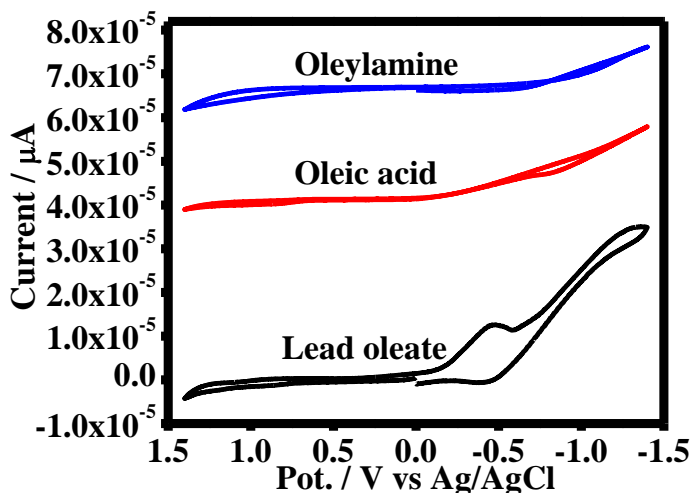
Figure 3.11: Cyclic voltammogram of oleylamine, oleic acid and lead oleate.

It is clear from the figure that the oleylamine and oleic acid does not possess any prominent peak at the set-potential window whereas lead oleate shows peak at around -0.47 V which is very much consistent to the potential at C_2 (-0.39 V). Thus, the peak near the potential at C_2 as shown in figure 3.10. (a) may be attributed to unreacted lead oleate.[23]

3.3 Conclusion

Herein, we have successfully synthesized CsPbBr$_3$ QDs at 200 °C following the previous report with some minor modification. The synthesized QDs were characterized employing UV-visible spectroscopy, PL spectroscopy, PXRD, XPS, TEM, FT-IR, CV, and TGA. The formed QDs at 200 °C were found to be stable with cubic phase. The stability of QDs is due to the passivation of bromine rich concentration and ligands on the surface of QDs as described through the FT-IR and XPS analysis. The obtained electrochemical band gap (2.47 eV) from CV experiment were in good agreement with the optical band gap (2.45 eV) obtained from UV-visible spectroscopy.

References

(1)   Yakuphanoglu, F.; Cukurovali, A.; Yilmaz, I. Refractive Index and Optical Absorption Properties of the Complexes of a Cyclobutane Containing Thiazolyl Hydrazone Ligand. *Opt. Mater.* **2005**, *27*, 1363–1368.

(2)   Zhang, M.; Zheng, Z.; Fu, Q.; Chen, Z.; He, J.; Zhang, S.; Chen, C.; Luo, W. Synthesis and Single Crystal Growth of Perovskite Semiconductor CsPbBr$_3$. *J. Cryst. Growth* **2018**, *484*, 37–42.

(3)   Su, Y.; Chen, X.; Ji, W.; Zeng, Q.; Ren, Z.; Su, Z.; Liu, L. Highly Controllable and Efficient Synthesis of Mixed-Halide CsPbX$_3$ (X = Cl, Br, I) Perovskite QDs toward the Tunability of Entire Visible Light. *ACS Appl. Mater. Interfaces* **2017**, *9*, 33020–33028.

(4)   Qaid, S. M. H.; Ghaithan, H. M.; Al-asbahi, B. A.; Alqasem, A.; Aldwayyan, A. S. Fabrication of Thin Films from Powdered Cesium Lead Bromide (CsPbBr$_3$) Perovskite Quantum Dots for Coherent Green Light Emission. *ACS Omega* **2020**, *5*, 30111–30122.

(5)   Yang, R. X.; Tan, L. Z. Understanding Size Dependence of Phase Stability and Band Gap in CsPbI$_3$ Perovskite Nanocrystals. *J. Chem. Phys.* **2020**, *152*, 34702–34707.

(6)   Thapa, S.; Bhardwaj, K.; Basel, S.; Pradhan, S.; Eling, C. J.; Adawi, A. M.; Bouillard, J. S. G.; Stasiuk, G. J.; Reiss, P.; Pariyar, A.; Tamang, S. Long-Term Ambient Air-Stable Cubic CsPbBr$_3$ Perovskite Quantum Dots Using Molecular Bromine. *Nanoscale Adv.* **2019**, *1*, 3388–3391.

(7)   Pan, J.; Quan, L. N.; Zhao, Y.; Peng, W.; Murali, B.; Sarmah, S. P.; Yuan, M.; Sinatra, L.; Alyami, N. M.; Liu, J.; Yassitepe, E.; Yang, Z.; Voznyy, O.; Comin, R.; Hedhili, M. N.; Mohammed, O. F.; Lu, Z. H.; Kim, D. H.; Sargent, E. H.; Bakr, O. M. Highly Efficient Perovskite-Quantum-Dot Light-Emitting Diodes by Surface Engineering. *Adv. Mater.* **2016**, *28*, 8718–8725.

(8)   Beal, R. E.; Slotcavage, D. J.; Leijtens, T.; Bowring, A. R.; Belisle, R. A.; Nguyen, W. H.; Burkhard, G. F.; Hoke, E. T.; McGehee, M. D. Cesium Lead Halide Perovskites with Improved Stability for Tandem Solar Cells. *J. Phys. Chem. Lett.* **2016**, *7*, 746–751.

(9)   Wang, W.; Wu, Y.; Wang, D.; Zhang, T. Effective Control of the Growth and Photoluminescence Properties of $CsPbBr_3$/Cs_4PbBr_6 Nanocomposites by Solvent Engineering. *ACS Omega* **2019**, *4*, 19641–19646.

(10)   Imran, M.; Caligiuri, V.; Wang, M.; Goldoni, L.; Prato, M.; Krahne, R.; Trizio, L. De; Manna, L. Benzoyl Halides as Alternative Precursors for the Colloidal Synthesis of Lead-Based Halide Perovskite Nanocrystals. *J. Am. Chem. Soc* **2018**, *140*, 2656–2664.

(11)   Dutta. A. Dutta.K.S, Adhikari. D.S, P. N. Chemie. *Angew. Chemie Int. Ed.* **2018**, *57*, 9083–9087.

(12)   Swarnkar, A.; Marshall, A. R.; Sanehira, E. M.; Chernomordik, B. D.; Moore, D. T.; Christians, J. A.; Chakrabarti, T.; Luther, J. M. Quantum Dot – Induced Phase Stabilization of a $CsPbI_3$ Perovskite for High-Efficiency Photovoltaics. *Science* **2016**, *354*, 92–95.

(13)   Luo, X.; Lai, R.; Li, Y.; Han, Y.; Liang, G.; Liu, X.; Ding, T.; Wang, J.; Wu, K. Triplet Energy Transfer from $CsPbBr_3$ Nanocrystals Enabled By. *J. Am. Chem. Soc* **2019**, *141*, 4186–4190.

(14)   Lee, D. C.; Jeong, S. Highly Stable Cesium Lead Halide Perovskite Nanocrystals through in Situ Lead Halide Inorganic Passivation. *Chem. Mater.* **2017**, *29*, 7088–7092.

(15)   Liu, J.; Song, K.; Shin, Y.; Liu, X.; Chen, J.; Yao, K. X.; Pan, J.; Yang, C.; Yin, J.; Xu, L.; Yang, H.; El-zohry, A. M.; Xin, B.; Mitra, S.; Hedhili, M. N.; Roqan, I. S.; Mohammed, O. F.; Han, Y.; Bakr, O. M. Light-Induced Self-Assembly of Cubic $CsPbBr_3$ Perovskite Nanocrystals into Nanowires. *Chem. Mater* **2019**, *31*, 6642–6649.

(16)   Ravi, V. K.; Santra, P. K.; Joshi, N.; Chugh, J.; Singh, S. K.; Ghosh, P.; Nag, A.

Origin of the Substitution Mechanism for the Binding of Organic Ligands on the Surface of CsPbBr$_3$ Perovskite Nanocubes. *J. Phys. Chem. Lett.* **2017**, *8*, 4988–4994.

(17) Worku, M.; Tian, Y.; Zhou, C.; Lin, H.; Chaaban, M.; Xu, L.; He, Q.; Beery, D.; Zhou, Y.; Lin, X.; Su, Y. feng; Xin, Y.; Ma, B. Hollow Metal Halide Perovskite Nanocrystals with Efficient Blue Emissions. *Sci. Adv.* **2019**, *6*, 1–9.

(18) Aldakov, D.; Reiss, P. Safer-by-Design Fluorescent Nanocrystals: Metal Halide Perovskites vs Semiconductor Quantum Dots. *J. Phys. Chem. C* **2019**, *123*, 12527–12541.

(19) Butkus, J.; Vashishtha, P.; Chen, K.; Gallaher, J. K.; Prasad, S. K. K.; Metin, D. Z.; Gaston, N.; Halpert, J. E.; Hodgkiss, J. M. The Evolution of Quantum Confinement in CsPbBr$_3$ Perovskite Nanocrystals. *Chem. Mater.* **2017**, *29*, 3644–3652.

(20) Yoo, D.; Woo, J. Y.; Kim, Y.; Kim, S. W.; Wei, S.; Jeong, S.; Kim, Y. Origin of the Stability and Transition from Anionic to Cationic Surface Ligand Passivation of All-Inorganic Cesium Lead Halide Perovskite Nanocrystals. *J. Phys. Chem. Lett* **2020**, *11*, 652–658.

(21) Pan, A.; He, B.; Fan, X.; Liu, Z.; Urban, J. J.; Alivisatos, A. P.; He, L.; Liu, Y. Insight into the Ligand-Mediated Synthesis of Colloidal CsPbBr$_3$ Perovskite Nanocrystals: The Role of Organic Acid, Base, and Cesium Precursors. *ACS Nano* **2016**, *10*, 7943–7954.

(22) Koh, T. M.; Shanmugam, V.; Guo, X.; Lim, S. S.; Filonik, O.; Herzig, E. M.; Müller-Buschbaum, P.; Swamy, V.; Chien, S. T.; Mhaisalkar, S. G.; Mathews, N. Enhancing Moisture Tolerance in Efficient Hybrid 3D/2D Perovskite Photovoltaics. *J. Mater. Chem. A* **2018**, *6*, 2122–2128.

(23) Ravi, V. K.; Markad, G. B.; Nag, A. Band Edge Energies and Excitonic Transition Probabilities of Colloidal CsPbX$_3$ (X = Cl, Br, I) Perovskite Nanocrystals. *ACS Energy Lett.* **2016**, *1*, 665–671.

(24) Inamdar, S. N.; Ingole, P. P.; Haram, S. K. Determination of Band Structure Parameters and the Quasi-Particle Gap of CdSe Quantum Dots by Cyclic Voltammetry. *ChemPhysChem* **2008**, *9*, 2574–2579.

(25) Elgrishi, N.; Rountree, K. J.; McCarthy, B. D.; Rountree, E. S.; Eisenhart, T. T.; Dempsey, J. L. A Practical Beginner's Guide to Cyclic Voltammetry. *J. Chem. Educ.* **2018**, *95*, 197–206.

(26)   Jalilov, A. S.; Zhang, C.; Samuel, E. L. G.; Sikkema, W. K. A.; Wu, G.; Berka, V.; Kent, T. A.; Tsai, A. L.; Tour, J. M. Mechanistic Study of the Conversion of Superoxide to Oxygen and Hydrogen Peroxide in Carbon Nanoparticles. *ACS Appl. Mater. Interfaces* **2016**, *8*, 15086–15092.

(27)   Hayyan, M.; Hashim, M. A.; Alnashef, I. M. Superoxide Ion: Generation and Chemical Implications. *Chem. Rev.* **2016**, *116*, 3029–3085.

(28)   Gagne, R. R.; Koval, C. A.; Lisensky, G. C. Ferrocene as an Internal Standard for Electrochemical Measurements. *Inorg. Chem.* **1980**, *19*, 2854–2855.

(29)   Shafiee, A.; Salleh, M. M.; Yahana, M. Determination of HOMO and LUMO of [6, 6]-Phenyl C61-Butyric Acid through Voltametry Characterization. *Sains Malaysiana* **2011**, *40*, 173–176.

(30)   Leonat, L.; Sbarcea, G.; Branzoi, I. V. Cyclic Voltammetry For Energy Levels Estimation Of Organic Materials. *U.P.B. Sci. Bull* **2013**, *75*, 1454–2331.

(31)   Lewandowski, A.; Waligora, L.; Galinski, M. Ferrocene as a Reference Redox Couple for Aprotic Ionic Liquids. *Electroanalysis* **2009**, *21*, 2221–2227.

CHAPTER IV

TUNING BAND GAP IN COLLOIDAL CsPbBr$_3$ QDs

CHAPTER IV
TUNING BAND GAP IN COLLOIDAL CsPbBr₃ QDs

4.1. Introduction

The band gap tunability in colloidal $CsPbBr_3$ QDs is an important property and has far-reaching implication in the field of optoelectronics. The tunability in $CsPbBr_3$ QDs can be achieved either through change in composition of the materials or simply by tuning the size of the QDs. The first section (4.2) of this chapter focuses on the synthesis of colloidal $CsPbBr_3$ QDs where the size of the QDs are effectively tuned by changing the reaction temperature.[1–4] To our knowledge, electrochemical studies on different sized $CsPbBr_3$ QDs has not been reported, mainly because of the lack of methods to precisely control the size of the NCs. However, the electrochemical studies on lead halide perovskite containing different halides have been reported. In the second section (4.3), we show a strong correlation between the electrochemical band and the optical band gap of $CsPbBr_3$ NCs of different sizes. The third section (4.4) is focussed on the effect of capping ligands on band edge alignment and optical properties of $CsPbBr_3$ QDs by varying the different capping ligands *viz.* alkyl amine and carboxylic acid at elevated temperature.

4.2. Synthesis of CsPbBr₃ QDs at different temperature and the role of reaction temperature towards size and optical properties

In order to understand the role of temperature on the size and its subsequent influence toward band edge, we synthesized $CsPbBr_3$ QDs at different temperature. The reaction injection temperature plays a dynamic role during the process of synthesizing colloidal $CsPbBr_3$ QDs.[3,5] There are numerous reports wherein the optical properties of $CsPbBr_3$ QDs were tuned by changing composition *via* halide exchange reaction.[6–10] Herein, we tuned the size of the QDs by changing the reaction temperature.[3,4] The $CsPbBr_3$ QDs were synthesized at four different temperatures 160, 170, 200, and 220 °C to obtain different sized QDs (~7-16 nm) marked as QD1, QD2, QD3 and QD4 respectively. Typically, cesium oleate precursor were injected into the hot reaction mixture containing lead and halide precursors stabilised by oleyl amine and oleic acid. Figure 4.1. (a) and (b) shows the UV-visible absorption and photoluminescence (PL) spectra

of CsPbBr$_3$ QDs synthesized at different temperatures. Increasing the size of NCs from ~7.2 ± 0.5 to ~15.7 ± 0.7 (*figure 4.2*) led to a slight red-shift of the absorption and emission maximum. Conversely, with the decrease in the size of NCs the wavelength of absorption and emission maximum spectra shortens and move slightly towards the blue end of the visible electromagnetic spectrum.[9] This characteristic property is generally attributed to the size quantum confinement effect of CsPbBr$_3$ QDs.[11–15] Furthermore, the distinct absorption signature and symmetrical and narrow emission spectra (*figure 4.1*) indicate the narrow size distribution of the QDs.[16]
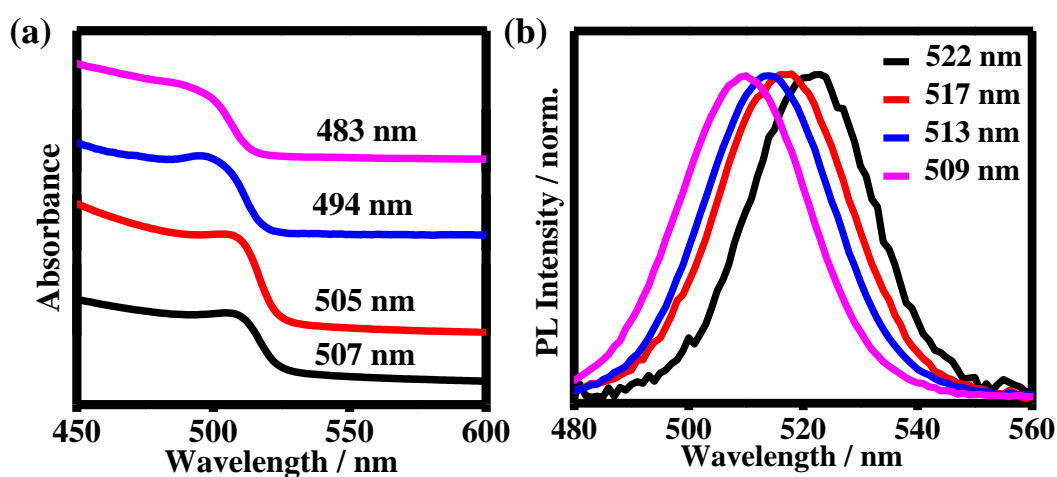
Figure 4.1: (a) UV-visible absorption and CsPbBr$_3$ QDs size-dependent optical band gap. (b) Corresponding PL emission spectra. Excitation wavelength: 400 nm

Increasing the reaction temperature (160-220 °C), the size of the QDs increases and *vice-versa* which is attributed to relative rate of nucleation and growth of nanocrystals occurred at different reaction temperature.[17] The optical band gap calculated from the absorption spectra (*figure 4.2. a, c, e and g*) were found to be decreases with increasing temperature (increasing size). The optical band gap for CsPbBr$_3$ QDs synthesized at 160, 170, 200, and 220 °C were calculated to be 2.56, 2.51, 2.45. and 2.44 eV respectively. The as-prepared CsPbBr$_3$ QDs were monodispersed as examined by HRTEM image. With the increase in reaction temperature the edge length of CsPbBr$_3$ QDs gradually increases from ~7.2 ± 0.5 to ~15.7 ± 0.7 nm for the smallest and largest nanocrystals respectively as demonstrated by TEM studies (*figure 4.2. b, d, f and h*) which is in the moderate to weak quantum confinement regime.[11]
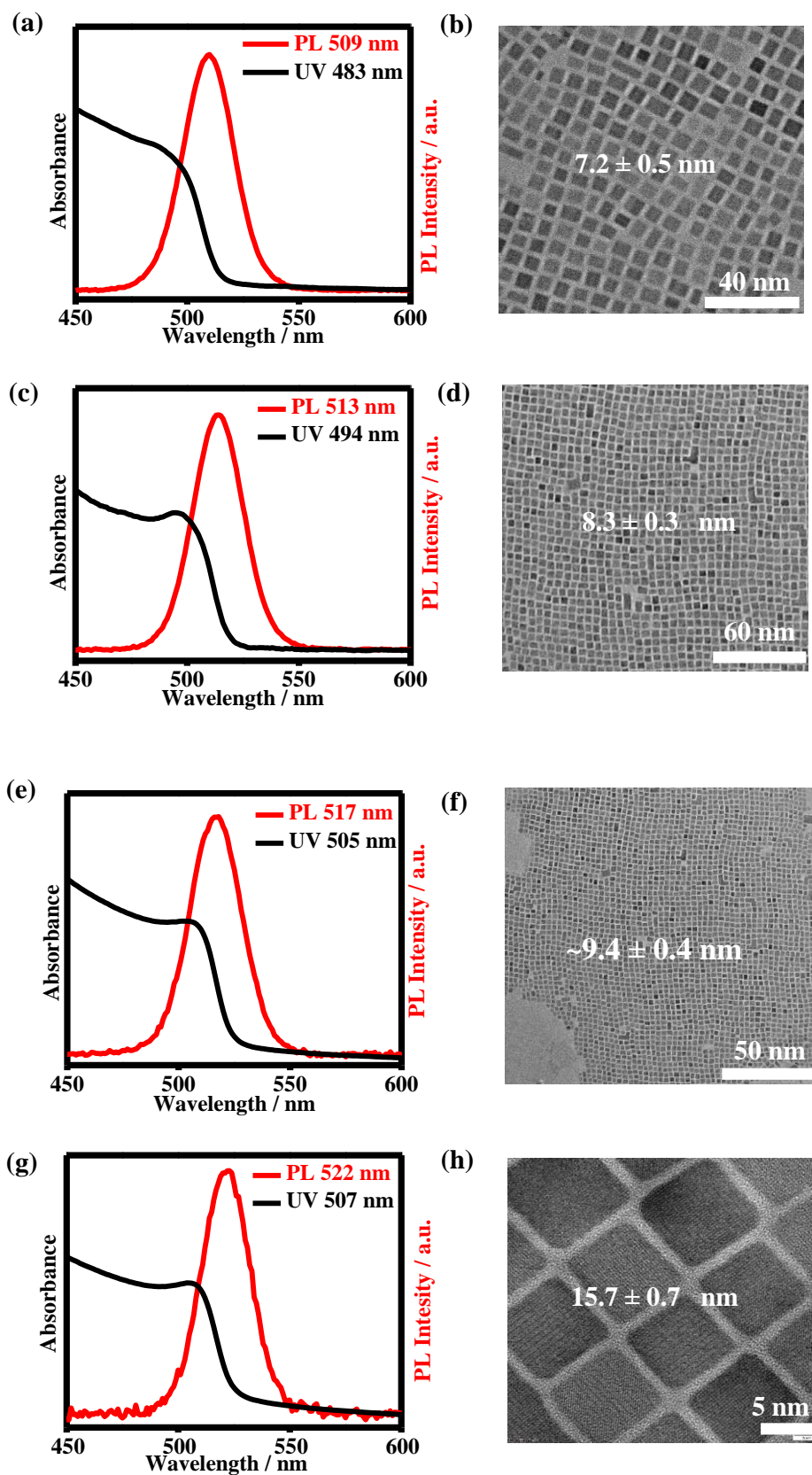
Figure 4.2: UV-vis absorption and PL spectra (excited at 400 nm) of QD1, QD2, QD3, and QD4 at (a)160 ℃, (c) 170 ℃, (e) 200 ℃ and (g) 220 ℃ and its corresponding TEM images were represented by (b), (d), (f), and (h) respectively.

4.3. Role of size towards band-edge alignment

Size-dependent optical properties of QDs have tremendous implication in their application in optoelectronics.[18–21] Due to the quantum confinement effect, VBM and CBM of the QDs change with change in size.[10] The exact position of VBM and CBM of QDs is important for design of optoelectronic devices. The VBM and CBM energy levels are typically determined using UV photoelectron spectroscopy.[10,22,23] The alternative method is by using cyclic voltammetry (CV). However, CV technique is more challenging due to instability of the QDs, the presence of insulating ligands on the surface of the QDs, poor conductivity and lack of appropriate solvent/electrolyte system for colloidal QDs. Furthermore, the absence of data on effect of size on electrochemical band gap of cesium lead halide perovskite is attributed to lack of synthetic methods to precisely control the size. The cyclic voltammogram of different size of QDs are illustrated in the figure 4.3. (a)-(d).
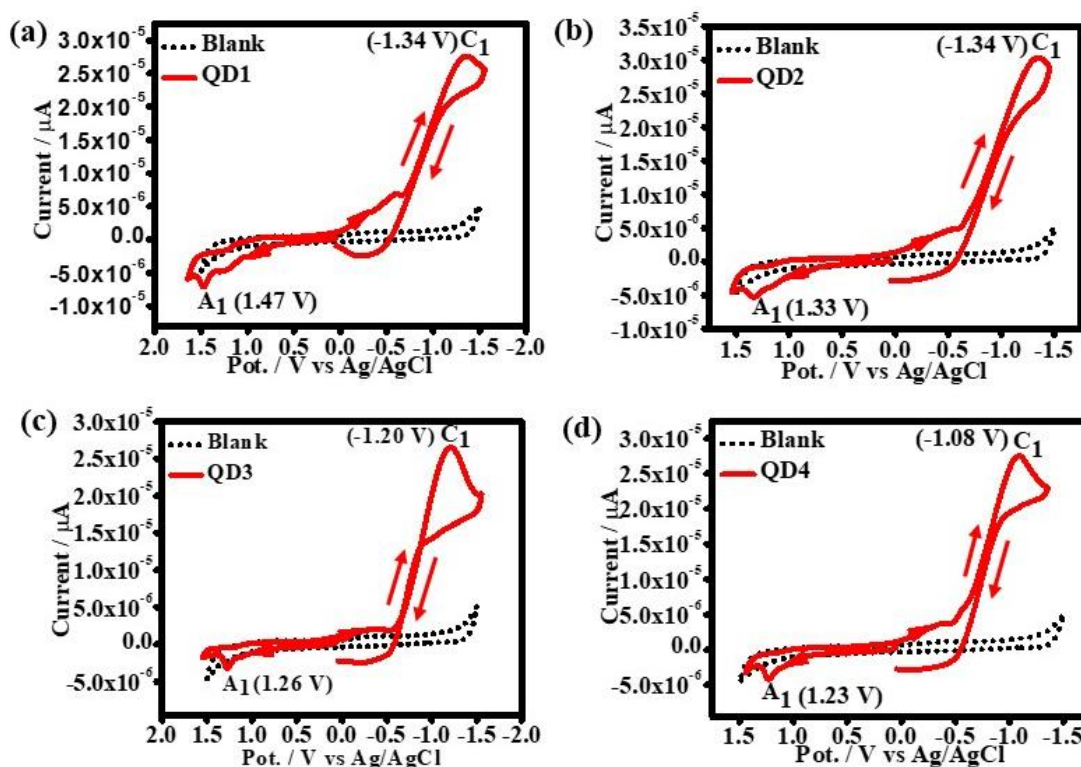
Figure 4.3: Cyclic voltammogram of as-synthesized CsPbBr$_3$ QDs at different temperature (a) 160 °C (QD1), (b) 170 °C (QD2), (c) 200 °C (QD3), and (d) 220 °C (QD4)

Figure 4.4. (a) and (b) show a systematic shift in VBM and CBM and their respective band gap with the increase in the size of QDs. This is consistent with the "particle in a box" model, Brus proposed to explain the dependence of redox potential on particle

size for Q-CdS.[24] VBM shifts towards less positive potential and the CBM shift towards less negative potential and the reverse is true when size of the QDs in decreased. QD1 having smaller size exhibit large electrochemical band gap as compared to QD4 having larger size. The comparative study of the energy levels (HOMO and LUMO) of different size of QDs as extracted from their CV curve were presented in the tabular form (Table 4.1). The energy level obtained from the electrochemical study (CV) is in good agreement with optical data.
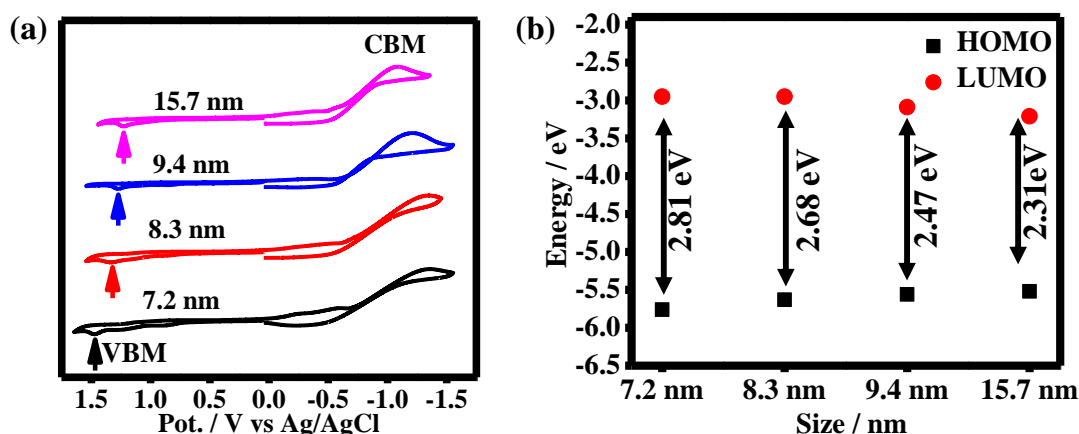
Figure 4.4: (a) Comparative band edge alignment of different size of QDs, and (b) its corresponding influence towards band edge position.

Table 4.1: UV, PL, electrochemical band gap, optical band gap and FWHM of as-prepared different size of QDs.

Sample	T/ °C	UV / nm	PL / nm	size / nm	Electrochemical band gap / eV	Optical band gap / eV	FWHM / nm
QD1	160	483	509	7.2±0.5	2.81	2.56	26
QD2	170	494	513	8.3±0.3	2.68	2.51	25
QD3	200	505	517	9.4±0.4	2.47	2.45	28
QD4	220	507	522	15.7±0.7	2.31	2.44	25

4.4. Role of capping ligands towards band-edge alignment and optical properties

Another important aspect of our investigation is to understand the role of different capping ligands over band-edge position and their corresponding influence on optical properties.[5,14,25–27] To elucidate the effect of capping ligands we chose different alkyl

amine [such as oleylamine (OAm), stearylamine (SAm), and dodecylamine (DAm)] and carboxylic acid [such as oleic acid (OA), stearic acid (SA) and myristic acid (MA)] for the synthesis of $CsPbBr_3$ QDs following the same reaction procedure. In one series of experiments, we have fixed the concentration of oleic acid thereby adding different alkyl amine and all the reaction was performed at 170 °C. The reaction scheme for the synthesis of QDs were shown in figure 4.5.

Scheme I: Synthesis of $CsPbBr_3$ QDs using various alkylamine.

Scheme II: Synthesis of $CsPbBr_3$ QDs using various carboxylic acid.
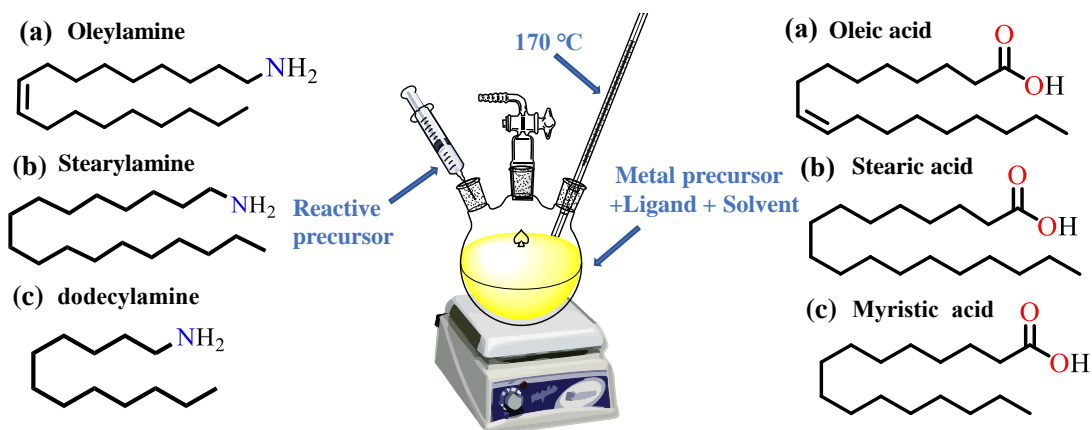
Figure 4.5: Representation of preparation of $CsPbBr_3$ QDs with various capping ligands.

The motive for the synthesis of $CsPbBr_3$ QDs with different ligands was to understand the effect of ligands over band edge position. All the reaction were performed at optimized reaction temperature at 170 °C. Above this temperature the precipitation of nanocrystal will occurs with DA, SAm, MA, and SA. The formed QDs were characterized using the UV-vis absorption and PL spectroscopy and is demonstrated in the figure 4.6.
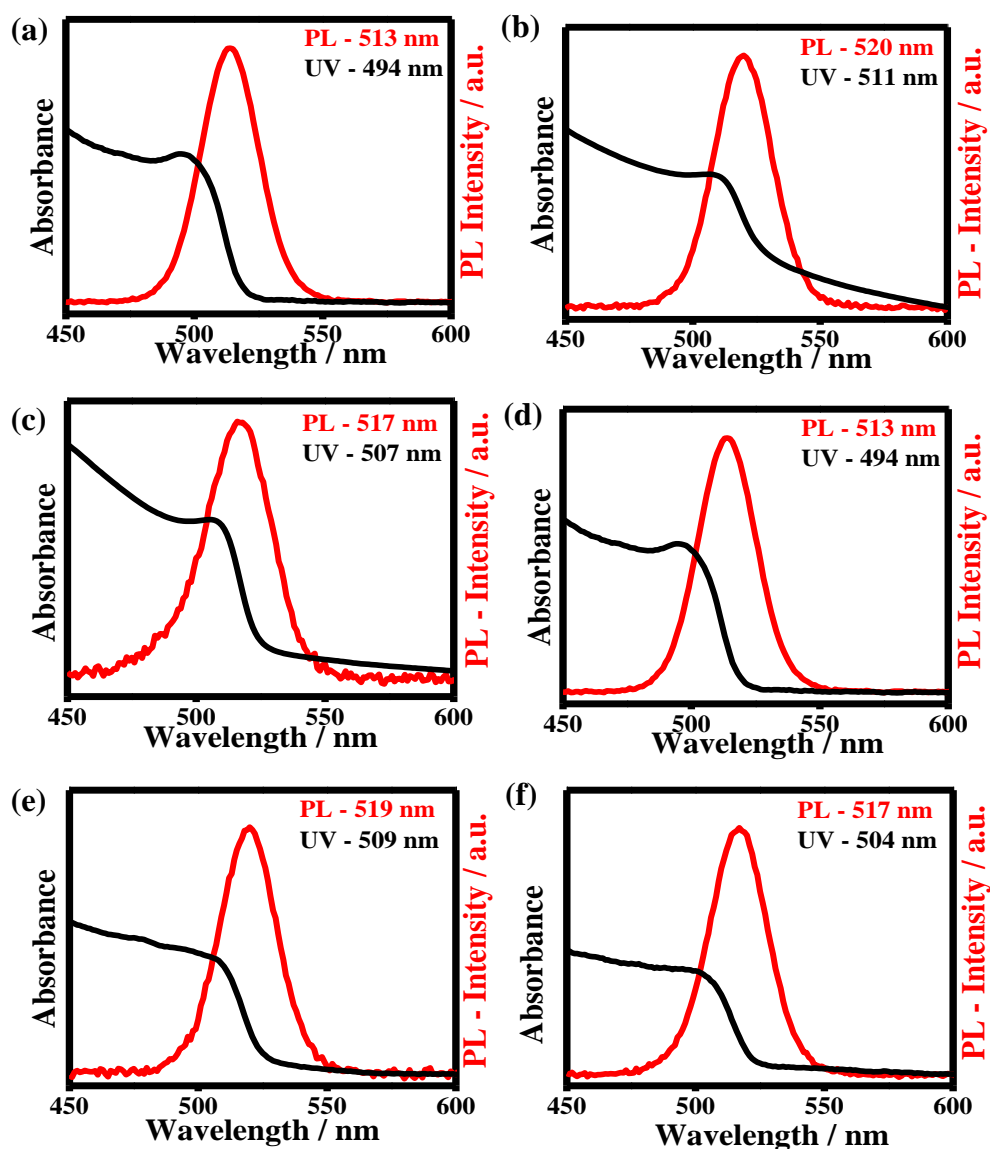
Figure 4.6: UV-vis absorption and PL spectra (excited at 400 nm) of as-prepared CsPbBr₃ QDs with (a) OAm, (b) DAm, (c) SAm, (d) OA, (e) MA, and (f) SA.

It was observed that by varying the chain length of alkyl amine the optical properties of QDs can be tuned over the entire visible region. Herein, CsPbBr₃ QDs capped with DAm (DAm having 12 carbon chain length) shows absorption/emission maximum spectra towards the red end of the visible electromagnetic spectrum whereas OAm and SAm capped QDs (OAm/SAm having 18 carbon chain length) having similar chain length shows absorption/emission maximum spectra towards the blue end of the visible electromagnetic spectrum (*figure 4.7*). Thus, by varying the chain length of alkyl amine, one can tune the optical properties of QDs.
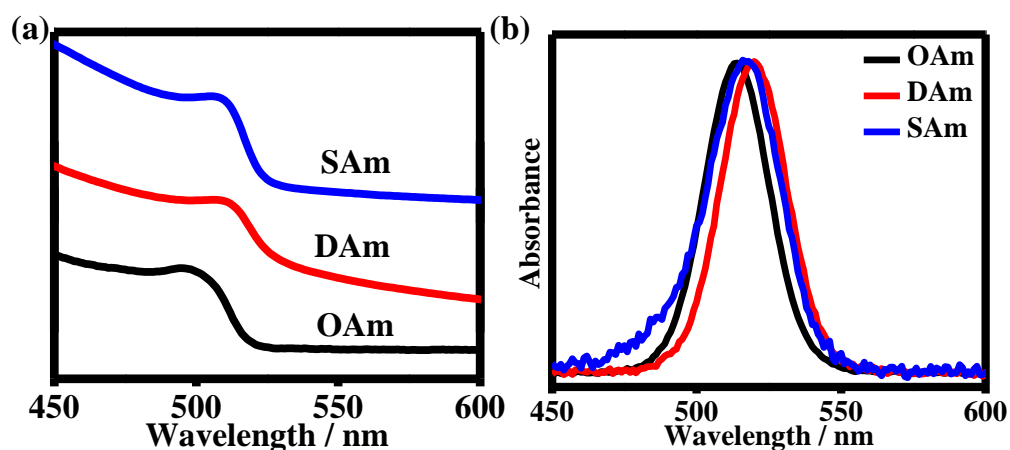
Figure 4.7: Tunable (a)UV-visible absorption, and (b)PL spectra of CsPbBr₃ QDs (excited at 400 nm) that are coated with OAm, SAm, and DAm respectively.

Furthermore, to have precise knowledge about the effect of various alkylamines on the band-edge position we have performed a CV experiment. Figure 4.8 (a) demonstrates the cyclic voltammogram of different alkylamine. It was observed that with alkylamine having a shorter chain length (DAm = 2.59 eV) the band edge position shift towards less positive and negative potential as compared to alkylamine having a longer chain length (OAm = 2.68 eV and SAm = 3.07 eV). Thus, tuning of band gap is evident where with the decrease in the chain length of the alkyl amine, the band-gap decrease and *vice-versa* as shown in the figure 4.8.(b).
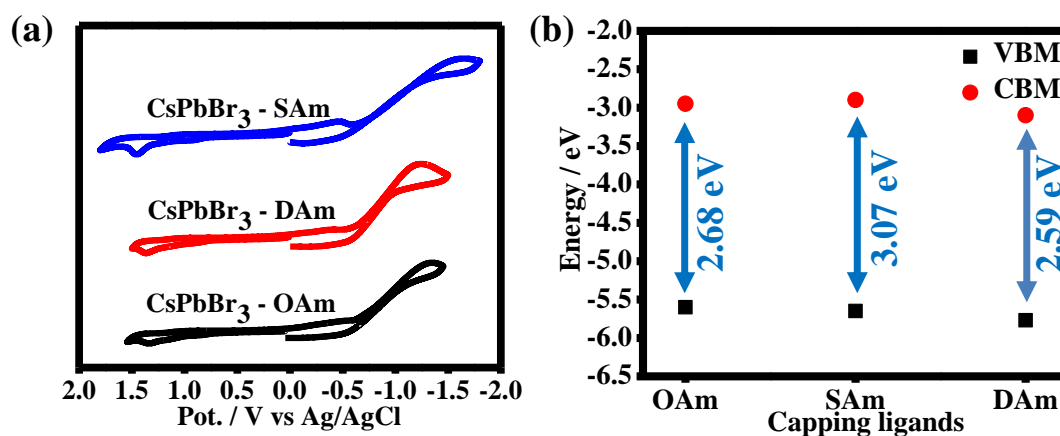
Figure 4.8: Representation of (a) cyclic voltammogram, and (b) tunable band-gap of as-synthesized CsPbBr₃ QDs that are coated with OAm, SAm, and DAm respectively.

In another series of experiments, keeping all other condition same, we fixed the concentration of oleylamine and varied carboxylic acid. We noted that by changing the chain length of carboxylic acids such as myristic acid (MA - C16), oleic acid (OA -

C18) and stearic acid (SA - C18) the band-edge position (*figure 4.9.b*) was found to be 2.53, 2.68, and 2.75 respectively.
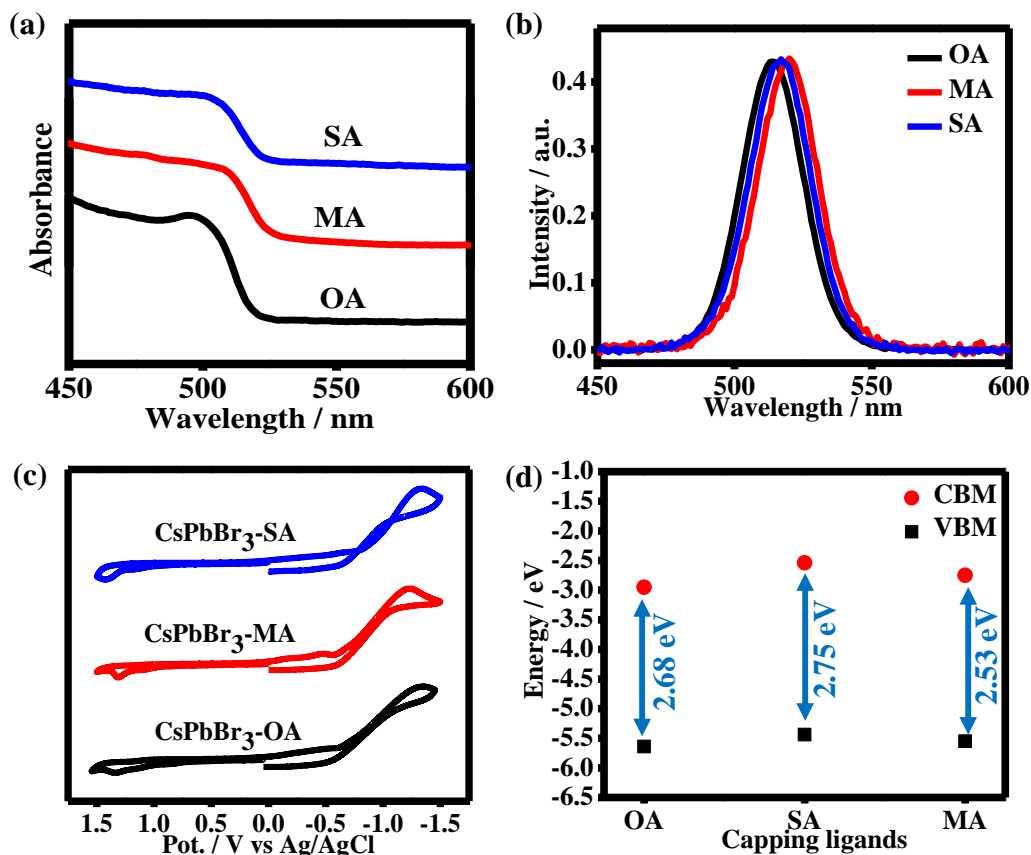
Figure 4.9: (a) UV-visible absorption spectra, (b) PL emission spectra (excited at 400 nm) (c) cyclic voltammogram, and (d) band-gap of as-synthesized CsPbBr$_3$ QDs that are coated with OA, SA, and MA respectively.

The comparative study of band-edge position, optical and electrochemical band-gap values of different alkylamine and carboxylic acid were demonstrated in the tabular form (Table 4.2). It is evident from the table 4.2 that by decreasing the chain length of carboxylic acid the size of QDs increases resulting in the decrease in band gap position. Thus, by decreasing the chain length of carboxylic acid we were able to tune the optical and electrochemical band gap. Similar results were also obtained by Pan *et.al.,* by performing the reaction at high temperature (170 °C) where the size of CsPbBr$_3$ QDs changes from 9.5 to 13 nm by decreasing the chain length of carboxylic acid.[5]

Table 4.2: Comparative study of effect of ligands over band edge alignment:

Capping Ligands	λ_{ab} / nm	λ_{em} / nm	E_{ox}^{onset} pot. vs Ag/AgCl / V	HOMO level / eV	E_{red}^{onset} pot. vs Ag/AgCl / V	LUMO level / eV	E_g [from CV / eV]	Optical E_g / eV
OAm	494	513	1.34	5.67	-1.34	2.99	**2.68**	**2.51**
SAm	507	517	1.45	5.78	-1.62	2.71	**3.07**	**2.44**
DAm	511	520	1.36	5.69	-1.23	3.10	**2.59**	**2.42**
OA	494	513	1.34	5.67	-1.34	2.99	**2.68**	**2.51**
SA	504	517	1.42	5.75	-1.33	3.00	**2.75**	**2.46**
MA	509	519	1.31	5.64	-1.22	3.11	**2.53**	**2.43**

4.5. Conclusion

The colloidal CsPbBr$_3$ QDs of varying size were synthesized at different optimized reaction temperature. The increase in temperature from 160 to 220 °C leads to increase in the size of QDs as a result, we were able to tune the optical and electrochemical band gap position. The obtained optical and electrochemical band gap position were found to be in good agreement. Furthermore, we synthesized CsPbBr$_3$ QDs exploiting different capping ligands and performed optical and electrochemical investigation in order to understand the effect of capping ligand over band edge position. It was found that with the increase in the chain length of carboxylic acid (or alkyl amine), the size of the QDs decreases resulting in the increase in band gap.

References:

(1)   Akkerman, Q. A.; Martínez-Sarti, L.; Goldoni, L.; Imran, M.; Baranov, D.; Bolink, H. J.; Palazon, F.; Manna, L. Molecular Iodine for a General Synthesis of Binary and Ternary Inorganic and Hybrid Organic-Inorganic Iodide Nanocrystals. *Chem. Mater.* **2018**, *30*, 6915–6921.

(2)   Sun, H.; Li, Z.; Kong, L.; Wang, B.; Zhang, C.; Yuan, Q.; Huang, S.; Liu, Y.;

Li, L. Enhancing the Stability of CsPbBr$_3$ Nanocrystals by Sequential Surface Adsorption of S^{2-} and Metal Ions. *Chem. Commun.* **2018**, *54*, 9345–9348.

(3)   Imran, M.; Caligiuri, V.; Wang, M.; Goldoni, L.; Prato, M.; Krahne, R.; De Trizio, L.; Manna, L. Benzoyl Halides as Alternative Precursors for the Colloidal Synthesis of Lead-Based Halide Perovskite Nanocrystals. *J. Am. Chem. Soc.* **2018**, *140*, 2656–2664.

(4)   Thapa, S.; Bhardwaj, K.; Basel, S.; Pradhan, S.; Eling, C. J.; Adawi, A. M.; Bouillard, J. S. G.; Stasiuk, G. J.; Reiss, P.; Pariyar, A.; Tamang, S. Long-Term Ambient Air-Stable Cubic CsPbBr$_3$ Perovskite Quantum Dots Using Molecular Bromine. *Nanoscale Adv.* **2019**, *1*, 3388–3391.

(5)   Shamsi, J.; Urban, A. S.; Imran, M.; De Trizio, L.; Manna, L. Metal Halide Perovskite Nanocrystals: Synthesis, Post-Synthesis Modifications, and Their Optical Properties. *Chem. Rev.* **2019**, *119*, 3296–3348.

(6)   Guhrenz, C.; Benad, A.; Ziegler, C.; Haubold, D.; Gaponik, N.; Eychmüller, A. Solid-State Anion Exchange Reactions for Color Tuning of CsPbX$_3$ Perovskite Nanocrystals. *Chem. Mater.* **2016**, *28*, 9033–9040.

(7)   Parobek, D.; Dong, Y.; Qiao, T.; Rossi, D.; Son, D. H. Photoinduced Anion Exchange in Cesium Lead Halide Perovskite Nanocrystals. *J. Am. Chem. Soc.* **2017**, *139*, 4358–4361.

(8)   Akkerman, Q. A.; Innocenzo, V. D.; Accornero, S.; Scarpellini, A.; Petrozza, A.; Prato, M.; Manna, L. Tuning the Optical Properties of Cesium Lead Halide Perovskite. *J. Am. Chem. Soc.* **2015**, *137*, 10276–10281.

(9)   Protesescu, L.; Yakunin, S.; Bodnarchuk, M. I.; Krieg, F.; Caputo, R.; Hendon, C. H.; Yang, R. X.; Walsh, A.; Kovalenko, M. V. Nanocrystals of Cesium Lead Halide Perovskites (CsPbX$_3$, X = Cl, Br, and I): Novel Optoelectronic Materials Showing Bright Emission with Wide Color Gamut. *Nano Lett.* **2015**, *15*, 3692–3696.

(10)   Ravi, V. K.; Markad, G. B.; Nag, A. Band Edge Energies and Excitonic Transition Probabilities of Colloidal CsPbX$_3$ (X = Cl, Br, I) Perovskite Nanocrystals. *ACS Energy Lett.* **2016**, *1*, 665–671.

(11)   Butkus, J.; Vashishtha, P.; Chen, K.; Gallaher, J. K.; Prasad, S. K. K.; Metin, D. Z.; Gaston, N.; Halpert, J. E.; Hodgkiss, J. M. The Evolution of Quantum Confinement in CsPbBr$_3$ Perovskite Nanocrystals. *Chem. Mater.* **2017**, *29*, 3644–3652.

(12)   Zorman, B. Quantum Confinement Effects in CdSe Quantum Dots. *J. Phys. Chem* **1995**, *99*, 7649–7653.

(13)   Yang, R. X.; Tan, L. Z. Understanding Size Dependence of Phase Stability and Band Gap in CsPbI$_3$ Perovskite Nanocrystals. *J. Chem. Phys.* **2020**, *152*, 34702–34707.

(14)   Querner, C.; Reiss, P.; Sadki, S.; Zagorska, M.; Pron, A. Size and Ligand Effects on the Electrochemical and Spectroelectrochemical Responses of CdSe Nanocrystals. *Phys.Chem.Chem. Phys* **2005**, *7*, 3204 –3209.

(15)   Haram, S. K.; Quinn, B. M.; Bard, A. J. Electrochemistry of CdS Nanoparticles : A Correlation between Optical and Electrochemical Band Gaps. *J. Am. Chem. Soc.* **2001**, *123*, 8860–8861.

(16)   Zhang, M.; Zheng, Z.; Fu, Q.; Chen, Z.; He, J.; Zhang, S.; Chen, C.; Luo, W. Synthesis and Single Crystal Growth of Perovskite Semiconductor CsPbBr$_3$. *J. Cryst. Growth* **2018**, *484*, 37–42.

(17)   Chen, S.; Zhang, X.; Zhao, Y.; Zhang, Q. Effects of Reaction Temperature on Size and Optical Properties of CdSe Nanocrystals. *Bull. Mater. Sci.* **2010**, *33*, 547–552.

(18)   Inamdar, S. N.; Ingole, P. P.; Haram, S. K. Determination of Band Structure Parameters and the Quasi-Particle Gap of CdSe Quantum Dots by Cyclic Voltammetry. *ChemPhysChem* **2008**, *9*, 2574–2579.

(19)   Jasieniak, J.; Califano, M.; Watkins, S. E. Size-Dependent Valence and Conduction Band-Edge Energies of Semiconductor Nanocrystals. *ACS Nano* **2011**, *5*, 5888–5902.

(20)   Shao, Q.; Lin, H.; Shao, M. Determining Locations of Conduction Bands and Valence Bands of Semiconductor Nanoparticles Based on Their Band Gaps. *ACS Omega* **2020**, *5*, 10297–10300.

(21)   Smith, A. M.; Nie, S. Semiconductor Nanocrystals: Structure, Properties, and Band Gap Engineering. *Acc. Chem. Res.* **2010**, *43*, 190–200.

(22)   Schulz, P.; Edri, E.; Kirmayer, S.; Hodes, G.; Cahen, D.; Kahn, A. Interface Energetics in Organo-Metal Halide Perovskite-Based Photovoltaic Cells. *Energy Environ. Sci.* **2014**, *7*, 1377–1381.

(23)   Ryu, S.; Noh, J. H.; Jeon, N. J.; Chan Kim, Y.; Yang, W. S.; Seo, J.; Seok, S. Il. Voltage Output of Efficient Perovskite Solar Cells with High Open-Circuit Voltage and Fill Factor. *Energy Environ. Sci.* **2014**, *7*, 2614–2618.

(24)   Brus, L. E. Electron – Electron and Electronhole Interactions in Small Semiconductor Crystallites : The Size Dependence of the Lowest Excited Electronic State Electron-Electron and Electron-Hole Interactions in Small Semiconductor Crystallites : The Size Dependence O. *J. Chem. Phys.* **1984**, *80*, 4403–4409.

(25)   Liu, J.; Yang, W.; Li, Y.; Fan, L.; Li, Y. Electrochemical Studies of the Effects of the Size, Ligand and Composition on the Band Structures of CdSe, CdTe and Their Alloy Nanocrystals. *Phys. Chem. Chem. Phys.* **2014**, *16*, 4778–4788.

(26)   Amelia, M.; Impellizzeri, S.; Monaco, S.; Yildiz, I.; Silvi, S.; Raymo, F. M.; Credi, A. Structural and Size Effects on the Spectroscopic and Redox Properties of Cdse Nanocrystals in Solution: The Role of Defect States. *ChemPhysChem* **2011**, *12*, 2280–2288.

(27)   Garcia-gutierrez, D. F.; Hernandez-casillas, L. P.; Cappellari, M. V.; Fungo, F.; Mart, E.; Ixcoatl, D. Influence of the Capping Ligand on the Band Gap and Electronic Levels of PbS Nanoparticles through Surface Atomistic Arrangement Determination. *ACS Omega* **2018**, *3*, 393–405.

CHAPTER V

APPLICATION OF BAND GAP ENGINEERING OF COLLOIDAL CsPbBr$_3$ QDs IN PHOTOCATALYSIS

CHAPTER V

APPLICATION OF BAND GAP ENGINEERING OF COLLOIDAL CsPbBr₃ QDs IN PHOTOCATALYSIS

5.1 Introduction

Lead halide perovskites (LHPs) nanocrystals have attracted a lot of attention in the last few years owing to their potential application in photovoltaics and other optoelectronic devices.[1–5] This novel class of materials exhibiting defect-free photoluminescence (PL) with exceptional photophysical properties are equally favourable for photocatalysis.[6] In Photocatalysis, the light absorption, charge separation, and transfer are pivotal for activating organic substrate in photoredox catalysis.[7] Such reactions rely on the nature of the band-edge position of catalyst with respect to the substrate.

5.2 Photocatalytic oxidative aromatization of Hantzsch ester using different sized CsPbBr₃ QDs.

To assess the applicability of as-prepared QDs in photocatalysis we performed aromatization of Hantzsch ester *i.e.*, diethyl 2,6-dimethyl-1,4-dihydropyridine-3,5-dicarboxylate [**1a**, (1,4-DHP)] as the model substrate due to its synthetic accessibility. Furthermore, it is a well known NAD(P)H-type model for redox processes based on the dihydropyridine skeleton[8–10] and is widely used for curing cardiovascular diseases and popularly known as calcium channel blockers in pharmacology.[11,12] We examined the photocatalytic efficiency of as-prepared four different sizes of QDs such as QD1, QD2, QD3, and QD4 synthesized at 160, 170, 200, and 220 $^{\circ}$C respectively (*Cf. Chapter IV*). In order to understand the catalytic efficiency of these QDs we performed the kinetic studies of oxidative aromatization of 1,4-DHP. The kinetic studies was performed by monitoring the progress of reaction using UV-visible absorption spectroscopy. The characteristic peak of aromatized proudct is at 339 nm. Figure 5.1 shows the kinetic data of the experiments performed with different QDs and also control experiments. The reaction was found to be pseudo-first order reaction and the rate of the reaction was calculated   by plotting $\ln(C_t/C_0)$ with reaction time. In absence of catalyst, the reaction is very slow (k = 0.037 ms^{-1}). Even after 5 h of reaction only trace amount of proudct is detected. In presence of the catalyst QD1 (size: 7.25±0.5 nm) the

rate is increased about 4-fold. Further increasing the size of the catalyst to 8.3±0.3 nm (QD2) slight increase in the rate of the reaction from 0.124 ms^{-1} to 0.163 ms^{-1} was observed which is surprising if we consider the surface area alone. Lower the surface area, higher should be catalytic efficicency. Interestingly, the highest efficiency was recorded for QD3 (Size: 9.4±0.4 nm). Further increasing the size to 15.7±0.7 nm did not increase the rate. The highest activity of QD3 is attributed to its photostability.[6,13]
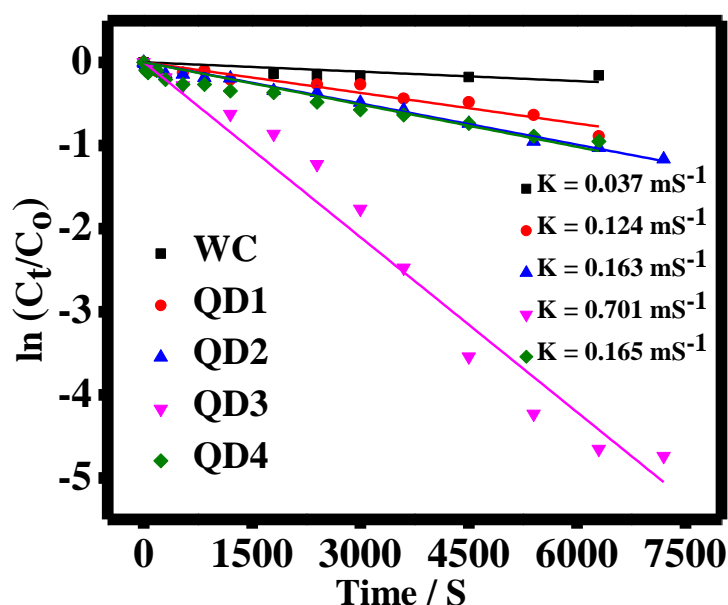
Figure 5.1: Comparative photocatalytic efficiency of QD1, QD2, QD3, QD4, and without catalyst (WC).

The photocatalytic study was performed in the presence of air at room temperature by dissolving **1a** in 3 mL of dichloromethane (DCM) 0.1 mg of QD catalyst was used for the study. The reaction mixture was illuminated with a blue LED having a maximum absorption wavelength of 461 nm with an illumination intensity of 0.363 mW/cm^2 at a distance of 10 cm apart. The formation of the product was monitored using the TLC technique and was isolated using column chromatography (10% EtOAc/Hexane) with a yield of 85%. The complete aromatization of the substrate was confirmed by performing the ^{1}H/^{13}C nuclear magnetic resonance (NMR) spectroscopy of the pure isolated product. Next, to optimized the reaction condition we performed an aromatization reaction in different solvents such as toluene, chloroform, tetrahydrofuran (THF), ethyl acetate, 1,4-dioxane, and 1,2-dichloroethane (DCE) having different polarity. The photocatalytic efficiency of QD3 was found to be excellent when 1,2-dichloroethane (DCE) was used as a solvent with an isolated yield of 95% (Table 5.1).

Table 5.1: Oxidative aromatization of 1a in different solvent using QD3 as catalyst.
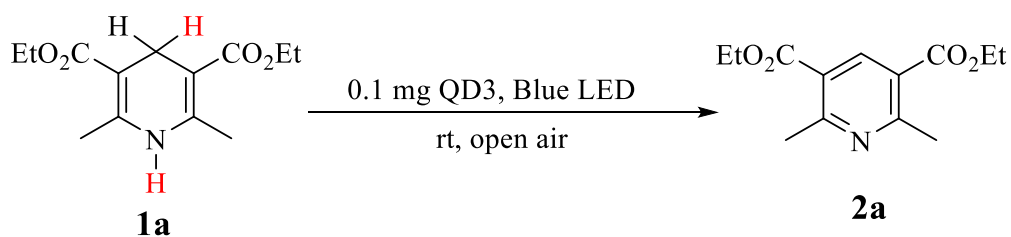
Entry	Catalysis	Solvent	Time (min)	Yield %
1	QD3	DCM	120	85
2	QD3	DCE	50	95
3	QD3	CHCl$_3$	90	80
4	QD3	Toluene	150	82
5	QD3	Ethyl acetate	60	86
6	QD3	1,4-dioxan	120	82
7	QD3	THF	90	84

Under the optimized reaction condition, catalyst (QD3) and solvent (DCE), the reaction was further extended to the oxidative aromatization of other substrates (*figure 5.2*) such as *aza*-heterocycle such as 1,3,5-triaryl-pyrazoline, (**1b**) 1,2-DHP (**1c**), and 2-aryl-2,3-dihydro benzothiazole (**1d**) to demonstrate the library of substrate scope. The method worked well for poor hydrogen transfer (HAT) too. In all the cases, yields above 85% were recorded.
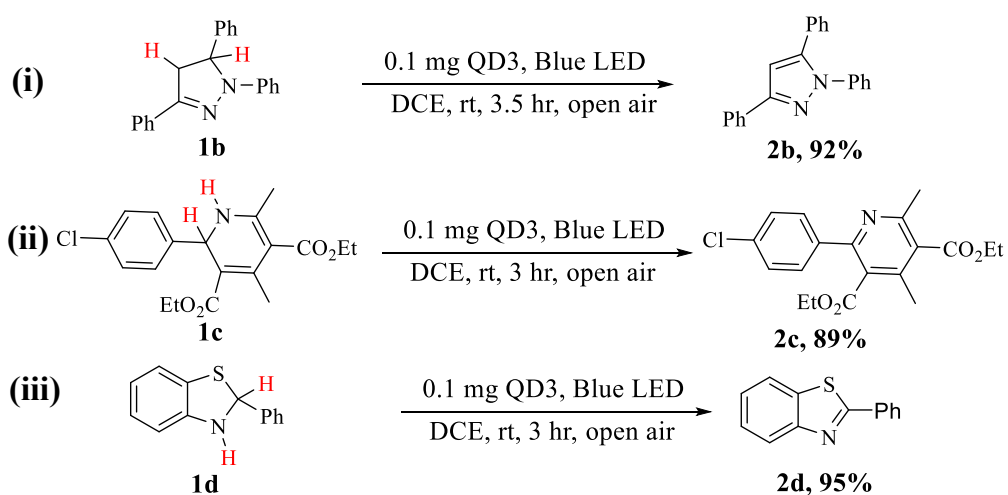
Figure 5.2: Oxidative aromatization reaction of different *aza*-heterocycle, 1,3,5 triphenyl- 4,5- dihydro-1H-prrazole(**1b**), 4-Cl-Phenyl-1,2-DHP(**1c**) and 2-phenyl-2,3 dihydrobenzo [d] thiozole(**1d**)

5.3. Mechanism

To understand the driving force of the reaction, the redox potential of the substrates (1a -1d) were measured using cyclic voltammetry (CV). CV studies were performed by dispersing the substrates in dry acetonitrile solvent using 0.1 M TBAP as a supporting electrolyte. The electrochemical investigation was performed under inert atmospheric condition using ferrocene/ferrocenium redox couple as an internal standard as shown in figure 5.3.
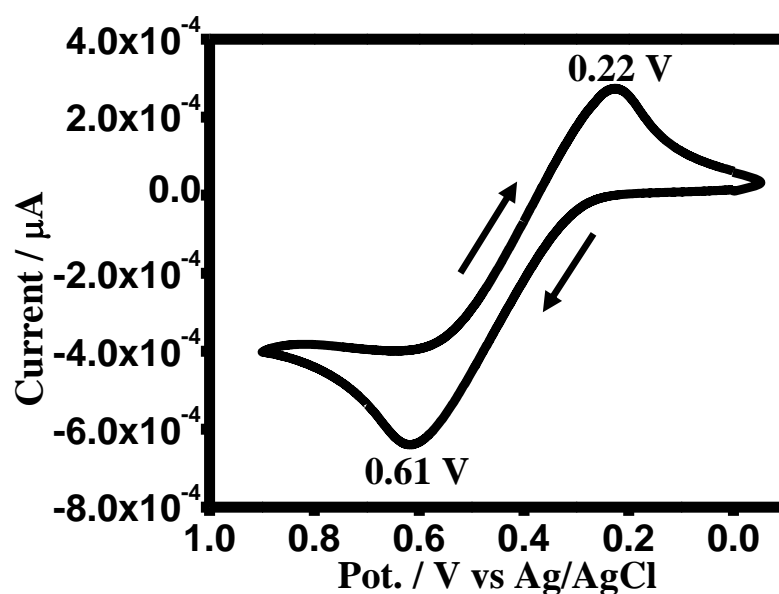
Figure 5.3: Cyclic voltammogram of ferrocene/ferrocenium (Fc/Fc$^+$) redox couple using TBAP (0.1 M) in acetonitrile, E_{redox} = 0.42 V *vs* Ag/AgCl.

The cyclic voltammogram of QD3 (*figure 5.4.*) shows the anodic peak (A$_1$) at 1.20 V and cathodic peak (C$_1$) at -1.26 V. Furthermore, the cyclic voltammogram of model substrate **1a** (*figure 5.4 b*) shows anodic peak at 0.92 V. It was observed that the redox potential value of model substrate (5.29 eV) lies above the VBM of QD3 inidicative of the substrate being a potential hole acceptor.
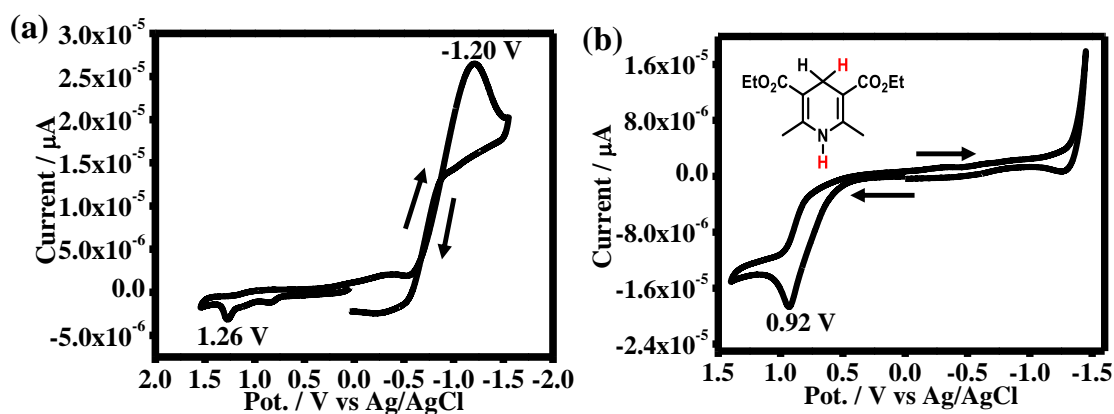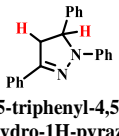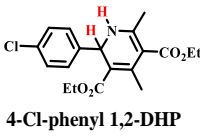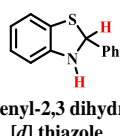
Figure 5.4: Cyclic voltammogram of (a) QD3 in 1:4 CH₃CN and toluene with a scan rate of 50 mVs⁻¹, and (b) model substrate **1a**, in CH₃CN with a scan rate of 50 mVs⁻¹.

The cyclic voltammogram of different azaheterocycle such as 1,2-DHP, 2-aryl-2,3-dihydro benzothiazole, and 1,3,5-triaryl-pyrazoline is shown in figure 5.5 and the redox potential value with respect to Ag/AgCl is shown in table 5.2.
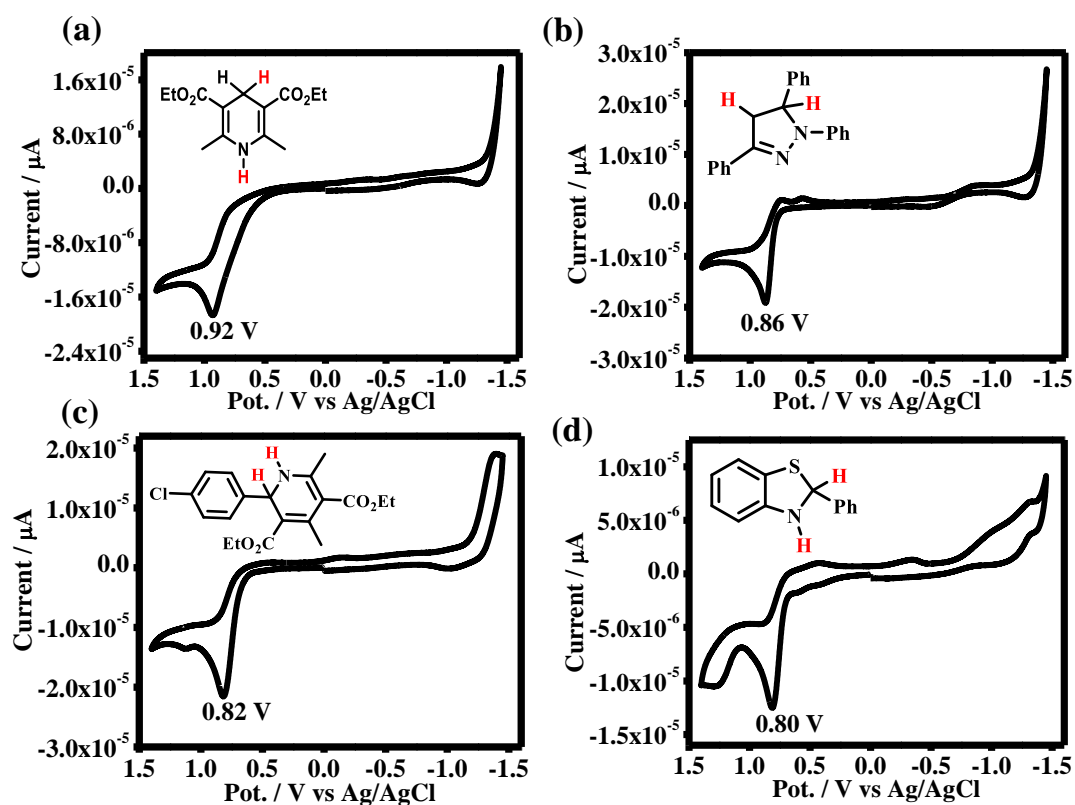
Figure 5.5: Cyclic voltammogram of different aza-heterocycle (a) 1,4-DHP, (b) 1,3,5 triphenyl-4,5-dihydro-1H-prrazole, (c) 4-Cl-Phenyl-1,2-DHP, and (d) 2-phenyl-2,3 dihydrobenzo [d] thiozole.

Table 5.2: Redox potential value of different aza-heterocycle relative to Ag/AgCl.

Aza-Heterocycle	1,4-DHP-H	1,3,5-triphenyl-4,5 -dihydro-1H-pyrazole	4-Cl-phenyl 1,2-DHP	2-phenyl-2,3 dihydrobenzo [d] thiazole
Redox Potential *vs Ag/AgCl* (V)	0.92 V	0.86 V	0.82 V	0.80 V
Redox Potential *vs Ag/AgCl* (eV)	-5.29 eV	-5.23 eV	-5.18 eV	-5.17 eV

The redox potential (V) value obtained from CV studies were converted to HOMO/LUMO energy levels (eV) with respect to Fc/Fc$^+$ redox couple as an internal standard (-4.8 eV to vacuum).[14] It was noted that the redox potential (eV) value of all the four class of aza-heterocycle lie well above the VBM of the QD3, thus acting as a potential hole acceptor as demonstrated in figure 5.6. Upon absorption of light, electron-hole pair is generated. Excited electron is transferred to dissolved oxygen while the whole transfer takes place to substrates, as both processes are thermodynamically downhill.
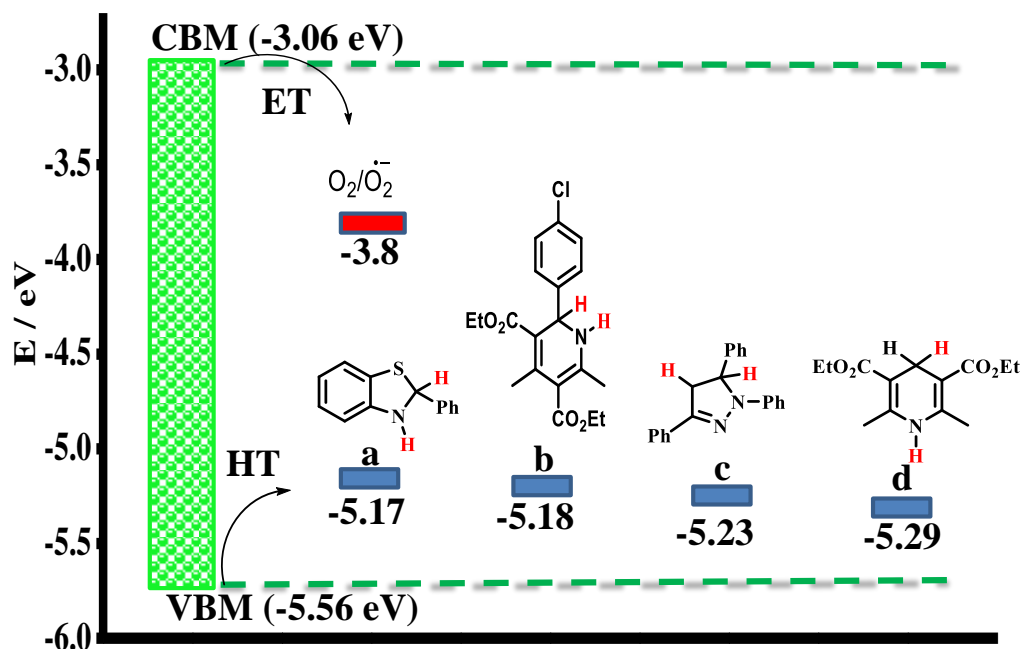
Figure 5.6: Redox potential of different aza-heterocycle compared with the VBM and CBM of QD1. The blue bar represents the VBM of a substrate which is well above the VBM of QD1 acting as a potential hole acceptor.

In order to confirm the hole accepting tendency of the substrates, we performed Stern-Volmer photoluminescence quenching experiments[15,16] (*figure 5.7.a*) and the quenching constant K_{sv} was calculated using the Stern-Volmer equation.[15]

$$I_o/I = 1 + K_{sv}[Q] \text{ .... (i)}$$

where I_0 and I are the highest photoluminescence intensity in the absence and presence of the quencher [Q]. The slope of [I_0/I - 1] vs [Q] plot gives the value of the Stern-Volmer quenching constant (K_{sv}). The photoluminescence quenching experiment of CsPbBr$_3$ QDs was carried out with 4-Me DHP as a quencher. The Stern-Volmer kinetics study was performed by taking the total volume of 3 mL reaction mixture (2.4 mL of toluene + 0.5 mL CsPbBr$_3$ QDs dispersed in 3 mL toluene + 0.1 mL of different concentration of quencher) using a standard fluorometer set-up with an excitation wavelength of 400 nm (*figure 5.7.a*). The linear correlation was obtained by plotting the slope of [I_0/I - 1] vs [Q] with K_{sv} of 8.59 as represented in figure 5.7.b.
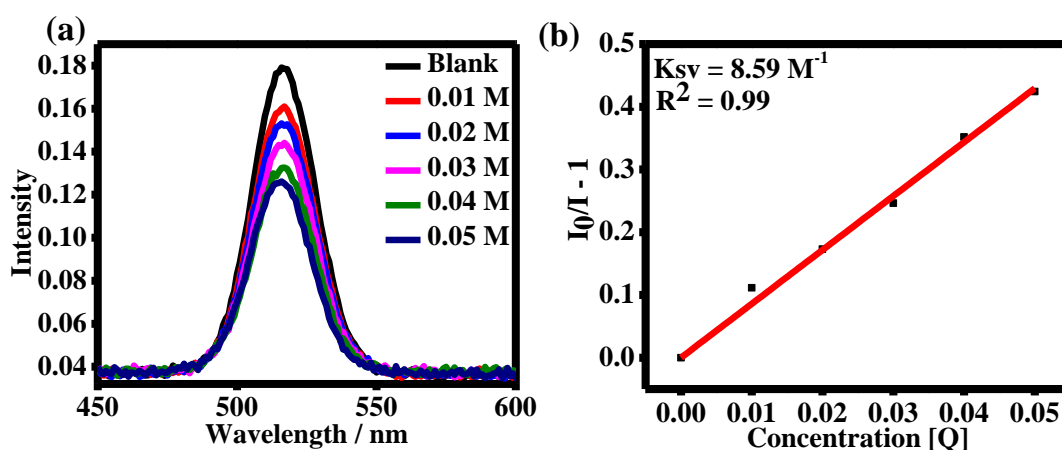
Figure 5.7: Representation of photoluminescence quenching experiment of QD3 in the presence of 4-Me-DHP (a), PL spectra of QD3 with the addition of different concentrations of 4-Me-DHP. (b) Stern-Volmer plot, k_{sv} = 8.59 M^{-1}.

5.4 Conclusion

The application of colloidal CsPbBr$_3$ QDs as photocatalyst in the oxidation aromatization of different class of azaheterocycles were studied. The rate of the reaction was dependent not only on the size (QD1 vs QD2) but more profoundly on the photostability of the QDs. QD3 with highest stability was the most efficient catalyst. The reactions were substantiated by corelating the redox potential of the organic substrate with the VBM of QD3, determined using CV. VBM of QD3 lie lower than

the redox potential of the substrates, thus allowing the hole transfer from excited QD to the substrate. The hole transfer was further confirmed by Stern-Volmer photoluminescence quenching experiment.

5.5. Spectral data of products

(a) Diethyl 2,6-dimethylpyridine-3,5-dicarboxylate (2a).

EtO$_2$C $\quad$ CO$_2$Et

2a
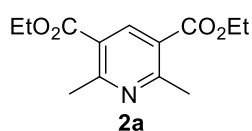
Following the general procedure, CsPbBr$_3$ perovskite **QD** (1 mg), **1a** (0.1 mmol) were dispersed in 3 mL DCE solvent in a 4 mL cylindrical glass vial and were subjected to blue light irradiation for 50 mins to complete the reaction and the pure aromatized product **2a** (23.8 mg, 0.095 mmol) was obtain in 95% yield. ^{1}H NMR (400 MHz, CDCl$_3$) δ 8.64 (s, 1H), 4.37 (q, J = 7.16 Hz, 4H), 2.81 (s, 6H), 1.38 (t, J = 7.16 Hz, 6H); ^{13}C{^{1}H} NMR (100 MHz, CDCl$_3$) δ 165.8, 162.1, 140.8, 123.0, 61.3, 24.8, 14.2

(b) 1,3,5-Triphenyl-1H-pyrazole (2b).

Ph

Ph $\quad$ N–Ph

Ph $\quad$ N

2b
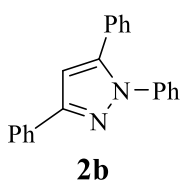
Following the general procedure, CsPbBr$_3$ perovskite **QD** (1 mg), **1b** (0.1 mmol) were dispersed in 3 mL DCE solvent in a 4 mL cylindrical glass vial and were subjected to blue light irradiation for 3.5 h to complete the reaction and the pure aromatized product, **2b** (27.2 mg, 0.092 mmol) was obtain in 92% yield. ^{1}H NMR (400 MHz, CDCl$_3$) δ 8.00 (d, J = 7.52 Hz, 2H), 7.51–7.35 (m, 13H), 6.89 (s, 1H); ^{13}C{^{1}H} NMR (100 MHz, CDCl$_3$) δ 152.0, 144.4, 140.1, 133.0, 130.6, 128.9, 128.8, 128.7, 128.5, 128.3, 128.0, 127.5, 125.8, 125.3, 105.2.

(c) Diethyl 2-(4-chlorophenyl)-4,6-dimethylpyridine-3,5-dicarboxylate (2c).
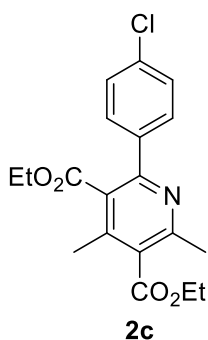
Following the general procedure, CsPbBr$_3$ perovskite **QD** (1 mg), **1c** (0.1 mmol) were dispersed in 3 mL DCE solvent in a 4 mL cylindrical glass vial and were subjected to blue light irradiation for 3 h to complete the reaction and the pure aromatized product, **2c** (32.2 mg, 0.089 mmol) was obtain in 89% yield. ^{1}H NMR (400 MHz, CDCl$_3$) δ 7.50 (d, J = 8.40 Hz, 2H), 7.38–7.35 (m, 2H), 4.42 (q, J = 7.08 Hz, 2H), 4.12 (q, J = 7.08 Hz, 2H), 2.58 (s, 3H), 2.33 (s, 3H), 1.38 (t, J = 7.04 Hz, 3H), 1.03 (t, J = 7.20 Hz, 3H); ^{13}C{^{1}H} NMR (100 MHz, CDCl$_3$) δ 168.34, 168.30, 155.5, 155.1, 143.1, 138.2, 135.2, 129.8, 128.8, 128.7, 127.3, 61.9, 61.8, 23.2, 17.0, 14.3, 13.8.

(d) 2-Phenylbenzo[*d*]thiazole (2d).
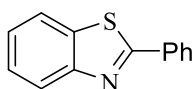
Following the general procedure, CsPbBr$_3$ perovskite **QD** (1 mg), **1d** (0.1 mmol) were dispersed in 3 mL DCE solvent in a 4 mL cylindrical glass vial and were subjected to blue light irradiation for 3 h to complete the reaction and the pure aromatized product, **2d** (20.0 mg, 0.095 mmol) was obtain in 95% yield. ^{1}H NMR (400 MHz, CDCl$_3$) δ 8.13–8.09 (m, 3H), 7.92 (d, J = 7.88 Hz, 1H), 7.52–7.50 (m, 4H), 7.42–7.39 (m, 1H); ^{13}C{^{1}H} NMR (100 MHz, CDCl$_3$) δ 168.1, 154.2, 135.0, 133.6, 131.0, 129.0, 127.5, 126.3, 125.2, 123.2, 121.6.

5.6. Copies of NMR spectra of the product

(1). Diethyl 2,6-dimethylpyridine-3,5-dicarboxylate (2a).
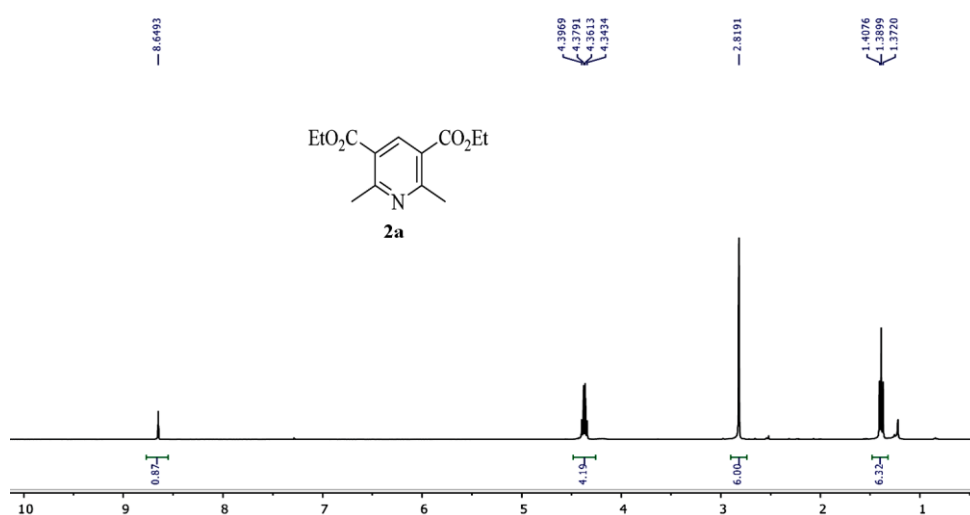
Figure 5.8: ^{1}H NMR of **2a** (400 MHz, CDCl$_3$).
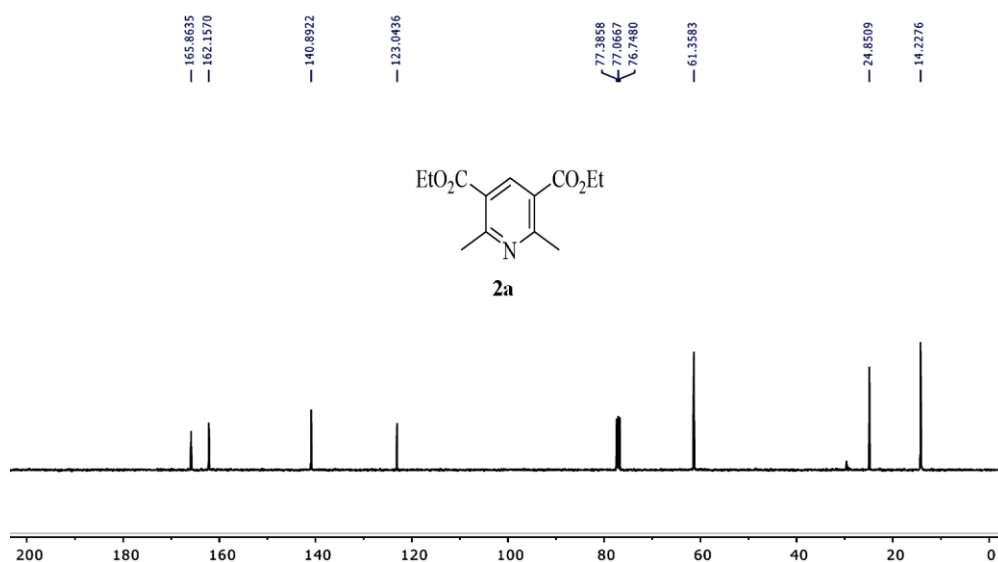
Figure 5.9: ^{13}C{^{1}H} NMR of **2a** (100 MHz, CDCl$_3$)

(2). 1,3,5-Triphenyl-1*H*-pyrazole (2b).
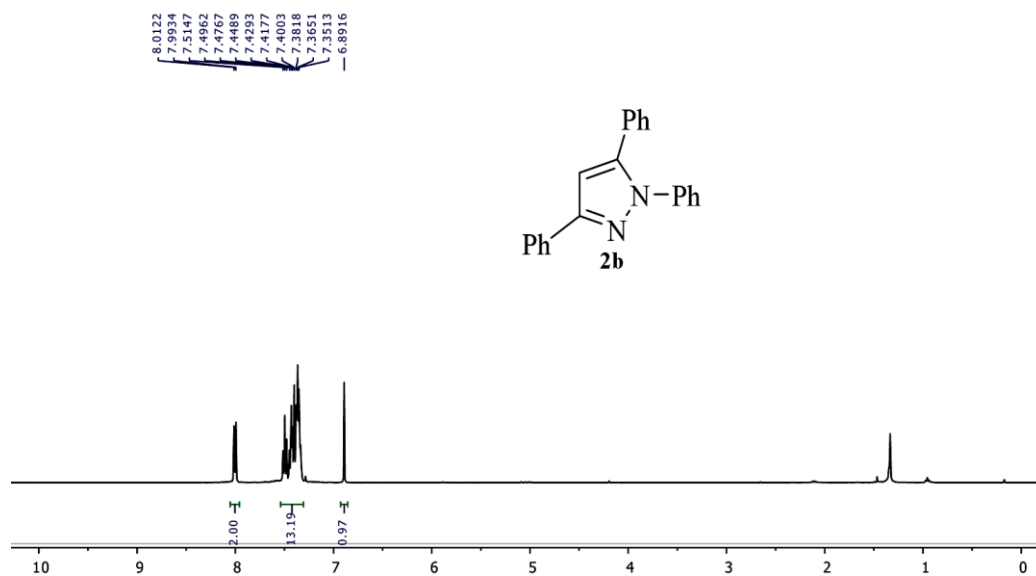
Figure 5.10: ^{1}H NMR of **2b** (400 MHz, CDCl$_3$).
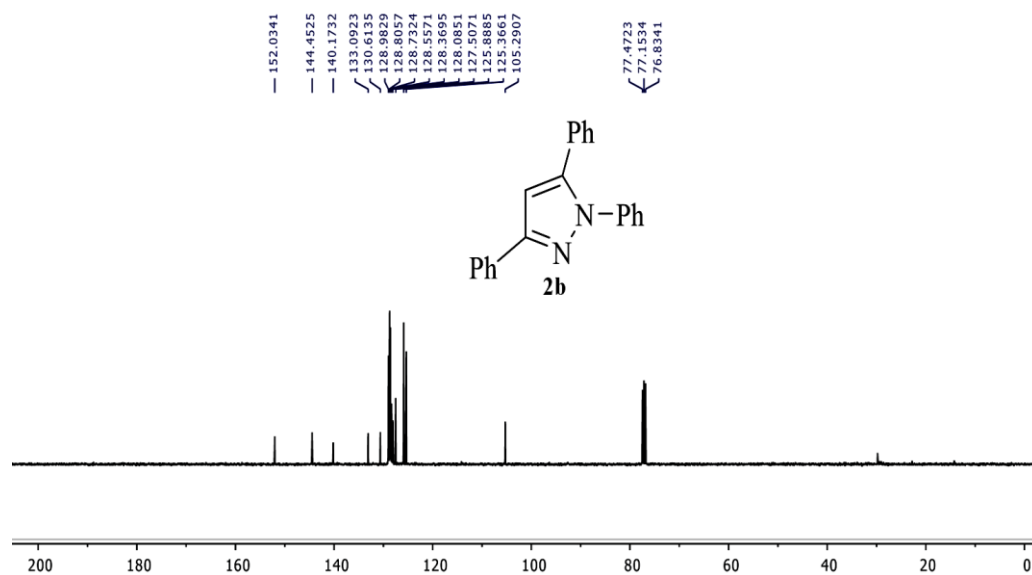
Figure 5.11: ^{13}C{^{1}H} NMR of **2b** (100 MHz, CDCl$_3$).

(3) Diethyl 2-(4-chlorophenyl)-4,6-dimethylpyridine-3,5-dicarboxylate (2c).
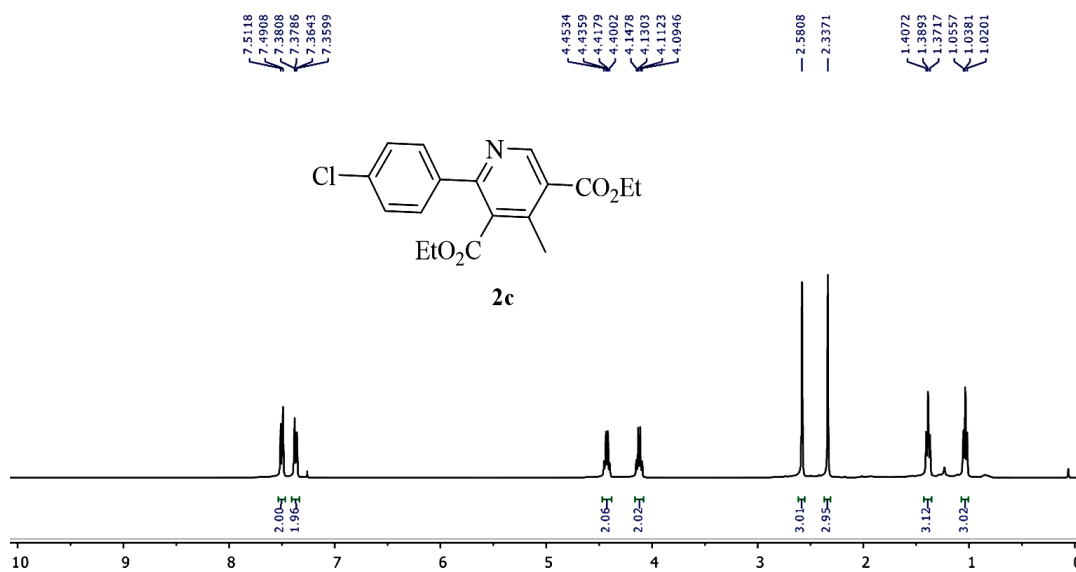
Figure 5.12: ^{1}H NMR of **2c** (400 MHz, CDCl$_3$).
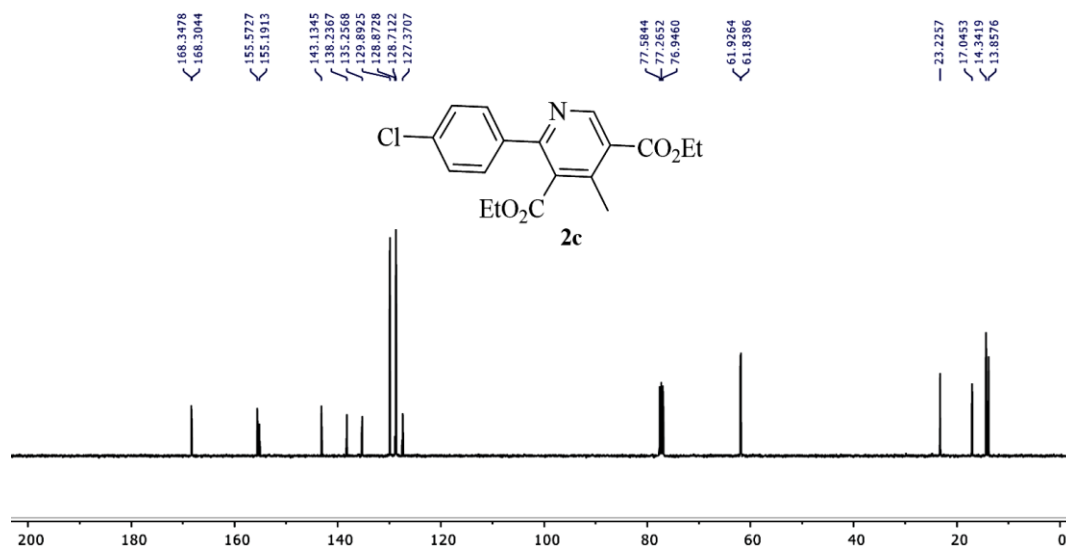
Figure 5.13: ^{13}C{^{1}H} NMR of **2c** (100 MHz, CDCl$_3$).

(4). 2-Phenylbenzo[*d*]thiazole (2d).
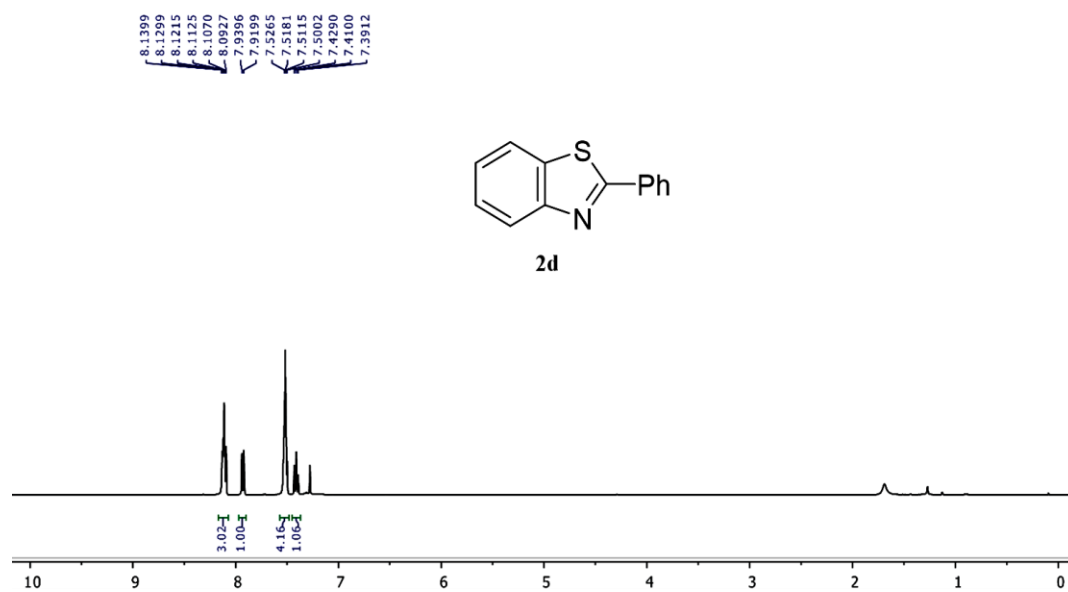
Figure 5.14: ^{1}H NMR of **2d** (400 MHz, CDCl$_3$).
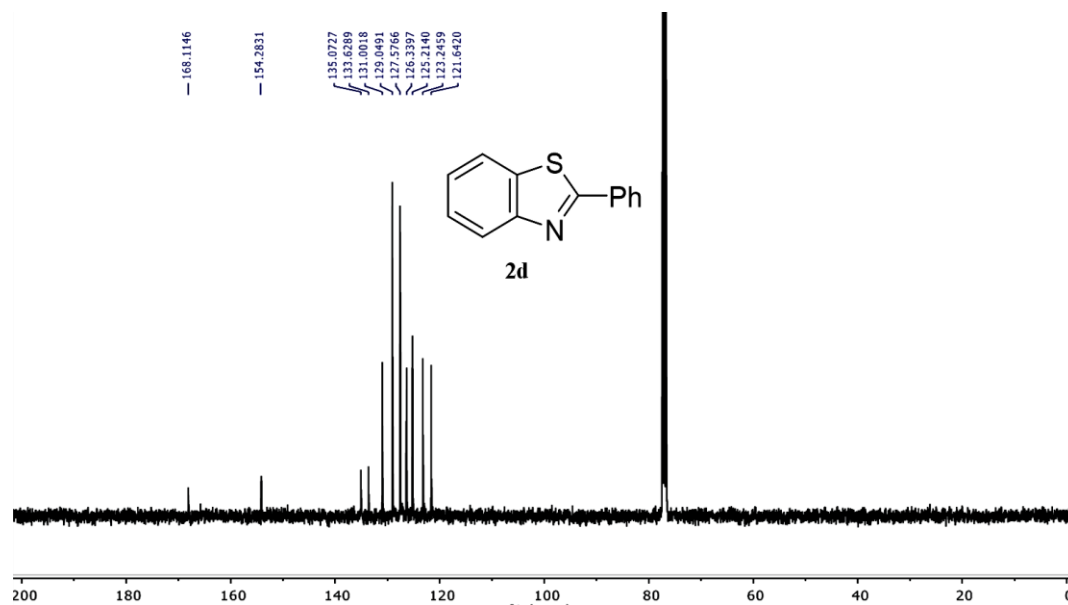
Figure 5.15: ^{13}C{^{1}H} NMR of **2d** (100 MHz, CDCl$_3$).

References

(1) Wang, Y.; Li, X.; Song, J.; Xiao, L.; Zeng, H.; Sun, H. All-Inorganic Colloidal Perovskite Quantum Dots: A New Class of Lasing Materials with Favorable Characteristics. *Adv. Mater.* **2015**, *27*, 7101–7108.

(2) Zhang, X.; Lin, H.; Huang, H.; Reckmeier, C.; Zhang, Y.; Choy, W. C. H.; Rogach, A. L. Enhancing the Brightness of Cesium Lead Halide Perovskite Nanocrystal Based Green Light-Emitting Devices through the Interface Engineering with Perfluorinated Ionomer. *Nano Lett.* **2016**, *16*, 1415–1420.

(3) Akkerman, Q. A.; Rainò, G.; Kovalenko, M. V.; Manna, L. Genesis, Challenges and Opportunities for Colloidal Lead Halide Perovskite Nanocrystals. *Nat. Mater.* **2018**, *17*, 394–405.

(4) Huang, H.; Bodnarchuk, M. I.; Kershaw, S. V.; Kovalenko, M. V.; Rogach, A. L. Lead Halide Perovskite Nanocrystals in the Research Spotlight: Stability and Defect Tolerance. *ACS Energy Lett.* **2017**, *2*, 2071–2083.

(5) Manser, J. S.; Christians, J. A.; Kamat, P. V. Intriguing Optoelectronic Properties of Metal Halide Perovskites. *Chem. Rev.* **2016**, *116*, 12956–13008.

(6) Zhu, X.; Lin, Y.; San Martin, J.; Sun, Y.; Zhu, D.; Yan, Y. Lead Halide Perovskites for Photocatalytic Organic Synthesis. *Nat. Commun.* **2019**, *10*, 1–10.

(7) Beatriz, A.; Vitoreti, F. Photocatalytic and Photoelectrochemical Degradation of Organic Compounds with All-Inorganic Metal Halide Perovskite Quantum Dots´. *J. Phys. Chem. Lett.* **2019**, *10*, 630–636.

(8) Guengerich, F. P.; Martin, M. V.; Beaune, P. H.; Kremers, P.; Wolff, T.; Waxman, D. J. Characterization of Rat and Human Liver Microsomal Cytochrome P-450 Forms Involved in Nifedipine Oxidation, a Prototype for Genetic Polymorphism in Oxidative Drug Metabolism. *J. Biol. Chem.* **1986**, *261*, 5051–5060.

(9) Stout, D. M.; Meyers, A. I. Recent Advances in the Chemistry of Dihydropyridines. *Chem. Rev.* **1982**, *82*, 223–243.

(10) Zhu, X. Q.; Zhao, B. J.; Cheng, J. P. Mechanisms of the Oxidations of NAD(P)H Model Hantzsch 1,4-Dihydropyridines by Nitric Oxide and Its Donor N-Methyl-

N-Nitrosotoluene-p-Sulfonamide. *J. Org. Chem.* **2000**, *65*, 8158–8163.

(11) O, D. V; Howlett, S. E.; E, E. Syntheses , Calcium Channel Agonist-Antagonist Modulation Activities , AndVoltage-Clamp Studies of Isopropyl 1,4-Dihydro-FL,G-Dimethy1-3-Nitro-4-Pyridinylpyridine-5-Carboxylate Racemates and Enantiomers. *J. Med. Chem.* **1995**, *38*, 2851–2859.

(12) Bocker, R. H.; Guengerich, F. P. Oxidation of 4-Aryl- and 4-Alkyl-Substituted 2,6-Dimethyl-3,5-Bis (Alkoxycarbonyl)-l,4-Dihydropyridines by Human Liver Microsomes and Immunochemical Evidence for the Involvement of a Form of Cytochrome P-450. *J. Med. Chem.* **1986**, *29*, 1596–1603.

(13) Pradhan, S.; Bhujel, D.; Gurung, B.; Sharma, D.; Basel, S.; Rasaily, S.; Thapa, S.; Borthakur, S.; Ling, W. L.; Saikia, L.; Reiss, P.; Pariyar, A.; Tamang, S. Stable Lead-Halide Perovskite Quantum Dots as Efficient Visible Light Photocatalysts for Organic Transformations. *Nanoscale Adv.* **2021**, *3*, 1464–1472.

(14) Leonat, L.; Sbarcea, G.; Branzoi, I. V. Cyclic Voltammetry For Energy Levels Estimation Of Organic Materials. *U.P.B. Sci. Bull* **2013**, *75*, 1454–2331.

(15) Wahba, M. E. K.; El-Enany, N.; Belal, F. Application of the Stern-Volmer Equation for Studying the Spectrofluorimetric Quenching Reaction of Eosin with Clindamycin Hydrochloride in Its Pure Form and Pharmaceutical Preparations. *Anal. Methods* **2015**, *7*, 10445–10451.

(16) Luiz, F. C. L.; Garcia, L. S.; Filho, L. S. G.; Teixeira, L. R.; Louro, S. R. W. Fluorescence Studies of Gold (III)-Norfloxacin Complexes in Aqueous Solutions. *J. Fluoresc.* **2011**, *21*, 1933–1940.

CHAPTER VI

CONCLUSION

CHAPTER VI

CONCLUSION

6.1. Summary and future perspective

The colloidal lead halide perovskite has gained much recognition in the past few years owing to its remarkable optoelectronic properties with power conversion efficiency more than 25%. These materials have shown to be an ideal candidate for solar cells, light-emitting diodes, photodetectors, and lasers. Essentially, their tunable opto-electronic properties are strongly dependent on the nature of electronic band structure such as band edge position (valence band and conduction band) and band gap energy. Therefore, to design and develop semiconductor NCs-based devices, the knowledge of band-gap engineering of their electronic structure is highly indispensable. Thus, electrochemical investigation of semiconductor NCs would be a powerful tool to understand the band edge position.

As of now, the clear understanding of the effect of size over the band edge alignment and optical transition across these edges without changing the composition of perovskites QDs have not been emphasized and the study of electrochemical investigation in this direction is highly noteworthy. We prepared $CsPbBr_3$ QDs at different injection temperature following the hot injection method. The reaction temperature plays a decisive role on optical properties and is attributed to the packing of capping ligands on the surface of QDs. The formed QDs were characterised using UV-visible absorption spectroscopy, PL spectroscopy, PXRD, TEM, XPS and FT-IR. It was observed that with the rise of reaction injection temperature from 160 to 220 ℃ the size of QDs increases from 7.2 to 15.7 nm whereas the optical band gap decreases from 2.56 to 2.44 eV (*Cf Chapter IV sec. 4.3*). The average particle sizes were 7.2 nm in 160 ℃, 8.3 nm in 170 ℃, 9.4 nm in 200 ℃, and 15.7 nm in 220 ℃, respectively. Furthermore, the electrochemical investigation of as-synthesized QDs were investigated by using cyclic voltammetry. It was noted that with the increase in the size of QDs the band gap decreases from 2.8 to 2.3 eV. This systematic shift in the optical and electrochemical band gap with respect to size is attribute to the size quantum confinement effect and has been observed previously. Thus, by varying the reaction

injection temperature we were able to tune the size and band gap (optical and electrochemical) of QDs.

Furthermore, we synthesized CsPbBr$_3$ QDs with various alkylamine (such as OAm-C18, SAm-C18, and DAm-C12) and carboxylic acid (such as OA-C18, SA-C18, and MA-C16) in order to understand the influence of capping ligands over optical and electrochemical properties. It was observed that by increasing the chain length of carboxylic acid and alkylamine the optical and electrochemical band gap increases. With carboxylic acid the optical band gap increases from 2.43 to 2.51 eV and electrochemical band gap increases from 2.53 to 2.68 eV, whereas with alkylamine the optical band gap increases from 2.42 to 2.51 eV and electrochemical band gap increases from 2.59 to 2.68 eV.

Also, we exploited CsPbBr$_3$ QDs as a photocatalyst in promoting oxidative aromatization, using different class of *aza*-heterocycle. We studied the photocatalytic efficiency of as-synthesized different size of CsPbBr$_3$ QDs. In order to examine the photocatalytic efficiency, we performed kinetic study using 1,4-DHP and the study was carried out by monitoring the progress of reaction using UV-visible absorption spectroscopy. The QD3 (~9.4 nm) with highest stability was the most efficient catalyst as compared to other size of QDs. The photocatalytic efficiency of QD3 was examined using 1,4-DHP with different solvents in presence of air at room temperature and found to be excellent when 1,2-dichloroethane was used with an isolated yield of 95%. The photocatalytic reactions were carried out by correlating the redox potential of the organic substrate with the VBM of QD3, determined using CV. It was observed that the redox potential of the substrates lies well above the VBM of the QDs, thus allowing the hole transfer from excited QDs to the substrate. The hole transfer was further confirmed by performing Stern-Volmer photoluminescence quenching experiment.

Since CsPbBr$_3$ QDs are versatile material for both optical and electrical purposes, there is still a plenty of room for further improvement towards the enhancement of tunable properties, stability and wide range of applicability.

Bibliography

Chapter I

(1)   Parida, B.; Iniyan, S.; Goic, R. A Review of Solar Photovoltaic Technologies. *Renew. Sustain. Energy Rev.* **2011**, *15*, 1625–1636.

(2)   Asim, N.; Sopian, K.; Ahmadi, S.; Saeedfar, K.; Alghoul, M. A.; Saadatian, O.; Zaidi, S. H. A Review on the Role of Materials Science in Solar Cells. *Renew. Sustain. Energy Rev.* **2012**, *16*, 5834–5847.

(3)   Etgar, L. Semiconductor Nanocrystals as Light Harvesters in Solar Cells. *Materials* **2013**, *6*, 445–459.

(4)   Mora-Seró, I.; Bisquert, J. Breakthroughs in the Development of Semiconductor-Sensitized Solar Cells. *J. Phys. Chem. Lett.* **2010**, *1*, 3046–3052.

(5)   Chapin, D. M.; Fuller, C. S.; Pearson, G. L. A New Silicon P-n Junction Photocell for Converting Solar Radiation into Electrical Power. *J. Appl. Phys.* **1953**, *25*, 676–677.

(6)   Ramanujam, J.; Singh, U. P. Copper Indium Gallium Selenide Based Solar Cells - A Review. *Energy Environ. Sci.* **2017**, *10*, 1306–1319.

(7)   Hagfeldt, A.; Boschloo, G.; Sun, L.; Kloo, L.; Pettersson, H. Dye-Sensitized Solar Cells. *Chem. Rev.* **2010**, *110*, 6595–6663.

(8)   Zhou, D.; Zhou, T.; Tian, Y.; Zhu, X.; Tu, Y. Perovskite-Based Solar Cells: Materials, Methods, and Future Perspectives. *J. Nanomater.* **2018**, *8*,1–15.

(9)   Yan, J.; Saunders, B. R. Third-Generation Solar Cells: A Review and Comparison of Polymer: Fullerene, Hybrid Polymer and Perovskite Solar Cells. *RSC Adv.* **2014**, *4*, 43286–43314.

(10)   Conibeer, G. Third-Generation Solar Cells. *Sol. Cell Mater. Dev. Technol.* **2014**, *16*, 283–314.

(11)   Yao, H.; Cui, Y.; Qian, D.; Ponseca, C. S.; Honarfar, A.; Xu, Y.; Xin, J.; Chen,

Z.; Hong, L.; Gao, B.; Yu, R.; Zu, Y.; Ma, W.; Chabera, P.; Pullerits, T.; Yartsev, A.; Gao, F.; Hou, J. 14.7% Efficiency Organic Photovoltaic Cells Enabled by Active Materials with a Large Electrostatic Potential Difference. *J. Am. Chem. Soc.* **2019**, *141*, 7743–7750.

(12)   Heinrichová, P.; Pospíšil, J.; Stříteský, S.; Vala, M.; Weiter, M.; Toman, P.; Rais, D.; Pfleger, J.; Vondráček, M.; Šimek, D.; Fekete, L.; Horáková, P.; Dokládalová, L.; Kubáč, L.; Kratochvílová, I. Diketopyrrolopyrrole-Based Organic Solar Cells Functionality: The Role of Orbital Energy and Crystallinity. *J. Phys. Chem. C* **2019**, *123*, 11447–11463.

(13)   Kan, B.; Zhang, Q.; Li, M.; Wan, X.; Ni, W.; Long, G.; Wang, Y.; Yang, X.; Feng, H.; Chen, Y. Solution-Processed Organic Solar Cells Based on Dialkylthiol-Substituted Benzodithiophene Unit with Efficiency near 10%. *J. Am. Chem. Soc.* **2014**, *136*, 15529–15532.

(14)   Huang, C.; Liao, X.; Gao, K.; Zuo, L.; Lin, F.; Shi, X.; Li, C. Z.; Liu, H.; Li, X.; Liu, F.; Chen, Y.; Chen, H.; Jen, A. K. Y. Highly Efficient Organic Solar Cells Based on S, N-Heteroacene Non-Fullerene Acceptors. *Chem. Mater.* **2018**, *30*, 5429–5434.

(15)   Lee, T. D.; Ebong, A. U. A Review of Thin Film Solar Cell Technologies and Challenges. *Renew. Sustain. Energy Rev.* **2017**, *70*, 1286–1297.

(16)   Gong, J.; Sumathy, K.; Qiao, Q.; Zhou, Z. Review on Dye-Sensitized Solar Cells (DSSCs): Advanced Techniques and Research Trends. *Renew. Sustain. Energy Rev.* **2017**, *68*, 234–246.

(17)   Mathew, S.; Yella, A.; Gao, P.; Humphry-baker, R.; Curchod, B. F. E.; Ashari-astani, N.; Tavernelli, I.; Rothlisberger, U.; Nazeeruddin, K.; Gra, M. Dye-Sensitized Solar Cells with 13% Efficiency Achieved through the Molecular Engineering of Porphyrin Sensitizers. *Nat. Chem.* **2014**, *6*, 242–247.

(18)   Pan, Z.; Rao, H.; Mora-sero, I.; Bisquert, J.; Zhong, X. Quantum Dot-Sensitized Solar Cells. *Chem Soc Rev.* **2018**, *47*, 7659–7702.

(19)   Ramade, J.; Qu, J.; Chu, A.; Gréboval, C.; Livache, C.; Goubet, N.; Martinez, B.; Vincent, G.; Lhuillier, E. Potential of Colloidal Quantum Dot Based Solar

Cells for Near-Infrared Active Detection. *ACS Photonics* **2020**, *7*, 272–278.

(20)   Chebrolu, V. T.; Kim, H. J. Recent Progress in Quantum Dot Sensitized Solar Cells: An Inclusive Review of Photoanode, Sensitizer, Electrolyte, and the Counter Electrode. *J. Mater. Chem. C* **2019**, *7*, 4911–4933.

(21)   Koster, L. J. A.; Mihailetchi, V. D.; Blom, P. W. M.; Koster, L. J. A.; Mihailetchi, V. D.; Blom, P. W. M. Ultimate Efficiency of Polymer / Fullerene Bulk Heterojunction Solar Cells. *Appl. Phys. Lett.* **2006**, *88*, 093511–09353.

(22)   Park, N. G. Perovskite Solar Cells: An Emerging Photovoltaic Technology. *Mater. Today* **2015**, *18*, 65–72.

(23)   Im, J.; Lee, C.; Lee, J.; Park, S.; Park, N. 6.5% Efficient Perovskite Quantum-Dot-Sensitized Solar Cell. *Nanoscale* **2011**, *3*, 4088–4093.

(24)   Manser, J. S.; Christians, A.; Kamat, P. V. Intriguing Optoelectronic Properties of Metal Halide Perovskites. *Chem. Rev.* **2016**, *116*, 12956–13008.

(25)   Ravi, V. K.; Markad, G. B.; Nag, A. Band Edge Energies and Excitonic Transition Probabilities of Colloidal $CsPbX_3$ (X = Cl, Br, I) Perovskite Nanocrystals. *ACS Energy Lett.* **2016**, *1*, 665–671.

(26)   Hasan, M.; Venkatesan, S.; Lyashenko, D. A.; Slinker, J. D.; Zakhidov, A. A Solvent Toolkit for Electrochemical Characterization of Hybrid Perovskite Films . *Anal. Chem* **2017**, *89*, 9649–9653.

(27)   Song, J.; Li, J.; Li, X.; Xu, L.; Dong, Y.; Zeng, H. Quantum Dot Light-Emitting Diodes Based on Inorganic Perovskite Cesium Lead Halides ($CsPbX_3$). *Adv. Mater* **2015**, *27*, 7162–7167.

(28)   Green, M. A.; Ho-baillie, A.; Snaith, H. J. The Emergence of Perovskite Solar Cells. *Nat. Photonics* **2014**, *8*, 506–513.

(29)   Sum, T. C.; Mathews, N. Advancements in Perovskite Solar Cells: Photophysics behind the Photovoltaics. *Energy Environ. Sci.* **2014**, *7*, 2518–2534.

(30)   Snaith, H. J. Perovskites: The Emergence of a New Era for Low-Cost, High-Efficiency Solar Cells. *J. Phys. Chem. Lett.* **2013**, *4*, 3623–3630.

(31)   Chang, J.; Waclawik, E. R. Colloidal Semiconductor Nanocrystals : Controlled

Synthesis and Surface Chemistry in Organic Media. *RSC Adv.* **2014**, *4*, 23505–23527.

(32) Poznyak, S. K.; Osipovich, N. P.; Shavel, A.; Talapin, D. V; Gao, M.; Eychmu, A.; Gaponik, N. Size-Dependent Electrochemical Behavior of Thiol-Capped CdTe Nanocrystals in Aqueous Solution. *J. Phys. Chem. B* **2005**, *109*, 1094–1100.

(33) Hines, M. A.; Scholes, G. D. Colloidal PbS Nanocrystals with Size-Tunable Near-Infrared Emission : Observation of Post- Synthesis Self-Narrowing of the Particle Size Distribution. *Adv. Mater.* **2003**, *15*, 1844–1849.

(34) Liu, J.; Yang, W.; Li, Y.; Fan, L.; Li, Y. Electrochemical Studies of the Effects of the Size, Ligand and Composition on the Band Structures of CdSe, CdTe and Their Alloy Nanocrystals. *Phys. Chem. Chem. Phys.* **2014**, *16*, 4778–4788.

(35) Yong, K.; Sahoo, Y.; Swihart, M. T.; Prasad, P. N. Shape Control of CdS Nanocrystals in One-Pot Synthesis. *J. Phys. Chem. C* **2007**, *111*, 2447–2458.

(36) Jeon, N. J.; Noh, J. H.; Yang, W. S.; Kim, Y. C.; Ryu, S.; Seo, J.; Seok, S. Il. Compositional Engineering of Perovskite Materials for High-Performance Solar Cells. *Nature* **2015**, *517*, 476–480.

(37) Imran, M.; Caligiuri, V.; Wang, M.; Goldoni, L.; Prato, M.; Krahne, R.; De Trizio, L.; Manna, L. Benzoyl Halides as Alternative Precursors for the Colloidal Synthesis of Lead-Based Halide Perovskite Nanocrystals. *J. Am. Chem. Soc.* **2018**, *140*, 2656–2664.

(38) Zhou, Y.; Zhu, K. Perovskite Solar Cells Shine in the "Valley of the Sun." *ACS Energy Lett.* **2016**, *1*, 64–67.

(39) Swarnkar, A.; Marshall, A. R.; Sanehira, E. M.; Chernomordik, B. D.; Moore, D. T.; Christians, J. A.; Chakrabarti, T.; Luther, J. M. Quantum Dot – Induced Phase Stabilization of a -CsPbI 3 Perovskite for High-Efficiency Photovoltaics. *Science* **2016**, *354*, 92–95.

(40) Gao, G.; Xi, Q.; Zhou, H.; Zhao, Y.; Wu, C.; Wang, L.; Guo, P.; Xu, J. Novel Inorganic Perovskite Quantum Dots for Photocatalysis. *Nanoscale* **2017**, *9*, 12032–12038.

(41) Samu, G. F.; Scheidt, R. A.; Kamat, P. V. Electrochemistry and Spectroelectrochemistry of Lead Halide Perovskite Films: Materials Science Aspects and Boundary Conditions. *Chem. Mater. 2018,* **2018**, *30*, 561–569.

(42) Inamdar, S. N.; Ingole, P. P.; Haram, S. K. Determination of Band Structure Parameters and the Quasi-Particle Gap of CdSe Quantum Dots by Cyclic Voltammetry. *ChemPhysChem* **2008**, *9*, 2574–2579.

(43) Smith, A. M.; Nie, S. Semiconductor Nanocrystals : Structure , Properties , and Band Gap Engineering. *Acc. Chem. Res.* **2009**, *43*, 190–200.

(44) Van Hecke, M. Semiconductor Nanocrystal. *Science* **2007**, *317*, 49–50.

(45) Dong, Y.; Qiao, T.; Kim, D.; Parobek, D.; Rossi, D.; Son, D. H. Precise Control of Quantum Confinement in Cesium Lead Halide Perovskite Quantum Dots via Thermodynamic Equilibrium. *Nano Lett.* **2018**, *18*, 3716–3722.

(46) Yarema, M.; Yarema, O.; Lin, W. M. M.; Volk, S.; Yazdani, N.; Bozyigit, D.; Wood, V. Upscaling Colloidal Nanocrystal Hot-Injection Syntheses via Reactor Underpressure. *Chem. Mater.* **2017**, *29*, 796–803.

(47) Williams, J. V.; Kotov, N. A.; Savage, P. E. Materials and Interfaces a Rapid Hot-Injection Method for the Improved Hydrothermal Synthesis of CdSe Nanoparticles. *Ind. Eng. Chem. Res.* **2009**, *48*, 4316–4321.

(48) Liu, M.; Matuhina, A.; Zhang, H.; Vivo, P. Advances in the Stability of Halide Perovskite Nanocrystals. *Materials* **2019**, *12*, 1–37.

(49) Lee, D.; Kim, M. H.; Woo, H. Y.; Chae, J.; Lee, D.; Jeon, S.; Oh, S. J.; Paik, T. Heating-up Synthesis of Cesium Bismuth Bromide Perovskite Nanocrystals with Tailored Composition, Morphology, and Optical Properties. *RSC Adv.* **2020**, *10*, 7126–7133.

(50) Cui, J.; Wang, L.; Yu, X. A Simple and Generalized Heat-up Method for the Synthesis of Metal Sulfide Nanocrystals. *New J. Chem.* **2019**, *43*, 16007–16011.

(51) Van Embden, J.; Chesman, A. S. R.; Jasieniak, J. J. The Heat-up Synthesis of Colloidal Nanocrystals. *Chem. Mater.* **2015**, *27*, 2246–2285.

(52) Thanh, N. T. K.; Maclean, N.; Mahiddine, S. Mechanisms of Nucleation and

Growth of Nanoparticles in Solution. *Chem. Rev.* **2014**, *114*, 7610–7630.

(53) Thapa, S.; Bhardwaj, K.; Basel, S.; Pradhan, S.; Eling, C. J.; Adawi, A. M.; Bouillard, J. S. G.; Stasiuk, G. J.; Reiss, P.; Pariyar, A.; Tamang, S. Long-Term Ambient Air-Stable Cubic CsPbBr$_3$ Perovskite Quantum Dots Using Molecular Bromine. *Nanoscale Adv.* **2019**, *1*, 3388–3391.

(54) Murray, C. B.; Noms, D. J.; Bawendi, M. G. Synthesis and Characterization of Nearly Monodisperse CdE (E = S, Se, Te) Semiconductor Nanocrystallites. *J. Am. Chem. Soc.* **1993**, *115*, 8706–8715.

(55) Talapin, D. V; Rogach, A. L.; Kornowski, A.; Haase, M.; Weller, H. Highly Luminescent Monodisperse CdSe and CdSe / ZnS Nanocrystals Synthesized in a Hexadecylamine − Trioctylphosphine Oxide − Trioctylphospine Mixture. *Nano Lett.* **2001**, *1*, 207–211.

(56) Blackman, B.; Battaglia, D. M.; Mishima, T. D.; Johnson, M. B.; Peng, X. Control of the Morphology of Complex Semiconductor Nanocrystals with a Type II Heterojunction , Dots vs Peanuts , by Thermal Cycling. *Chem. Mater* **2007**, *19*, 3815–3821.

(57) Peng, Z. A.; Peng, X. Nearly Monodisperse and Shape-Controlled CdSe Nanocrystals via Alternative Routes : Nucleation and Growth. *J. Am. Chem. Soc.* **2002**, *124*, 3343–3353.

(58) Steigerwald, M. L.; Gibson, M.; Harris, D.; Kortan, R.; Muller, A. J.; Duncan, T. M.; Douglass, D. C.; Brus, L. E. Surface Derivatization and Isolation of Semiconductor Cluster Molecules. *J. Am. Chem. Soc.* **1988**, *110*, 3046–3050.

(59) Haram, S. K.; Quinn, B. M.; Bard, A. J. Electrochemistry of CdS Nanoparticles : A Correlation between Optical and Electrochemical Band Gaps. *J. Am. Chem. Soc.* **2001**, *123*, 8860–8861.

(60) Querner, C.; Reiss, P.; Sadki, S.; Zagorska, M.; Pron, A. Size and Ligand Effects on the Electrochemical and Spectroelectrochemical Responses of CdSe Nanocrystals. *Phys.Chem.Chem. Phys* **2005**, *7*, 3204 –3209.

(61) Brus, L. E. Electron – Electron and Electronhole Interactions in Small Semiconductor Crystallites : The Size Dependence of the Lowest Excited

Electronic State Electron-Electron and Electron-Hole Interactions in Small Semiconductor Crystallites. *J. Chem. Phys.* **1984**, *80*, 4403–4409.

(62) Tamang, S.; Lincheneau, C.; Hermans, Y.; Jeong, S.; Reiss, P. Chemistry of InP Nanocrystal Syntheses. *Chem. Mater.* **2016**, *28*, 2491−2506.

(63) Talapin, D. V; Rogach, A. L.; Shevchenko, E. V; Kornowski, A.; Haase, M.; Weller, H. Dynamic Distribution of Growth Rates within the Ensembles of Colloidal II-VI and III-V Semiconductor Nanocrystals as a Factor Governing Their Photoluminescence Efficiency. *J. Am. Chem. Soc.* **2002**, *124*, 5782–5790.

(64) Micic, O.; Curtis, C. J.; Jones, K. M.; Sprague, J. R.; Nozik, A. J. Synthesis and Characterization of InP Quantum Dots. *J. Phys. Chem* **1994**, *98*, 4966–4969.

(65) Battaglia, D.; Peng, X. Formation of High Quality InP and InAs Nanocrystals in a Noncoordinating Solvent. *Nano Lett.* **2002**, *9*, 1027–1030.

(66) Lin, W.; Fritz, K.; Guerin, G.; Bardajee, G. R.; Hinds, S.; Sukhovatkin, V.; Sargent, E. H.; Scholes, G. D.; Winnik, M. A. Highly Luminescent Lead Sulfide Nanocrystals in Organic Solvents and Water through Ligand Exchange with Poly (Acrylic Acid). *Langmuir* **2008**, *24*, 8215–8219.

(67) Lee, S.; Jun, Y.; Cho, S.; Cheon, J. Single-Crystalline Star-Shaped Nanocrystals and Their Evolution : Programming the Geometry of Nano-Building Blocks. *J. Am. Chem. Soc.* **2002**, *124*, 11244–11245.

(68) Cademartiri, L.; Bertolotti, J.; Sapienza, R.; Wiersma, D. S.; Freymann, G. Von; Ozin, G. A. Multigram Scale , Solventless , and Diffusion-Controlled Route to Highly Monodisperse PbS Nanocrystals. *J. Phys. Chem. B* **2006**, *110*, 671–673.

(69) Talapin, D. V; Murray, C. B. PbSe Nanocrystal Solids for N- and p-Channel Thin Film Field-Effect Transistors. *Science* **2005**, *310*, 86–88.

(70) Urban, J. J.; Talapin, D. V; Shevchenko, E. V; Murray, C. B. Self-Assembly of PbTe Quantum Dots into Nanocrystal Superlattices and Glassy Films. *J. Am. Chem. Soc.* **2006**, *128*, 3248–3255.

(71) Ha, S. T.; Su, R.; Xing, J.; Zhang, Q.; Xiong, Q. Metal Halide Perovskite Nanomaterials: Synthesis and Applications. *Chem. Sci.* **2017**, *8*, 2522–2536.

(72) Chen, D.; Chen, X. Luminescent Perovskite Quantum Dots: Synthesis, Microstructures, Optical Properties and Applications. *J. Mater. Chem. C* **2019**, *7*, 1413–1446.

(73) James, C. Featured Graphic. Lives on the Line: Mapping Life Expectancy along the London Tube Network. *Environ. Plan. A* **2012**, *44*, 1525–1528.

(74) Swarnkar, A.; Ravi, V. K.; Nag, A. Beyond Colloidal Cesium Lead Halide Perovskite Nanocrystals: Analogous Metal Halides and Doping. *ACS Energy Lett.* **2017**, *2*, 1089–1098.

(75) Zhang, C.; Wang, B.; Wan, Q.; Kong, L.; Zheng, W.; Li, Z.; Li, L. Critical Role of Metal Ions in Surface Engineering toward Brightly Luminescent and Stable Cesium Lead Bromide Perovskite Quantum Dots. *Nanoscale* **2019**, *11*, 2602–2607.

(76) Akkerman, Q. A.; Martínez-Sarti, L.; Goldoni, L.; Imran, M.; Baranov, D.; Bolink, H. J.; Palazon, F.; Manna, L. Molecular Iodine for a General Synthesis of Binary and Ternary Inorganic and Hybrid Organic-Inorganic Iodide Nanocrystals. *Chem. Mater.* **2018**, *30*, 6915–6921.

(77) Akkerman, Q. A.; Rainò, G.; Kovalenko, M. V.; Manna, L. Genesis, Challenges and Opportunities for Colloidal Lead Halide Perovskite Nanocrystals. *Nat. Mater.* **2018**, *17*, 394–405.

(78) Kojima, A.; Teshima, K.; Shirai, Y.; Miyasaka, T. Organometal Halide Perovskites as Visible-Light Sensitizers for Photovoltaic Cells. *J. Am. Chem. Soc.* **2009**, *131*, 6050–6051.

(79) Singh, S. P.; Nagarjuna, P. Organometal Halide Perovskites as Useful Materials in Sensitized Solar Cells. *Dalt. Trans.* **2014**, *43*, 5247–5251.

(80) Lee, M. M.; Teuscher, J.; Miyasaka, T.; Murakami, T. N.; Snaith, H. J. Efficient Hybrid Solar Cells Based on Meso-Superstructured Organometal Halide Perovskitesfile. *Science* **2012**, *338*, 643–646.

(81) Kim, H.; Lee, C.; Im, J.; Lee, K.; Moehl, T.; Marchioro, A.; Moon, S.; Humphry-baker, R.; Yum, J.; Moser, J. E.; Gra, M. Lead Iodide Perovskite Sensitized All-Solid-State Submicron Thin Film Mesoscopic Solar Cell with Efficiency

Exceeding 9%. *Sci. Rep.* **2012**, *591*, 1–7.

(82)   Chung, I.; Lee, B.; He, J.; Chang, R. P. H.; Kanatzidis, M. G. All-Solid-State Dye-Sensitized Solar Cells with High Efficiency. *Nature* **2012**, *485*, 486–489.

(83)   Gra, M. Sequential Deposition as a Route to High-Performance Perovskite-Sensitized Solar Cells. *Nature* **2013**, *499*, 316–319.

(84)   Zhou, H.; Chen, Q.; Li, G.; Luo, S.; Song, T.; Duan, H.-S.; Hong, Z.; You, J.; Liu, Y.; Yang, Y. Interface Engineering of Highly Efficient Perovskite Solar Cells Huanping. *Science* **2014**, *345*, 542–546.

(85)   Stoumpos, C. C.; Malliakas, C. D.; Kanatzidis, M. G. Semiconducting Tin and Lead Iodide Perovskites with Organic Cations: Phase Transitions, High Mobilities, and Near-Infrared Photoluminescent Properties. *Inorg. Chem.* **2013**, *15*, 9019–9038.

(86)   Kojima, A.; Teshima, K.; Shirai, Y.; Miyasaka, T. Organometal Halide Perovskites as Visible-Light Sensitizers for Photovoltaic. *J. Am. Chem. Soc.* **2009**, *131*, 6050–6051.

(87)   Luan, M.; Song, J.; Wei, X.; Chen, F.; Liu, J. Controllable Growth of Bulk Cubic-Phase $CH_3NH_3PbI_3$ Single Crystal with Exciting Room-Temperature Stability. *Cryst. Eng. Comm.* **2016**, *18*, 5257–5261.

(88)   Li, G.; Wisnivesky, F.; Rivarola, R.; Davis, N. J. L. K.; Bai, S.; Jellicoe, T. C.; Peña, F. De; Hou, S.; Ducati, C.; Gao, F.; Friend, R. H.; Greenham, N. C.; Tan, Z. Highly Efficient Perovskite Nanocrystal Light-Emitting Diodes Enabled by a Universal Crosslinking Method. *Adv. Mater.* **2016**, *28*, 3528–3534.

(89)   Li, X.; Wang, Y.; Sun, H.; Zeng, H. Amino-Mediated Anchoring Perovskite Quantum Dots for Stable and Low-Threshold Random Lasing. *Adv. Mater.* **2017**, *29*, 1701185-1701194.

(90)   Huang, C.; Zou, C.; Mao, C.; Corp, K. L.; Yao, Y.; Lee, Y.; Schlenker, C. W.; Jen, A. K. Y.; Lin, L. Y. $CsPbBr_3$ Perovskite Quantum Dot Vertical Cavity Lasers with Low Threshold and High Stability. *ACS Photonics* **2017**, *4*, 2281−2289.

(91)   Yakunin, S.; Sytnyk, M.; Kriegner, D.; Shrestha, S.; Richter, M.; Matt, G. J.;

Azimi, H.; Brabec, C. J.; Stangl, J.; Kovalenko, M. V; Heiss, W. Detection of X-Ray Photons by Solution-Processed Lead Halide Perovskites. *Nat. Photonics* **2015**, *9*, 444–449.

(92) Jasieniak, J.; Califano, M.; Watkins, S. E. Size-Dependent Valence and Conduction Band-Edge Energies of Semiconductor Nanocrystals. *ACS Nano* **2011**, *5*, 5888–5902.

(93) Sakai, N.; Ebina, Y.; Takada, K.; Sasaki, T. Electronic Band Structure of Titania Semiconductor Nanosheets Revealed by Electrochemical and Photoelectrochemical Studies. *J. Am. Chem. Soc.* **2004**, *126*, 5851–5858.

(94) Li, B. Y.; Zhong, H.; Li, R.; Zhou, Y.; Yang, C.; Li, Y. High-Yield Fabrication and Electrochemical Characterization of Tetrapodal CdSe , CdTe , and CdSe x Te 1 – x Nanocrystals. *Adv. Funct. Mater.* **2006**, *16*, 1705–1716.

(95) Jiang, F.; Li, Y.; Ye, M.; Fan, L.; Ding, Y.; Li, Y. Ligand-Tuned Shape Control , Oriented Assembly , and Electrochemical Characterization of Colloidal ZnTe Nanocrystals. *Chem. Mater.* **2010**, *22*, 4632–4641.

(96) Brandt, R. E.; Stevanovic, V.; Ginley, D. S. G.; Buonassisi, T. Identifying Defect-Tolerant Semiconductors with High Minority-Carrier Lifetimes : Beyond Hybrid Lead Halide Perovskites. *MRS Commun.* **2015**, *5*, 265–275.

(97) Garcia-gutierrez, D. F.; Hernandez-casillas, L. P.; Cappellari, M. V.; Fungo, F.; Mart, E.; Ixcoatl, D. Influence of the Capping Ligand on the Band Gap and Electronic Levels of PbS Nanoparticles through Surface Atomistic Arrangement Determination. *ACS Omega* **2018**, *3*, 393–405.

(98) Leonat, L.; Sbarcea, G.; Branzoi, I. V. Cyclic Voltammetry For Energy Levels Estimation Of Organic Materials. *U.P.B. Sci. Bull* **2013**, *75*, 1454–2331.

(99) Davis, R. J.; Lloyd, M. T.; Ferreira, S. R.; Bruzek, M. J.; Watkins, S. E.; Lindell, L.; Sehati, P.; Fahlman, M.; Anthony, J. E.; Hsu, J. W. P. Determination of Energy Level Alignment at Interfaces of Hybrid and Organic Solar Cells under Ambient Environment. *J. Mater. Chem.* **2011**, *21*, 1721–1729.

(100) Lupo, M. G.; Sala, F. D.; Carbone, L.; Zavelani-Rossi, M.; Fiore, A.; Lüer, L.; Polli, D.; Cingolani, R.; Manna, L.; Lanzani, G. Ultrafast Electron-Hole

Dynamics in Core/Shell CdSe/CdS Dot/Rod Nanocrystals. *Nano Lett.* **2008**, *8*, 4582–4587.

(101) Soreni-Harari, M.; Yaacobi-Gross, N.; Steiner, D.; Aharoni, A.; Banin, U.; Millo, O.; Tessler, N. Tuning Energetic Levels in Nanocrystal Quantum Dots through Surface Manipulations. *Nano Lett.* **2008**, *8*, 678–684.

(102) Schlaf, R.; Parkinson, B. A.; Lee, P. A.; Nebesny, K. W.; Armstrong, N. R. HOMO/LUMO Alignment at PTCDA/ZnPc and PTCDA/ClInPc Heterointerfaces Determined by Combined UPS and XPS Measurements. *J. Phys. Chem. B* **1999**, *103*, 2984–2992.

(103) Yu, D.; Wang, C.; Guyot-Sionnest, P. N-Type Conducting CdSe Nanocrystal Solids. *Science* **2003**, *300*, 1277–1280.

(104) Eckhardt, H.; Shacklette, L. W.; Jen, K. Y.; Elsenbaumer, R. L. The Electronic and Electrochemical Properties of Poly (Phenylene Vinylenes) and Poly (Thienylene Vinylenes): An Experimental and Theoretical Study. *J. Chem. Phys.* **1989**, *91*, 1303–1315.

(105) Gao, J.; Li, Y.; Yu, G.; Heeger, A. J. Polymer Light-Emitting Electrochemical Cells with Frozen Junctions. *J. Appl. Phys.* **1999**, *86*, 4594–4599.

(106) Sun, H.; Li, Z.; Kong, L.; Wang, B.; Zhang, C.; Yuan, Q.; Huang, S.; Liu, Y.; Li, L. Enhancing the Stability of $CsPbBr_3$ Nanocrystals by Sequential Surface Adsorption of S2- and Metal Ions. *Chem. Commun.* **2018**, *54*, 9345–9348.

(107) Kucur, E.; Riegler, J.; Urban, G. A.; Nann, T. Determination of Quantum Confinement in CdSe Nanocrystals by Cyclic Voltammetry. *J. Chem. Phys.* **2003**, *119*, 2333–2337.

(108) Kuçur, E.; Bücking, W.; Giernoth, R.; Nann, T. Determination of Defect States in Semiconductor Nanocrystals by Cyclic Voltammetry. *J. Phys. Chem. B* **2005**, *109*, 20355–20360.

(109) Kucur, E.; Riegler, J.; Urban, G. A.; Nann, T. Determination of Quantum Confinement in CdSe Nanocrystals by Cyclic Voltammetry. *J. Chem. Phys.* **2003**, *199*, 2333–2337.

(110) Shafiee, A.; Salleh, M. M.; Yahana, M. Determination of HOMO and LUMO of

[6, 6]-Phenyl C61-Butyric Acid through Voltametry Characterization. *Sains Malaysiana* **2011**, *40*, 173–176.

(111) Haram, S. K.; Kshirsagar, A.; Gujarathi, Y. D.; Ingole, P. P.; Nene, O. A.; Markad, G. B.; Nanavati, S. P. Quantum Confinement in CdTe Quantum Dots : Investigation through Cyclic Voltammetry Supported by Density Functional Theory (DFT). *J. Phys. Chem. C* **2011**, *115*, 6243–6249.

(112) Brédas, J. L.; Silbey, R.; Boudreaux, D. S.; Chance, R. R. Chain-Length Dependence of Electronic and Electrochemical Properties of Conjugated Systems: Polyacetylene, Polyphenylene, Polythiophene, and Polypyrrole. *J. Am. Chem. Soc.* **1983**, *105*, 6555–6559.

(113) Markad, G. B.; Battu, S.; Kapoor, S.; Haram, S. K. Interaction between Quantum Dots of CdTe and Reduced Graphene Oxide : Investigation through Cyclic Voltammetry and Spectroscopy. *J. Phys. Chem. C* **2013**, *117*, 20944–20950.

(114) Protesescu, L.; Yakunin, S.; Bodnarchuk, M. I.; Krieg, F.; Caputo, R.; Hendon, C. H.; Yang, R. X.; Walsh, A.; Kovalenko, M. V. Nanocrystals of Cesium Lead Halide Perovskites ($CsPbX_3$, X = Cl, Br, and I): Novel Optoelectronic Materials Showing Bright Emission with Wide Color Gamut. *Nano Lett.* **2015**, *15*, 3692–3696.

(115) Nedelcu, G.; Protesescu, L.; Yakunin, S.; Bodnarchuk, M. I.; Grotevent, M. J.; Kovalenko, M. V. Fast Anion-Exchange in Highly Luminescent Nanocrystals of Cesium Lead Halide Perovskites ($CsPbX_3$, X = Cl, Br, I). *Nano Lett.* **2015**, *15*, 5635–5640.

(116) Swarnkar, A.; Chulliyil, R.; Ravi, V. K.; Irfanullah, M.; Chowdhury, A.; Nag, A. Colloidal $CsPbBr_3$ Perovskite Nanocrystals: Luminescence beyond Traditional Quantum Dots. *Angew. Chemie - Int. Ed.* **2015**, *54*, 15424–15428.

(117) Samu, G. F.; Scheidt, R. A.; Kamat, P. V.; Janáky, C. Electrochemistry and Spectroelectrochemistry of Lead Halide Perovskite Films: Materials Science Aspects and Boundary Conditions. *Chem. Mater.* **2018**, *30*, 561–569.

Chapter II

(1)   Wang, Y.; Xia, Y. Bottom-Up and Top-Down Approaches to the Synthesis of Monodispersed Spherical Colloids of Low Melting-Point Metals. *Nano Lett.* **2004**, *4*, 2047–2050.

(2)   Pradhan, N. Journey of Making Cesium Lead Halide Perovskite Nanocrystals: What's Next. *J. Phys. Chem. Lett.* **2019**, *10*, 5847–5855.

(3)   Schlipf, J.; Askar, A. M.; Pantle, F.; Wiltshire, B. D.; Schneider, P.; Huber, L.; Shankar, K.; Müller-buschbaum, P. Top-Down Approaches Towards Single Crystal Perovskite Solar Cells. *Sci. Rep.* **2018**, *8*, 1–8.

(4)   Xie, L.; Lin, K.; Lu, J.; Feng, W.; Song, P.; Yan, C.; Liu, K.; Shen, L.; Tian, C.; Wei, Z. Efficient and Stable Low-Bandgap Perovskite Solar Cells Enabled by a $CsPbBr_3$ - Cluster Assisted Bottom-up Crystallization Approach. *J. Am. Chem. Soc.* **2019**, *141*, 20537–20546.

(5)   Sardar, S.; Jana, A.; Mukherjee, A.; Dhara, A.; Bandyopadhyay, A. Bottom-up Synthesis of Bright Fluorescent, Moisture-Resistant Methylammonium Lead Bromide Poly (3-Bromothiophene). *New J. Chem.* **2020**, *44*, 2053–2058.

(6)   Yoon, K. Liquid-Phase Bottom-up Synthesis of Graphene Nanoribbons. *Mater. Chem. Front* **2020**, *4*, 29–45.

(7)   Zhuang, Z.; Peng, Q.; Li, Y. Controlled Synthesis of Semiconductor Nanostructures in the Liquid Phase. *Chem. Soc. Rev.* **2011**, *40*, 5492–5513.

(8)   Chang, J.; Waclawik, E. R. Colloidal Semiconductor Nanocrystals : Controlled Synthesis and Surface Chemistry in Organic Media. *RSC Adv.* **2014**, *4*, 23505–23527.

(9)   Li, Z.; Hu, Q.; Tan, Z.; Yang, Y.; Leng, M.; Liu, X.; Ge, C.; Niu, G.; Tang, J. Aqueous Synthesis of Lead Halide Perovskite Nanocrystals with High Water Stability and Bright Photoluminescence. *ACS Appl. Mater. Interfaces* **2018**, *10*, 43915–43922.

(10)   Jing, L.; Kershaw, S. V; Li, Y.; Huang, X.; Li, Y.; Rogach, A. L.; Gao, M. Aqueous Based Semiconductor Nanocrystals. *Chem. Rev.* **2016**, *116*, 10623–10730.

(11)   Chiang, C. H.; Wu, C. G. A Method for the Preparation of Highly Oriented

MAPbI$_3$ Crystallites for High-Efficiency Perovskite Solar Cells to Achieve an 86% Fill Factor. *ACS Nano* **2018**, *12*, 10355–10364.

(12) Shamsi, J.; Urban, A. S.; Imran, M.; Trizio, L. De; Manna, L. Metal Halide Perovskite Nanocrystals : Synthesis, Post-Synthesis Modifications, and Their Optical Properties. *Chem. Rev.* **2019**, *119*, 3296–3348.

(13) Cao, M.; Djerdj, I.; Antonietti, M.; Niederberger, M.; August, R. V. Nonaqueous Synthesis of Colloidal ZnGa$_2$O$_4$ Nanocrystals and Their Photoluminescence Properties Fluorescent Semiconductor Nanocrystals Have Attracted Intensive Interest During the Past Decade Because of Their Promising Applications in Various Fields. *Chem. Mater.* **2016**, *19*, 5830–5832.

(14) Ye, Q.; Zhang, J.; Guo, P.; Fan, H.; Shchukin, D.; Wei, B.; Wang, H. Wet-Chemical Synthesis of Surface-Passivated Halide Perovskite Microwires for Improved Optoelectronic Performance and Stability. *ACS Appl. Mater. Interfaces* **2018**, *10*, 43850–43856.

(15) Chan, E. M.; Xu, C.; Mao, A. W.; Han, G.; Owen, J. S.; Cohen, B. E.; Milliron, D. J. Reproducible, High-Throughput Synthesis of Colloidal Nanocrystals for Optimization in Multidimensional Parameter Space. *Nano Lett.* **2010**, *10*, 1874–1885.

(16) Faraday, M. The Bakerian Lecture : Experimental Relations of Gold (and Other Metals) to Light. *Phil. Trans. R. Soc. Lond.* **1857**, *147*, 145–181.

(17) Murray, C. B.; Noms, D. J.; Bawendi, M. G. Synthesis and Characterization of Nearly Monodisperse CdE (E = S, Se, Te) Semiconductor Nanocrystallites. *J. Am. Chem. Soc.* **1993**, *115*, 8706–8715.

(18) Zacharaki, E.; Kalyva, M.; Fjellvåg, H.; Sjåstad, A. O. Burst Nucleation by Hot Injection for Size Controlled Synthesis of ε - Cobalt Nanoparticles. *Chem. Cent. J.* **2016**, *10*, 1–11.

(19) Murray, C. B.; Norris, D. J.; Bawendi, M. G. Synthesis and Characterization of Nearly Monodisperse CdE (E = S , Se , Te) Semiconductor Nanocrystallites. *J. Am. Chem. Soc.* **1993**, *115*, 8706–8715.

(20) Lamer, V. K.; Dinegar, H. Theory, Production and Mechanism of Formation of Monodispersed Hydrosols. *J. Am. Chem. Soc.* **1950**, *72*, 4847–4854.

(21) Protesescu, L.; Yakunin, S.; Bodnarchuk, M. I.; Krieg, F.; Caputo, R.; Hendon, C. H.; Yang, R. X.; Walsh, A.; Kovalenko, M. V. Nanocrystals of Cesium Lead Halide Perovskites (CsPbX$_3$, X = Cl, Br, and I): Novel Optoelectronic Materials

Showing Bright Emission with Wide Color Gamut. *Nano Lett.* **2015**, *15*, 3692–3696.

(22)   Ravi, V. K.; Markad, G. B.; Nag, A. Band Edge Energies and Excitonic Transition Probabilities of Colloidal $CsPbX_3$ (X = Cl, Br, I) Perovskite Nanocrystals. *ACS Energy Lett.* **2016**, *1*, 665–671.

(23)   Akkerman, Q. A.; Rainò, G.; Kovalenko, M. V.; Manna, L. Genesis, Challenges and Opportunities for Colloidal Lead Halide Perovskite Nanocrystals. *Nat. Mater.* **2018**, *17*, 394–405.

(24)   Shamsi, J.; Urban, A. S.; Imran, M.; De Trizio, L.; Manna, L. Metal Halide Perovskite Nanocrystals: Synthesis, Post-Synthesis Modifications, and Their Optical Properties. *Chem. Rev.* **2019**, *119*, 3296–3348.

(25)   Park, J.; An, K.; Hwang, Y.; Park, J.; Noh, H.; Kim, J.; Park, J.; Hwang, N.; Hyeon, T. Ultra-Large-Scale Syntheses of Monodisperse Nanocrystals. *Nat. Mater.* **2004**, *3*, 891–895.

(26)   Park, J.; Joo, J.; Kwon, S. G.; Jang, Y.; Hyeon, T. Synthesis of Monodisperse Spherical Nanocrystals Angewandte. *Angew. Chem. Int. Ed.* **2007**, *46*, 4630–4660.

(27)   Lee, D.; Kim, M. H.; Woo, H. Y.; Chae, J.; Lee, D.; Jeon, S.; Oh, S. J.; Paik, T. Heating-up Synthesis of Cesium Bismuth Bromide Perovskite Nanocrystals with Tailored Composition, Morphology, and Optical Properties. *RSC Adv.* **2020**, *10*, 7126–7133.

(28)   Tamang, S.; Lincheneau, C.; Hermans, Y.; Jeong, S.; Reiss, P. Chemistry of InP Nanocrystal Syntheses. *Chem. Mater.* **2016**, *28*, 2491−2506.

(29)   Van Embden, J.; Chesman, A. S. R.; Jasieniak, J. J. The Heat-up Synthesis of Colloidal Nanocrystals. *Chem. Mater.* **2015**, *27*, 2246–2285.

(30)   Zhao, Y. S.; Fu, H.; Peng, A.; Ma, Y.; Xiao, D.; Yao, J. Low-Dimensional Nanomaterials Based on Small Organic Molecules: Preparation and Optoelectronic Properties. *Adv. Mater.* **2008**, *20*, 2859–2876.

(31)   Kasai, H.; Nalwa, H. S.; Oikawa, H.; Okada, S.; Matsuda, H.; Minami, N.; Kakuta, A.; Ono, K.; Mukoh, A.; Nakanishi, H. A Novel Preparation Method of Organic Microcrystals. *Jpn. J. Appl. Phys.* **1992**, *31*, 1132–1134.

(32)   Wei, S.; Yang, Y.; Kang, X.; Wang, L.; Huang, L.; Pan, D. Room-temperature and gram-scale synthesis of $CsPbX_3$ (X = Cl, Br, I) perovskite nanocrystals with 50–85% photoluminescence quantum yields. *Chem. Commun.* **2016**, *52*, 7265–

7268.

(33)   Ng, C. K.; Yin, W.; Li, H.; Jasieniak, J. J. Scalable Synthesis of Colloidal CsPbBr$_3$ Perovskite Nanocrystals with High Reaction Yields through Solvent and Ligand Engineering. *Nanoscale* **2020**, *12*, 4859–4867.

(34)   Sun, S.; Yuan, D.; Xu, Y.; Wang, A.; Deng, Z. Ligand-Mediated Synthesis of Shape- Controlled Cesium Lead Halide Perovskite Nanocrystals via Reprecipitation Process at Room Temperature. *ACS Nano* **2016**, *10*, 3648–3657.

(35)   Shamsi, J.; Rastogi, P.; Caligiuri, V.; Abdelhady, A. L.; Spirito, D.; Manna, L.; Krahne, R. Bright-Emitting Perovskite Films by Large-Scale Synthesis and Photoinduced Solid-State Transformation of CsPbBr$_3$ Nanoplatelets. *ACS Nano* **2017**, *11*, 10206–10213.

(36)   Papavassiliou, G. C.; Pagona, G.; Karousis, N.; Mousdis, G. A.; Koutselas, I.; Vassilakopoulou, A. Nanocrystalline/Microcrystalline Materials Based on Lead-Halide Units. *J. Mater. Chem.* **2012**, *22*, 8271–8280.

(37)   Zhang, F.; Zhong, H.; Chen, C.; Wu, X. G.; Hu, X.; Huang, H.; Han, J.; Zou, B.; Dong, Y. Brightly Luminescent and Color-Tunable Colloidal CH$_3$NH$_3$PbX$_3$ (X = Br, I, Cl) Quantum Dots: Potential Alternatives for Display Technology. *ACS Nano* **2015**, *9*, 4533–4542.

(38)   Yang, B.; Chen, J.; Hong, F.; Mao, X.; Zheng, K.; Yang, S.; Li, Y.; Pullerits, T.; Deng, W.; Han, K. Lead-Free, Air-Stable All-Inorganic Cesium Bismuth Halide Perovskite Nanocrystals. *Angew. Chemie - Int. Ed.* **2017**, *56*, 12471–12475.

(39)   Povrozin, Y.; Barbieri, B. Fluorescence Spectroscopy; Handbook of Measurement in Science and Engineering, *John Wiley & Sons.* **2016**, *3*, 2475–2498.

(40)   Karoui, R.; Blecker, C. Fluorescence Spectroscopy Measurement for Quality Assessment of Food Systems-a Review. *Food Bioprocess Technol.* **2011**, *4*, 364–386.

(41)   Romani, A.; Clementi, C.; Miliani, C.; Favaro, G. Fluorescence Spectroscopy: A Powerful Technique for the Noninvasive Characterization of Artwork. *Acc. Chem. Res.* **2010**, *43*, 837–846.

(42)   F, H. C.; E, S. R. Tutorial on Powder X-Ray Diffraction for Characterizing Nanoscale Materials. *ACS Nano* **2019**, *13*, 7359–7365.

(43)   Lansing, E. Principles of Powder Diffraction. *R. Soc. Chem.* **2008**, *20*, 1–19.

(44)   Bunaciu, A. A.; S, E. G. U. X-Ray Diffraction : Instrumentation and

Applications. *Crit. Rev. Anal. Chem.* **2015**, *45*, 289–299.

(45) Thakral, N. K.; Zanon, R. L.; Kelly, R. C.; Thakral, S. Applications of Powder X-Ray Diffraction in Small Molecule Pharmaceuticals : Achievements and Aspirations. *J. Pharm. Sci.* **2018**, *107*, 2969–2982.

(46) Ismail, A. A.; Voort, F. R. Van De; Sedman, J. Fourier Transform Infrared Spectroscopy : Principles and Applications. *Tech. Instrum. Anal. Chem.* **1997**, *18*, 93–139.

(47) Furutani, Y.; Shimizu, H.; Asai, Y.; Fukuda, T.; Oiki, S.; Kandori, H. ATR-FTIR Spectroscopy Revealing the Different Vibrational Modes of the Selectivity Filter Interacting with K^+ and Na^+ in the Open and Collapsed Conformations of the KcsA Potassium Channel. *J. Phys. Chem. Lett.* **2012**, *3*, 3806–3810.

(48) Solteira, I.; Solteira, I.; Solteira, I. Infrared Spectroscopy : A Tool for Determination of the Degree of Conversion In. *J Appl Oral Sci.* **2008**, *16*, 145–149.

(49) Coates, J. Interpretation of Infrared Spectra , A Practical Approach. *Encycl. Anal. Chem.* **2006**, *31*, 179–193.

(50) Mantele, W.; Deniz, E. UV-VIS Absorption Spectroscopy: Lambert-Beer Reloaded. *Spectrochem. acta* **2016**, *173*, 965–968.

(51) Klotz, I. M. Ultraviolet Absorption Spectroscopy. *J. Chem. Educ.* **1945**, *22*, 328–336.

(52) Coats, A. W.; Redfern, J. P. Thermogravimetric Analysis. *Analyst* **1963**, *88*, 906–924.

(53) Sharp, J. H. Thermal Analysis. *Proc. Soc. Anal. Chem* **1971**, *8*, 112–115.

(54) Dollimore, D.; Lerdkanchanaporn, S. Thermal Analysis. *Anal. Chem.* **1998**, *70*, 27–36.

(55) Simon, J. Introduction to Thermal Analysis Techniques Applications. Brown, M. E., *Ed. Kluwer Academic Publishers*, **2001**.

(56) Mabboil, G. A. An Introduction to Cyclic Voltammetry. *J. Chem. Educ.* **1983**, *60*, 697–702.

(57) Elgrishi, N.; Rountree, K. J.; McCarthy, B. D.; Rountree, E. S.; Eisenhart, T. T.; Dempsey, J. L. A Practical Beginner's Guide to Cyclic Voltammetry. *J. Chem. Educ.* **2018**, *95*, 197–206.

(58) Sandford, C.; Edwards, M. A.; Klunder, K. J.; Hickey, D. P.; Li, M.; Barman, K.; Sigman, M. S.; White, H. S.; Minteer, S. D. A Synthetic Chemist's Guide to

Electroanalytical Tools for Studying Reaction Mechanisms. *Chem. Sci.* **2019**, *10*, 6404–6422.

(59) Killa, M.; Mercer, E. E.; Philp, R. H. Applications of Cyclic Voltammetry in the Characterization of Complexes at Low Ligand Concentrations. *Anal. Chem.* **1984**, *56*, 2401–2405.

(60) Querner, C.; Reiss, P.; Sadki, S.; Zagorska, M.; Pron, A. Size and Ligand Effects on the Electrochemical and Spectroelectrochemical Responses of CdSe Nanocrystals. *Phys.Chem.Chem. Phys* **2005**, *7*, 3204 –3209.

(61) Inamdar, S. N.; Ingole, P. P.; Haram, S. K. Determination of Band Structure Parameters and the Quasi-Particle Gap of CdSe Quantum Dots by Cyclic Voltammetry. *ChemPhysChem* **2008**, *9*, 2574–2579.

(62) Kucur, E.; Riegler, J.; Urban, G. A.; Nann, T. Determination of Quantum Confinement in CdSe Nanocrystals by Cyclic Voltammetry. *J. Chem. Phys.* **2003**, *199*, 2333–2337.

(63) Haram, S. K.; Quinn, B. M.; Bard, A. J. Electrochemistry of CdS Nanoparticles : A Correlation between Optical and Electrochemical Band Gaps. *J. Am. Chem. Soc.* **2001**, *123*, 8860–8861.

(64) Haram, S. K.; Kshirsagar, A.; Gujarathi, Y. D.; Ingole, P. P.; Nene, O. A.; Markad, G. B.; Nanavati, S. P. Quantum Confinement in CdTe Quantum Dots : Investigation through Cyclic Voltammetry Supported by Density Functional Theory (DFT). *J. Phys. Chem. C* **2011**, *115*, 6243–6249.

(65) Hart, N. T.; Lane, W. C.; Garza, L. De. Electrochemical Quanti Fi Cation of Acetaminophen: An Engaging Cyclic Voltammetry Laboratory for the Quantitative Analysis Course. *J. Chem. Educ.* **2020**, *97*, 2254–2259.

(66) Hayyan, M.; Hashim, M. A.; Alnashef, I. M. Superoxide Ion: Generation and Chemical Implications. *Chem. Rev.* **2016**, *116*, 3029–3085.

(67) Jalilov, A. S.; Zhang, C.; Samuel, E. L. G.; Sikkema, W. K. A.; Wu, G.; Berka, V.; Kent, T. A.; Tsai, A. L.; Tour, J. M. Mechanistic Study of the Conversion of Superoxide to Oxygen and Hydrogen Peroxide in Carbon Nanoparticles. *ACS Appl. Mater. Interfaces* **2016**, *8*, 15086–15092.

(68) Nakamura, E.; Editor, G.; Sommerdijk, N. A. J. M.; Editor, G. Transmission Electron Microscopy for Chemists. *Acc. Chem. Res.* **2017**, *50*, 1795–1796.

(69) Denny, M. S.; Parent, L. R.; Patterson, J. P.; Meena, S. K.; Pham, H.; Abellan, P.; Ramasse, Q. M.; Paesani, F.; Gianneschi, N. C.; Cohen, S. M. Transmission

Electron Microscopy Reveals Deposition of Metal Oxide Coatings onto Metal − Organic Frameworks. *J. Am. Chem. Soc.* **2018**, *140*, 1348–1357.

(70) Ma, H.; Shieh, K.-J.; Qiao, T. X. Study of Transmission Electron Microscopy (TEM) and Scanning Electron Microscopy (SEM). *Nat. Sci.* **2006**, *4*, 14–22.

(71) Senthil Kumar, P.; Grace Pavithra, K.; Naushad, M. Characterization Techniques for Nanomaterials. *Nanomaterials for Solar Cell Applications* **2019**, *47*, 97-124.

(72) Kaech, A. An Introduction To Electron Microscopy Instrumentation, Imaging and Preparation. *Cent. Microsc. Image Anal.* **2013**, *25*,1–26.

(73) Oswald, S. X-Ray Photoelectron Spectroscopy in Analysis of Surfaces*, John Wiley & Sons* **2013**.

(74) Markus, A. X-Ray Photoelectron Spectroscopy (XPS) as Part of the Course 'Characterization of Catalysts and Surfaces'. *IM Publications and Surface Spectra Ltd.* **2003**.

(75) Briggs, D. X-Ray Photoelectron Spectroscopy (XPS), *Perkin-Elmer Corporation*. **2005**.

Chapter III

(1) Yakuphanoglu, F.; Cukurovali, A.; Yilmaz, I. Refractive Index and Optical Absorption Properties of the Complexes of a Cyclobutane Containing Thiazolyl Hydrazone Ligand. *Opt. Mater.* **2005**, *27*, 1363–1368.

(2) Zhang, M.; Zheng, Z.; Fu, Q.; Chen, Z.; He, J.; Zhang, S.; Chen, C.; Luo, W. Synthesis and Single Crystal Growth of Perovskite Semiconductor $CsPbBr_3$. *J. Cryst. Growth* **2018**, *484*, 37–42.

(3) Su, Y.; Chen, X.; Ji, W.; Zeng, Q.; Ren, Z.; Su, Z.; Liu, L. Highly Controllable and Efficient Synthesis of Mixed-Halide $CsPbX_3$ (X = Cl, Br, I) Perovskite QDs toward the Tunability of Entire Visible Light. *ACS Appl. Mater. Interfaces* **2017**, *9*, 33020–33028.

(4) Qaid, S. M. H.; Ghaithan, H. M.; Al-asbahi, B. A.; Alqasem, A.; Aldwayyan, A. S. Fabrication of Thin Films from Powdered Cesium Lead Bromide ($CsPbBr_3$) Perovskite Quantum Dots for Coherent Green Light Emission. *ACS Omega*

2020, *5*, 30111–30122.

(5)   Yang, R. X.; Tan, L. Z. Understanding Size Dependence of Phase Stability and Band Gap in CsPbI$_3$ Perovskite Nanocrystals. *J. Chem. Phys.* **2020**, *152*, 34702– 34707.

(6)   Thapa, S.; Bhardwaj, K.; Basel, S.; Pradhan, S.; Eling, C. J.; Adawi, A. M.; Bouillard, J. S. G.; Stasiuk, G. J.; Reiss, P.; Pariyar, A.; Tamang, S. Long-Term Ambient Air-Stable Cubic CsPbBr$_3$ Perovskite Quantum Dots Using Molecular Bromine. *Nanoscale Adv.* **2019**, *1*, 3388–3391.

(7)   Pan, J.; Quan, L. N.; Zhao, Y.; Peng, W.; Murali, B.; Sarmah, S. P.; Yuan, M.; Sinatra, L.; Alyami, N. M.; Liu, J.; Yassitepe, E.; Yang, Z.; Voznyy, O.; Comin, R.; Hedhili, M. N.; Mohammed, O. F.; Lu, Z. H.; Kim, D. H.; Sargent, E. H.; Bakr, O. M. Highly Efficient Perovskite-Quantum-Dot Light-Emitting Diodes by Surface Engineering. *Adv. Mater.* **2016**, *28*, 8718–8725.

(8)   Beal, R. E.; Slotcavage, D. J.; Leijtens, T.; Bowring, A. R.; Belisle, R. A.; Nguyen, W. H.; Burkhard, G. F.; Hoke, E. T.; McGehee, M. D. Cesium Lead Halide Perovskites with Improved Stability for Tandem Solar Cells. *J. Phys. Chem. Lett.* **2016**, *7*, 746–751.

(9)   Wang, W.; Wu, Y.; Wang, D.; Zhang, T. Effective Control of the Growth and Photoluminescence Properties of CsPbBr$_3$/Cs$_4$PbBr$_6$ Nanocomposites by Solvent Engineering. *ACS Omega* **2019**, *4*, 19641–19646.

(10)   Imran, M.; Caligiuri, V.; Wang, M.; Goldoni, L.; Prato, M.; Krahne, R.; Trizio, L. De; Manna, L. Benzoyl Halides as Alternative Precursors for the Colloidal Synthesis of Lead-Based Halide Perovskite Nanocrystals. *J. Am. Chem. Soc* **2018**, *140*, 2656–2664.

(11)   Dutta. A. Dutta.K.S, Adhikari. D.S, P. N. Chemie. *Angew. Chemie Int. Ed.* **2018**, *57*, 9083–9087.

(12)   Swarnkar, A.; Marshall, A. R.; Sanehira, E. M.; Chernomordik, B. D.; Moore, D. T.; Christians, J. A.; Chakrabarti, T.; Luther, J. M. Quantum Dot – Induced Phase Stabilization of a -CsPbI$_3$ Perovskite for High-Efficiency Photovoltaics. *Science* **2016**, *354*, 92–95.

(13)   Luo, X.; Lai, R.; Li, Y.; Han, Y.; Liang, G.; Liu, X.; Ding, T.; Wang, J.; Wu, K. Triplet Energy Transfer from CsPbBr 3 Nanocrystals Enabled By. *J. Am. Chem. Soc* **2019**, *141*, 4186–4190.

(14)   Lee, D. C.; Jeong, S. Highly Stable Cesium Lead Halide Perovskite Nanocrystals

through in Situ Lead Halide Inorganic Passivation. *Chem. Mater.* **2017**, *29*, 7088–7092.

(15) Liu, J.; Song, K.; Shin, Y.; Liu, X.; Chen, J.; Yao, K. X.; Pan, J.; Yang, C.; Yin, J.; Xu, L.; Yang, H.; El-zohry, A. M.; Xin, B.; Mitra, S.; Hedhili, M. N.; Roqan, I. S.; Mohammed, O. F.; Han, Y.; Bakr, O. M. Light-Induced Self-Assembly of Cubic CsPbBr₃ Perovskite Nanocrystals into Nanowires. *Chem. Mater* **2019**, *31*, 6642–6649.

(16) Ravi, V. K.; Santra, P. K.; Joshi, N.; Chugh, J.; Singh, S. K.; Ghosh, P.; Nag, A. Origin of the Substitution Mechanism for the Binding of Organic Ligands on the Surface of CsPbBr 3 Perovskite Nanocubes. *J. Phys. Chem. Lett.* **2017**, *8*, 4988–4994.

(17) Worku, M.; Tian, Y.; Zhou, C.; Lin, H.; Chaaban, M.; Xu, L.; He, Q.; Beery, D.; Zhou, Y.; Lin, X.; Su, Y. feng; Xin, Y.; Ma, B. Hollow Metal Halide Perovskite Nanocrystals with Efficient Blue Emissions. *Sci. Adv.* **2019**, *6*, 1–9.

(18) Aldakov, D.; Reiss, P. Safer-by-Design Fluorescent Nanocrystals: Metal Halide Perovskites vs Semiconductor Quantum Dots. *J. Phys. Chem. C* **2019**, *123*, 12527–12541.

(19) Butkus, J.; Vashishtha, P.; Chen, K.; Gallaher, J. K.; Prasad, S. K. K.; Metin, D. Z.; Gaston, N.; Halpert, J. E.; Hodgkiss, J. M. The Evolution of Quantum Confinement in CsPbBr₃ Perovskite Nanocrystals. *Chem. Mater.* **2017**, *29*, 3644–3652.

(20) Yoo, D.; Woo, J. Y.; Kim, Y.; Kim, S. W.; Wei, S.; Jeong, S.; Kim, Y. Origin of the Stability and Transition from Anionic to Cationic Surface Ligand Passivation of All-Inorganic Cesium Lead Halide Perovskite Nanocrystals. *J. Phys. Chem. Lett* **2020**, *11*, 652–658.

(21) Pan, A.; He, B.; Fan, X.; Liu, Z.; Urban, J. J.; Alivisatos, A. P.; He, L.; Liu, Y. Insight into the Ligand-Mediated Synthesis of Colloidal CsPbBr₃ Perovskite Nanocrystals: The Role of Organic Acid, Base, and Cesium Precursors. *ACS Nano* **2016**, *10*, 7943–7954.

(22) Koh, T. M.; Shanmugam, V.; Guo, X.; Lim, S. S.; Filonik, O.; Herzig, E. M.; Müller-Buschbaum, P.; Swamy, V.; Chien, S. T.; Mhaisalkar, S. G.; Mathews, N. Enhancing Moisture Tolerance in Efficient Hybrid 3D/2D Perovskite Photovoltaics. *J. Mater. Chem. A* **2018**, *6*, 2122–2128.

(23) Ravi, V. K.; Markad, G. B.; Nag, A. Band Edge Energies and Excitonic

Transition Probabilities of Colloidal CsPbX$_3$ (X = Cl, Br, I) Perovskite Nanocrystals. *ACS Energy Lett.* **2016**, *1*, 665–671.

(24) Inamdar, S. N.; Ingole, P. P.; Haram, S. K. Determination of Band Structure Parameters and the Quasi-Particle Gap of CdSe Quantum Dots by Cyclic Voltammetry. *ChemPhysChem* **2008**, *9*, 2574–2579.

(25) Elgrishi, N.; Rountree, K. J.; McCarthy, B. D.; Rountree, E. S.; Eisenhart, T. T.; Dempsey, J. L. A Practical Beginner's Guide to Cyclic Voltammetry. *J. Chem. Educ.* **2018**, *95*, 197–206.

(26) Jalilov, A. S.; Zhang, C.; Samuel, E. L. G.; Sikkema, W. K. A.; Wu, G.; Berka, V.; Kent, T. A.; Tsai, A. L.; Tour, J. M. Mechanistic Study of the Conversion of Superoxide to Oxygen and Hydrogen Peroxide in Carbon Nanoparticles. *ACS Appl. Mater. Interfaces* **2016**, *8*, 15086–15092.

(27) Hayyan, M.; Hashim, M. A.; Alnashef, I. M. Superoxide Ion: Generation and Chemical Implications. *Chem. Rev.* **2016**, *116*, 3029–3085.

(28) Gagne, R. R.; Koval, C. A.; Lisensky, G. C. Ferrocene as an Internal Standard for Electrochemical Measurements. *Inorg. Chem.* **1980**, *19*, 2854–2855.

(29) Shafiee, A.; Salleh, M. M.; Yahana, M. Determination of HOMO and LUMO of [6, 6] -Phenyl C61-Butyric Acid through Voltametry Characterization. *Sains Malaysiana* **2011**, *40*, 173–176.

(30) Leonat, L.; Sbarcea, G.; Branzoi, I. V. Cyclic Voltammetry For Energy Levels Estimation Of Organic Materials. *U.P.B. Sci. Bull* **2013**, *75*, 1454–2331.

(31) Lewandowski, A.; Waligora, L.; Galinski, M. Ferrocene as a Reference Redox Couple for Aprotic Ionic Liquids. *Electroanalysis* **2009**, *21*, 2221–2227.

Chapter IV

(1) Akkerman, Q. A.; Martínez-Sarti, L.; Goldoni, L.; Imran, M.; Baranov, D.; Bolink, H. J.; Palazon, F.; Manna, L. Molecular Iodine for a General Synthesis of Binary and Ternary Inorganic and Hybrid Organic-Inorganic Iodide Nanocrystals. *Chem. Mater.* **2018**, *30*, 6915–6921.

(2)   Sun, H.; Li, Z.; Kong, L.; Wang, B.; Zhang, C.; Yuan, Q.; Huang, S.; Liu, Y.; Li, L. Enhancing the Stability of CsPbBr3 Nanocrystals by Sequential Surface Adsorption of S2- and Metal Ions. *Chem. Commun.* **2018**, *54*, 9345–9348.

(3)   Imran, M.; Caligiuri, V.; Wang, M.; Goldoni, L.; Prato, M.; Krahne, R.; De Trizio, L.; Manna, L. Benzoyl Halides as Alternative Precursors for the Colloidal Synthesis of Lead-Based Halide Perovskite Nanocrystals. *J. Am. Chem. Soc.* **2018**, *140*, 2656–2664.

(4)   Thapa, S.; Bhardwaj, K.; Basel, S.; Pradhan, S.; Eling, C. J.; Adawi, A. M.; Bouillard, J. S. G.; Stasiuk, G. J.; Reiss, P.; Pariyar, A.; Tamang, S. Long-Term Ambient Air-Stable Cubic CsPbBr3 Perovskite Quantum Dots Using Molecular Bromine. *Nanoscale Adv.* **2019**, *1*, 3388–3391.

(5)   Shamsi, J.; Urban, A. S.; Imran, M.; De Trizio, L.; Manna, L. Metal Halide Perovskite Nanocrystals: Synthesis, Post-Synthesis Modifications, and Their Optical Properties. *Chem. Rev.* **2019**, *119*, 3296–3348.

(6)   Guhrenz, C.; Benad, A.; Ziegler, C.; Haubold, D.; Gaponik, N.; Eychmüller, A. Solid-State Anion Exchange Reactions for Color Tuning of CsPbX3 Perovskite Nanocrystals. *Chem. Mater.* **2016**, *28*, 9033–9040.

(7)   Parobek, D.; Dong, Y.; Qiao, T.; Rossi, D.; Son, D. H. Photoinduced Anion Exchange in Cesium Lead Halide Perovskite Nanocrystals. *J. Am. Chem. Soc.* **2017**, *139*, 4358–4361.

(8)   Akkerman, Q. A.; Innocenzo, V. D.; Accornero, S.; Scarpellini, A.; Petrozza, A.; Prato, M.; Manna, L. Tuning the Optical Properties of Cesium Lead Halide Perovskite. *J. Am. Chem. Soc.* **2015**, *137*, 10276–10281.

(9)   Protesescu, L.; Yakunin, S.; Bodnarchuk, M. I.; Krieg, F.; Caputo, R.; Hendon, C. H.; Yang, R. X.; Walsh, A.; Kovalenko, M. V. Nanocrystals of Cesium Lead Halide Perovskites (CsPbX3, X = Cl, Br, and I): Novel Optoelectronic Materials Showing Bright Emission with Wide Color Gamut. *Nano Lett.* **2015**, *15*, 3692–3696.

(10)   Ravi, V. K.; Markad, G. B.; Nag, A. Band Edge Energies and Excitonic Transition Probabilities of Colloidal CsPbX3 (X = Cl , Br , I) Perovskite

Nanocrystals. *ACS Energy Lett.* **2016**, *1*, 665–671.

(11)   Butkus, J.; Vashishtha, P.; Chen, K.; Gallaher, J. K.; Prasad, S. K. K.; Metin, D. Z.; Gaston, N.; Halpert, J. E.; Hodgkiss, J. M. The Evolution of Quantum Confinement in CsPbBr3 Perovskite Nanocrystals. *Chem. Mater.* **2017**, *29*, 3644–3652.

(12)   Zorman, B. Quantum Confinement Effects in CdSe Quantum Dots ^ V2. *J. Phys. Chem* **1995**, *99*, 7649–7653.

(13)   Yang, R. X.; Tan, L. Z. Understanding Size Dependence of Phase Stability and Band Gap in CsPbI3 Perovskite Nanocrystals. *J. Chem. Phys.* **2020**, *152*, 34702–34707.

(14)   Querner, C.; Reiss, P.; Sadki, S.; Zagorska, M.; Pron, A. Size and Ligand Effects on the Electrochemical and Spectroelectrochemical Responses of CdSe Nanocrystals. *Phys.Chem.Chem. Phys* **2005**, *7*, 3204 –3209.

(15)   Haram, S. K.; Quinn, B. M.; Bard, A. J. Electrochemistry of CdS Nanoparticles : A Correlation between Optical and Electrochemical Band Gaps. *J. Am. Chem. Soc.* **2001**, *123*, 8860–8861.

(16)   Zhang, M.; Zheng, Z.; Fu, Q.; Chen, Z.; He, J.; Zhang, S.; Chen, C.; Luo, W. Synthesis and Single Crystal Growth of Perovskite Semiconductor CsPbBr3. *J. Cryst. Growth* **2018**, *484*, 37–42.

(17)   Chen, S.; Zhang, X.; Zhao, Y.; Zhang, Q. Effects of Reaction Temperature on Size and Optical Properties of CdSe Nanocrystals. *Bull. Mater. Sci.* **2010**, *33*, 547–552.

(18)   Inamdar, S. N.; Ingole, P. P.; Haram, S. K. Determination of Band Structure Parameters and the Quasi-Particle Gap of CdSe Quantum Dots by Cyclic Voltammetry. *ChemPhysChem* **2008**, *9*, 2574–2579.

(19)   Jasieniak, J.; Califano, M.; Watkins, S. E. Size-Dependent Valence and Conduction Band-Edge Energies of Semiconductor Nanocrystals. *ACS Nano* **2011**, *5*, 5888–5902.

(20)   Shao, Q.; Lin, H.; Shao, M. Determining Locations of Conduction Bands and Valence Bands of Semiconductor Nanoparticles Based on Their Band Gaps. *ACS*

Omega **2020**, *5*, 10297–10300.

(21)   Smith, A. M.; Nie, S. Semiconductor Nanocrystals: Structure, Properties, and Band Gap Engineering. *Acc. Chem. Res.* **2010**, *43*, 190–200.

(22)   Schulz, P.; Edri, E.; Kirmayer, S.; Hodes, G.; Cahen, D.; Kahn, A. Interface Energetics in Organo-Metal Halide Perovskite-Based Photovoltaic Cells. *Energy Environ. Sci.* **2014**, *7*, 1377–1381.

(23)   Ryu, S.; Noh, J. H.; Jeon, N. J.; Chan Kim, Y.; Yang, W. S.; Seo, J.; Seok, S. Il. Voltage Output of Efficient Perovskite Solar Cells with High Open-Circuit Voltage and Fill Factor. *Energy Environ. Sci.* **2014**, *7*, 2614–2618.

(24)   Brus, L. E. Electron-Electron and Electronhole Interactions in Small Semiconductor Crystallites : The Size Dependence of the Lowest Excited Electronic State Electron-Electron and Electron-Hole Interactions in Small Semiconductor Crystallites : The Size Dependence O. *J. Chem. Phys.* **1984**, *80*, 4403–4409.

(25)   Liu, J.; Yang, W.; Li, Y.; Fan, L.; Li, Y. Electrochemical Studies of the Effects of the Size, Ligand and Composition on the Band Structures of CdSe, CdTe and Their Alloy Nanocrystals. *Phys. Chem. Chem. Phys.* **2014**, *16*, 4778–4788.

(26)   Amelia, M.; Impellizzeri, S.; Monaco, S.; Yildiz, I.; Silvi, S.; Raymo, F. M.; Credi, A. Structural and Size Effects on the Spectroscopic and Redox Properties of Cdse Nanocrystals in Solution: The Role of Defect States. *ChemPhysChem* **2011**, *12*, 2280–2288.

(27)   Garcia-gutierrez, D. F.; Hernandez-casillas, L. P.; Cappellari, M. V.; Fungo, F.; Mart, E.; Ixcoatl, D. Influence of the Capping Ligand on the Band Gap and Electronic Levels of PbS Nanoparticles through Surface Atomistic Arrangement Determination. *ACS Omega* **2018**, *3*, 393–405.

Chapter V

(1) Wang, Y.; Li, X.; Song, J.; Xiao, L.; Zeng, H.; Sun, H. All-Inorganic Colloidal Perovskite Quantum Dots: A New Class of Lasing Materials with Favorable Characteristics. *Adv. Mater.* **2015**, *27*, 7101–7108.

(2) Zhang, X.; Lin, H.; Huang, H.; Reckmeier, C.; Zhang, Y.; Choy, W. C. H.; Rogach, A. L. Enhancing the Brightness of Cesium Lead Halide Perovskite Nanocrystal Based Green Light-Emitting Devices through the Interface Engineering with Perfluorinated Ionomer. *Nano Lett.* **2016**, *16*, 1415–1420.

(3) Akkerman, Q. A.; Rainò, G.; Kovalenko, M. V.; Manna, L. Genesis, Challenges and Opportunities for Colloidal Lead Halide Perovskite Nanocrystals. *Nat. Mater.* **2018**, *17*, 394–405.

(4) Huang, H.; Bodnarchuk, M. I.; Kershaw, S. V.; Kovalenko, M. V.; Rogach, A. L. Lead Halide Perovskite Nanocrystals in the Research Spotlight: Stability and Defect Tolerance. *ACS Energy Lett.* **2017**, *2*, 2071–2083.

(5) Manser, J. S.; Christians, J. A.; Kamat, P. V. Intriguing Optoelectronic Properties of Metal Halide Perovskites. *Chem. Rev.* **2016**, *116*, 12956–13008.

(6) Zhu, X.; Lin, Y.; San Martin, J.; Sun, Y.; Zhu, D.; Yan, Y. Lead Halide Perovskites for Photocatalytic Organic Synthesis. *Nat. Commun.* **2019**, *10*, 1–10.

(7) Beatriz, A.; Vitoreti, F. Photocatalytic and Photoelectrochemical Degradation of Organic Compounds with All-Inorganic Metal Halide Perovskite Quantum Dots´. *J. Phys. Chem. Lett.* **2019**, *10*, 630–636.

(8) Guengerich, F. P.; Martin, M. V.; Beaune, P. H.; Kremers, P.; Wolff, T.; Waxman, D. J. Characterization of Rat and Human Liver Microsomal Cytochrome P-450 Forms Involved in Nifedipine Oxidation, a Prototype for Genetic Polymorphism in Oxidative Drug Metabolism. *J. Biol. Chem.* **1986**, *261*, 5051–5060.

(9) Stout, D. M.; Meyers, A. I. Recent Advances in the Chemistry of Dihydropyridines. *Chem. Rev.* **1982**, *82*, 223–243.

(10) Zhu, X. Q.; Zhao, B. J.; Cheng, J. P. Mechanisms of the Oxidations of NAD(P)H Model Hantzsch 1,4-Dihydropyridines by Nitric Oxide and Its Donor N-Methyl-N-Nitrosotoluene-p-Sulfonamide. *J. Org. Chem.* **2000**, *65*, 8158–8163.

(11) O, D. V; Howlett, S. E.; E, E. Syntheses , Calcium Channel Agonist-Antagonist Modulation Activities, and Voltage-Clamp Studies of Isopropyl 1,4-Dihydro-FL,G-Dimethy1-3-Nitro-4-Pyridinylpyridine-5-Carboxylate Racemates and Enantiomers. *J. Med. Chem.* **1995**, *38*, 2851–2859.

(12) Bocker, R. H.; Guengerich, F. P. Oxidation of 4-Aryl- and 4-Alkyl-Substituted 2,6-Dimethyl-3,5-Bis (Alkoxycarbonyl)-l,4-Dihydropyridines by Human Liver Microsomes and Immunochemical Evidence for the Involvement of a Form of Cytochrome P-450. *J. Med. Chem.* **1986**, *29*, 1596–1603.

(13) Pradhan, S.; Bhujel, D.; Gurung, B.; Sharma, D.; Basel, S.; Rasaily, S.; Thapa, S.; Borthakur, S.; Ling, W. L.; Saikia, L.; Reiss, P.; Pariyar, A.; Tamang, S. Stable Lead-Halide Perovskite Quantum Dots as Efficient Visible Light Photocatalysts for Organic Transformations. *Nanoscale Adv.* **2021**, *3*, 1464–1472.

(14) Leonat, L.; Sbarcea, G.; Branzoi, I. V. Cyclic Voltammetry For Energy Levels Estimation Of Organic Materials. *U.P.B. Sci. Bull* **2013**, *75*, 1454–2331.

(15) Wahba, M. E. K.; El-Enany, N.; Belal, F. Application of the Stern-Volmer Equation for Studying the Spectrofluorimetric Quenching Reaction of Eosin with Clindamycin Hydrochloride in Its Pure Form and Pharmaceutical Preparations. *Anal. Methods* **2015**, *7*, 10445–10451.

(16) Luiz, F. C. L.; Garcia, L. S.; Filho, L. S. G.; Teixeira, L. R.; Louro, S. R. W. Fluorescence Studies of Gold(III)-Norfloxacin Complexes in Aqueous Solutions. *J. Fluoresc.* **2011**, *21*, 1933–1940.

APPENDIX-I

List of Publications

1. Stable Lead-Halide Perovskite Quantum Dots as Efficient Visible Light Photocatalysts for Organic Transformations. *Nanoscale Advances* **2021**, *3*, 1464-1472.

2. The Effect of Size and Capping-ligands on the Band-Edge Alignments of the CsPbBr$_3$ Perovskite Quantum Dots: A Cyclic voltammetry Study.

"Manuscript to be communicated"

3. Synthesis of CsPbBr$_3$ Perovskite Quantum Dots using DBI: Photocatalytic access to heterocycles via intramolecular sp^3 C–H Functionalization.

"Manuscript to be communicated"